Post Pulse Compression & Partially Adaptive Multi-Waveform Space-Time Adaptive Processing for Heterogeneous Clutter

By

Lumumba Harnett

Submitted to the graduate degree program in Department of Electrical Engineering and Computer Science and the Graduate Faculty of the University of Kansas in partial fulfillment of the requirements for the degree of Master of Science.

Dr. Shannon Blunt, Chairperson

Committee members

Dr. Christopher Allen, Committe Memeber

Dr. James Stiles, Commitee Member

Date defended: July 31, 2018

The Thesis Committee for Lumumba Harnett certifies
that this is the approved version of the following thesis :

Post Pulse Compression & Partially Adaptive Multi-Waveform Space-Time Adaptive Processing
for Heterogeneous Clutter

Dr. Shannon Blunt, Chairperson

Date approved: July 31, 2018

Abstract

A new form of multi-waveform space-time adaptive processing (μ-STAP) is presented. The formulation provides additional training data for adaptive clutter cancellation for ground moving target indication after pulse compression. The pulse compression response is homogenized using stochastic phase filters to produce a smeared response that approximates identically distribution assumed by covariance estimation. Post pulse compression μ-STAP (Pμ-STAP) is proposed to address clutter heterogeneity that causes degradation in detection performance of STAP similar to single-input multi-output μ-STAP. Furthermore, the family of μ-STAP algorithms are computationally expensive due to estimation of multiple covariance matrices and inversion of a single covariance for every range sample. Well-known partially adaptive techniques, previously implemented in STAP, are implemented with Pμ-STAP. Partial adaptation in element-space post-Doppler, beam-space pre-Doppler, and beam-space post-Doppler are presented. Each of these are examined on several simulated, controlled clutter scenarios. Fully adaptive Pμ-STAP is further evaluated on the high-fidelity knowledge aided adaptive radar architecture: knowledge-aided sensor signal processing and expert reasoning (KASSPER) dataset.

Acknowledgements

I would like to dedicate this to the warm community of Lawrence, Kansas, the faculty and staff at the amazing Department of Electrical Engineering and Computer Science, my chairperson for his overarching mentorship, my family for their overwhelming love and support, and last but not least, Zavien,

This work was supported in part by a subcontract with Matrix Research, Inc. for research sponsored by AFRL under Prime Contract No. FA8650-14-D-1722, by the NSF Graduate Research Fellowship Program under Grant No. DGE-1451148, and by the University of Kansas Chancellor's Fellowship.

Contents

1 Introduction **1**

2 Signal Model **4**

2.1 Target Response 9

2.2 Clutter from an Airborne Platform 13

2.3 Receiver Thermal Noise 16

3 Multi-Waveform Space-Time Adaptive Processing **18**

4 Post Pulse Compression Multi-Waveform Space-Time Adaptive Processing **27**

4.1 Homogenization Filter Length 28

4.2 Number of Secondary Filters 34

4.3 μ-STAP and Pμ-STAP Performance Comparison 39

4.4 Pμ-STAP in High Fidelity Knowledge Aided Radar Architecture 44

5 Partially Adaptive Multi-Waveform Space-Time Adaptive Processing **50**

5.1 Element-Space Post-Doppler 54

5.2 Beam-Space Pre-Doppler 65

5.3 Beam-Space Post-Doppler 74

6 Conclusions **83**

List of Figures

2.1 Radar Datacube [1] 8

2.2 Clutter Patch in a Radar Scene [2] 14

2.3 3-element Array Traveling for 3 Pulses with a $\beta = 1$ [3] 15

2.4 Clutter Ridges [3], a) Stationary Platform, $\beta = 0$ b) Moving Platform, Spatial ambiguity, $\beta = .5$ c) Moving Platform, No ambiguity $\beta = 1$ d) Moving Platform, Doppler ambiguity $\beta = 2$ 16

3.1 Minimum Detectable Doppler of a Clairvoyant SINR 22

4.1 Primary and Secondary Homogenization Response for $BT = 5$ 30

4.2 Primary and Secondary Homogenization Response for $BT = B\tau/2 - 1$ 30

4.3 Primary and Secondary Homogenization Response for $BT = B\tau - 1$ 31

4.4 Primary and Secondary Homogenization Response for $BT = 2B\tau - 1$ 31

4.5 SINR Loss for Various Homogenization Filter Lengths 33

4.6 Average Improvement Factor for Various Homogenization Filter Lengths 34

4.7 SINR Loss at $0.5MN$ for Various Number of Secondary Filters in Homogeneous Clutter 35

4.8 SINR Loss at $2MN$ for Various Number of Secondary Filters in Homogeneous Clutter 36

4.9 Average Improvement Factor for Various Number of Secondary Filters in Homogeneous Clutter 37

4.10 SINR Loss at $0.5MN$ for Various Number of Secondary Filters in Heterogeneous Clutter 38

4.11 SINR Loss at $2MN$ for Various Number of Secondary Filters in Heterogeneous Clutter 38
4.12 Average Improvement Factor per Range Sample Intervals for Various Number of Secondary Filters in Heterogeneous Clutter 39
4.13 μ-STAP and Pμ-STAP SINR Loss at $0.5MN$ in Heterogeneous Clutter 40
4.14 μ-STAP and Pμ-STAP Average Improvement Factor in Heterogeneous Clutter . . 42
4.15 μ-STAP and Pμ-STAP SINR Loss at $0.5MN$ with Clutter Discrete in CUT 42
4.16 μ-STAP and Pμ-STAP Average Improvement Factor with Clutter Discrete in CUT 43
4.17 μ-STAP and Pμ-STAP SINR Loss at $0.5MN$ with Targets in Training Data 43
4.18 SINR Loss in KASSPER Range Sample 27 45
4.19 Average Improvement Factor in KASSPER Range Sample 27 46
4.20 SINR Loss in KASSPER Range Sample 236 46
4.21 Average Improvement Factor in KASSPER Range Sample 236 47
4.22 SINR Loss in KASSPER Range Sample 400 48
4.23 Average Improvement Factor in KASSPER Range Sample 400 48

5.1 Partially Adaptive Algorithms [3] 52
5.2 Recieve Processing Chain for Partial Adaptive μ-STAP 53
5.3 Primary and Secondary Homogenization Filter Responses for PCFM Waveform . . 54
5.4 ESPoD PRI-Staggered SINR Loss at $2ND_t$ in Heterogeneous Clutter 58
5.5 ESPoD PRI-Staggered Average Improvement Factor in Heterogeneous Clutter . . . 59
5.6 ESPoD Adjacent-Bin SINR Loss at $2ND_t$ in Heterogeneous Clutter 59
5.7 ESPoD Adjacent-Bin Average Improvement Factor in Heterogeneous Clutter . . . 60
5.8 ESPoD PRI-Staggered SINR Loss at $2ND_t$ with Clutter Discrete in CUT 61
5.9 ESPoD PRI-Staggered Average Improvement Factor with Clutter Discrete in CUT . 62
5.10 ESPoD Adjacent-Bin SINR Loss at $2ND_t$ with Clutter Discrete in CUT 62
5.11 ESPoD Adjacent-Bin Average Improvement Factor with Clutter Discrete in CUT . 63
5.12 ESPoD PRI-Staggered SINR Loss at $2ND_t$ with Targets in Training Data 64

5.13 ESPoD Adjacent-Bin SINR Loss at $2ND_t$ with Targets in Training Data 64
5.14 BSPrD Displace-Beam SINR Loss at $2D_sD_{t,1}$ in Heterogeneous Clutter 68
5.15 BSPrD Displace-Beam Average Improvement Factor in Heterogeneous Clutter . . 68
5.16 BSPrD Adjacent-Beam SINR Loss at $2D_sD_{t,1}$ in Heterogeneous Clutter 69
5.17 BSPrD Adjacent-Beam Average Improvement Factor in Heterogeneous Clutter . . 69
5.18 BSPrD Displace-Beam SINR Loss at $2D_sD_{t,1}$ with Clutter Discrete in CUT 70
5.19 BSPrD Displace-Beam Average Improvement Factor with Clutter Discrete in CUT 71
5.20 BSPrD Adjacent-Beam SINR Loss at $2D_sD_{t,1}$ with Clutter Discrete in CUT 72
5.21 BSPrD Adjacent-Beam Average Improvement Factor with Clutter Discrete in CUT 72
5.22 BSPrD Displace-Beam SINR Loss at $2D_sD_{t,1}$ with Targets in Training Data 73
5.23 BSPrD Adjacent-Beam SINR Loss at $2ND_t$ with Targets in Training Data 74
5.24 BSPoD PRI-Staggered/Displace-Beam SINR Loss at $2D_sD_{t,1}$ in Heterogeneous Clutter 76
5.25 BSPoD PRI-Staggered/Displace-Beam Average Improvement Factor in Heterogeneous Clutter 76
5.26 BSPoD Adjacent-Bin/Adjacent-Beam SINR Loss at $2D_sD_{t,1}$ in Heterogeneous Clutter 77
5.27 BSPoD Adjacent-Bin/Adjacent-Beam Average Improvement Factor in Heterogeneous Clutter 77
5.28 BSPoD PRI-Staggered/Displace-Beam SINR Loss at $2D_sD_{t,1}$ with Clutter Discrete in CUT 78
5.29 BSPoD PRI-Staggered/Displace-Beam Average Improvement Factor with Clutter Discrete in CUT 79
5.30 BSPoD Adjacent-Bin/Adjacent-Beam SINR Loss at $2D_sD_{t,1}$ with Clutter Discrete in CUT 79
5.31 BSPoD Adjacent-Bin/Adjacent-Beam Average Improvement Factor with Clutter Discrete in CUT 80

5.32 BSPoD PRI-Staggered/Displace-Beam SINR Loss at $2D_sD_{t,1}$ with Targets in Training Data 81
5.33 BSPoD Adjacent-Bin/Adjacent-Beam SINR Loss at $2D_sD_{t,1}$ with Targets in Training Data 81

List of Tables

2.1 Parameters in Signal-to-Noise Ratio 6

4.1 Simulated Test Flight 1 Parameters 33

4.2 Training Data Combinations in SINR Analysis of Number Secondary Filters . . . 35

4.3 Training Data Combinations in Performance Comparison 41

5.1 Simulated Test Flight 2 Parameters 54

5.2 Training Data Combinations in SINR Analysis of Partial Adaption 57

Chapter 1

Introduction

Airborne ground moving target indication (GMTI) is a radar application tasked with detecting moving targets in a radar scene. GMTI determines angular information from spatial signals received on an antenna array and Doppler information from multiple receive pulses. Due to the platform motion of the radar, a coupling of the spatial and Doppler dimensions occurs. In the early days of GMTI, this phenomena was corrected using algorithms such as displaced phase center antenna (DPCA) [4]. DPCA accounts for the platform motion by steering the receive array from pulse to pulse. The radar scene landscape can vary depending on weather, land, or littoral environments. In heterogeneous environments, detection performance for airborne GMTI becomes increasing difficult.

In a seminal paper by Brennen and Reed [5], space-time adaptive processing (STAP) was first introduced as a means to optimally cancel clutter through adaptive processing. STAP exploits the second-order statistics of temporal and spatial signals to nullify clutter. The original STAP formulation is based on the independent and identically distributed assumption (i.i.d) [6]. This assumes that the clutter has the same statistically characteristics for all fast-time samples [7]. In the presence of heterogeneous clutter, internal clutter motion, strong clutter discretes, and/or contaminated training data, STAP performance degrades due to its inability to accurately estimate an adaptive filter for sufficient clutter cancellation. The degradation in the filter estimate corresponds to a decrease in minimum detectable velocity and overall target detection performance. STAP is wildly researched topic [25-55] and is driven by developing ways to mitigate the effects of heterogeneous clutter and improve detection performance on the GMTI radar.

A new form of STAP called *multi-waveform space-time adaptive processing* (μ-STAP) was de-

veloped to address heterogeneous clutter [8; 9; 10]. μ-STAP exploits decorrelation of training data used to form a covariance matrix by implementing secondary pulse compression filters to enforce homogeneity. In addition, multiple space-time datacubes are generated from these filters creating a multiplicative increase in the number of samples used to form a covariance thereby further accurately estimating the adaptive filter. μ-STAP was initially developed as a form of multi-input multi-output (MIMO). The MIMO formulation describes the emission of multiple transmit waveforms on a single aperture. The secondary waveforms are designed to have low-cross correlation with the primary waveform. The additional pulse compression filters homogenized the receive data to be more identically distributed. Upon further analysis, the performance benefit of μ-STAP was attributed to the coherent integration of the receive processing. This lead to the development of single-input multi-output (SIMO) μ-STAP which transmits only a single waveform, similar to STAP, and performs receive processing using the same secondary pulse compression filters as if they were transmitted.

Legacy radar systems that perform pulse compression prior to analog-to-digital conversion can not benefit from μ-STAP. Post pulse compression μ-STAP (Pμ-STAP) is a new form of SIMO μ-STAP that would allow legacy radar systems to benefit. Pμ-STAP homogenizes space-time signals after coherent integration and discretization of fast-time samples. The secondary filters do not need a priori knowledge of the transmit waveform to perform homogenization.

All of the STAP algorithms mentioned have high computation cost due to a adaptive filter needing to be developed for every fast-time sample thereby hindering real-time application. Partially adaptive algorithms have been implemented with traditional STAP to facilitate real-time application [3]. The class of μ-STAP algorithms have yet to be examined for real-time application. For the prospect of implementing on legacy systems, Pμ-STAP would require a similar analysis. Therefore, well-known partial adaptive techniques will be examined with Pμ-STAP for the prospect of real-time application in legacy radar systems.

The purpose of this report is to analyze the Pμ-STAP algorithm, compare and contrast to μ-STAP performance in heterogeneous clutter, and determine if it is feasible for real-time application.

The organization of the report is as follows. In Chapter 2, a signal model of fast-time, slow-time, and spatial signals for airborne radar is presented. Chapter 3 provides an overview of STAP and μ-STAP. Chapter 4 introduces post pulse compression μ-STAP by providing analysis of the homogenization filters and performance in heterogeneous clutter. Chapter 5 reviews will-known partially adaptive techniques then analyzes them with Pμ-STAP.

Chapter 2

Signal Model

An airborne radar performing GMTI detects a target's range, velocity, and angular location by exploiting fast-time, temporal, and spatial signals, respectively. To implement airborne GMTI, a pulse-Doppler radar is operated from a phased array. A pulse is emitted from the radar illuminating an area on the Earth's surface. The slant range from the radar to a scatterer in the scene is

$$R = \frac{c\Delta T}{2} \tag{2.1}$$

where c is the speed of light and ΔT is the round trip delay [1]. The interval between pulses is the *pulse repetition interval* (PRI). The rate pulses are emitted per second is the *pulse repetition frequency* and is inversely proportional to the PRI

$$f_r = \frac{1}{T_r} \tag{2.2}$$

where f_r is PRF and T_r is PRI. The maximum unambiguous range is

$$R_{max} = \frac{c}{2f_r}. \tag{2.3}$$

Range ambiguity occurs when a pulse from one PRI returns during another. If this aliasing occurs, the range of the pulse return can be inaccurately determined. GMTI radars are typically designed to have low PRF to prevent range ambiguities [4].

Another ambiguity is two closely spaced pulse returns within one PRI. For an unmodulated pulse, a smaller pulse duration provides greater *range resolution* between pulse returns. However,

a smaller pulse width comes at the cost of transmit power on target that a longer pulse duration provides. Modulation of the pulse will produce range resolution and energy on target unlike a unmodulated pulse. The operation of modulating a pulse is called *pulse compression*. Pulse compression waveforms modulate either in amplitude, phase, or frequency [1]. Frequency modulated waveforms will be considered throughout. Examples of frequency modulated waveforms are linear (LFM), non-linear (NLFM)[11], and polyphase-coded (PCFM)[12; 13] among others. A pulse compression waveform $s(t)$ is represented as .

$$s(t) = u(t)e^{j(2\pi f_c t+\varphi)} \tag{2.4}$$

where $u(t)$ is the complex envelope, f_c is the transmit center frequency, and φ is phase. The waveform is defined over a pulse duration τ where $0 \leq t \leq \tau$ [3]. The duration of the pulse is a portion of PRI. The ratio between the pulse duration and PRI, is the *duty cycle*. The complex envelope is defined by the type of waveform used [11].

The pulse return signals are passed through a *match filter* that maximizes the signal-to-noise ratio (SNR). The match filter is defined as

$$h(t) = \frac{s^*(-t)}{\|s(t)\|^2} \tag{2.5}$$

where $(\bullet)^*$ denotes complex conjugation and $\|\bullet\|$ denotes norm [11]. Note that the duration of the match filter is equivalent to the waveform. The autocorrelation of the FM waveform with its match filter provides a narrower 3dB width than a unmodulated pulse. Signal-to-noise ratio (SNR) for an single unmodulated pulse is defined using the radar range equation [1] as

$$\zeta = \frac{P_t G_t G_r \lambda_c^2 \sigma_{RCS}}{(4\pi)^3 P_n L_s R_t^4} \tag{2.6}$$

The parameters within (2.6) are defined in Table 2.1. Systems losses include transmit loss, receiver

Table 2.1: Parameters in Signal-to-Noise Ratio

P_t	Peak transmit power
G_t	Transmit antenna gain
G_r	Receive antenna gain
λ_c	Operating wavelength
P_n	Thermal noise power spectral density
L_s	System loss
R_t	Range from radar to target

loss, atmospheric loss, and signal processing loss [1]. Applying pulse compression increases the SNR equation

$$\zeta_{pc} = \zeta B \tau \tag{2.7}$$

where B is the pulse modulation bandwidth [1].

The waveform is transmitted coherently over a *uniformly-spaced linear array* (ULA) with N_h horizontal elements. Also, a vertically beamformed *uniformly-spaced planer array* (UPA) with N_v vertical elements and N_h horizontal elements can be used. The total number of elements for a UPA is $N = N_v N_h$. UPAs are useful since elevation can be determine from vertical elements and azimuth from horizontal elements. Typically, airborne GMTI radar favors azimuthal angular information for target location due to the downward orientation of the array look direction. Beams are formed over the vertical elements and the horizontal elements are kept the same making $N = N_h$ beams. Therefore, a ULA will be consider throughout with the prospect of using a UPA.

Coherent transmission of the same pulse on all array elements forms a single transmit beam. The number of elements, type of antenna elements, and spacing each contribute to the *beampattern* emitted from the radar. The number of array elements is inversely proportional to the 3dB beamwidth also known as the spatial resolution. The transmit waveform has following response

$$\tilde{s}(t, \theta, \theta_{look}) = s(t)\, b(\theta, \theta_{look}) \tag{2.8}$$

for transmit beampattern $b(\theta, \theta_{look})$ with dependencies on spatial angle, θ, and look angle, θ_{look} [8; 9; 10]. The distinction between spatial angle and look angle is how the beam is steered. For spatial

angle, the beam is electronically steered by uniformly offsetting the coherence of the waveform as it emits from each element. The look angle is the physical steering of array relative to a radar emitting abeam to the aircraft. The look angle is not typically altered. In addition, the spatial angle is pointing in direction of the look angle, i.e. $\theta = \theta_{look}$. Therefore, θ_{look} will be subsumed from here out.

After interaction with the radar scene, multiple pulse returns from the scene are received on each element of the array. The radar collects M pulses in a *coherent processing interval*. The duration of the CPI is $T_{CPI} = MT_r$. Effectively a collection of M successive PRI. The number of pulses in a CPI dictate the Doppler resolution between two targets with close radial velocities. For the mth received pulse, the receive signal collected on the nth element is

$$y(m,n,t) = \sum_{\omega}\sum_{\theta}\left[\tilde{s}(t,\theta) * x(t,\omega,\theta)\right] e^{j(m\omega+n\theta)} + v(t) \tag{2.9}$$

where ω is Doppler frequency, θ is spatial frequency, $x(t,\omega,\theta)$ is the complex scatterers in the scene, and $v(t)$ is thermal noise. Pulse compression is applied to the receive signal using the match filter

$$z(m,n,t) = h(t) * y(m,n,t). \tag{2.10}$$

Each array element down-converts and digitizes each receive time-delayed return signal within a PRI to form fast-time (range) samples. Collection of L fast-time samples for each pulse and element combination, produces the pulse compressed datacube shown in Figure 2.1. Define a single range sample ℓ (also called a range bin) corresponding to a discretized sample of a time-delay received signal. For a received CPI, successive PRI returns are oriented into slow-time samples. The start of a new PRI creates a new slow-time sample. For a single range sample, the

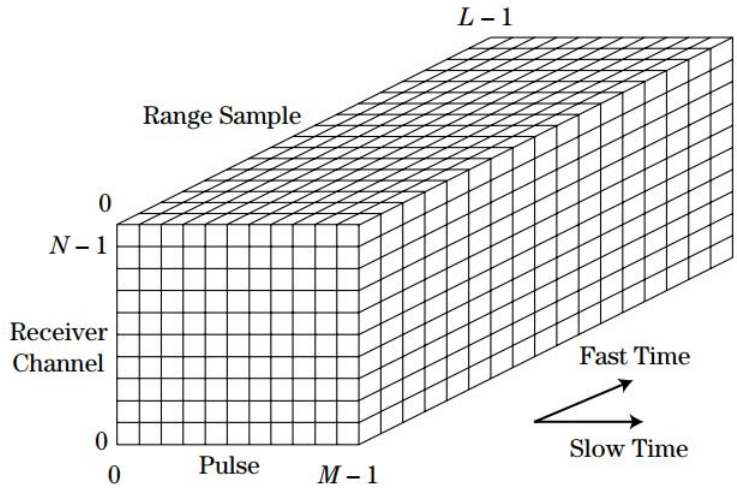

Figure 2.1: Radar Datacube [1]

received slow-time samples for each element forms the $M \times N$ space-time data matrix

$$\mathbf{Z}(\ell) = \begin{bmatrix} z(0,0,\ell) & \dots & z(0,N-1,\ell) \\ \vdots & \ddots & \vdots \\ z(M-1,0,\ell) & \cdots & z(M-1,N-1,\ell) \end{bmatrix} = \begin{bmatrix} \mathbf{z}_0(\ell) & \cdots & \mathbf{z}_{N-1}(\ell) \end{bmatrix} \tag{2.11}$$

where $\mathbf{Z}(\ell) \in \mathbb{C}^{M \times N}$ [3]. Collecting L fast-time samples forms the $M \times N \times L$ space-time datacube. The space-time matrix is vectorized into a $MN \times 1$ space-time snapshot by stacking the columns of (2.11)

$$\mathbf{z}(\ell) = \begin{bmatrix} \mathbf{z}_0(\ell) \\ \vdots \\ \mathbf{z}_{N-1}(\ell) \end{bmatrix}. \tag{2.12}$$

Scattered returns within every space-time snapshot will always contain clutter but may or may not contain a target. Clutter is the unwanted returns that are not pertaining to GMTI goal [1]. For GMTI radar, clutter are all non-moving returns or very slow moving returns which typically is the Earth's surface. Clutter for an airborne radar is detailed in Section 2.2. The two hypotheses for

target detection are

$$\begin{aligned} &\text{Target Absent - } h_0 : \mathbf{z}(\ell) = \mathbf{x}_c(\ell) + \mathbf{v}(\ell) \\ &\text{Target Present - } h_1 : \mathbf{z}(\ell) = \mathbf{x}_t(\ell) + \mathbf{x}_c(\ell) + \mathbf{v}(\ell) \end{aligned} \tag{2.13}$$

where $\mathbf{x}_t(\ell)$ is the target response, $\mathbf{x}_c(\ell)$ is the clutter response and $\mathbf{v}(\ell)$ is thermal noise for the ℓth range sample. A covariance matrix is used to characterize the second-order statistics of the elements in the space-time snapshot. The formal definition of covariance matrix is

$$\mathbf{R} = E\left[\mathbf{x}\mathbf{x}^H\right] - E[\mathbf{x}](E[\mathbf{x}])^H \tag{2.14}$$

where $(\bullet)^H$ denotes conjugate transposition. Typically, the mean is assumed to be $E[\mathbf{x}] = 0$. The diagonal terms are the variance of each element and off-diagonal terms are autocorrelations of different delays [2]. The covariance matrix is positive-definite Hermitian. The covariance matrix of the target absent hypothesis (h_1) is

$$\begin{aligned} \mathbf{R}(\ell) &= E\left[\mathbf{z}_{h_1}(\ell)\mathbf{z}_{h_1}^H(\ell)\right] \\ &= E\left[\mathbf{x}_t(\ell)\mathbf{x}_t^H(\ell)\right] + E\left[\mathbf{x}_c(\ell)\mathbf{x}_c^H(\ell)\right] + E\left[\mathbf{v}(\ell)\mathbf{v}^H(\ell)\right] \\ &= \mathbf{R}_t(\ell) + \mathbf{R}_c(\ell) + \mathbf{R}_v(\ell). \end{aligned} \tag{2.15}$$

This characterizes the statiscally nature of the targets, clutter and noise which will be examined further in the following subsections. Later, it will be shown that the covariance matrix for target absent scenario (h_0) can be used to nullify clutter (Chapter 3).

2.1 Target Response

Targets are moving objects in the scene traveling above a radial velocity of interest. A target velocity directly relates to a *Doppler frequency*. The Doppler effect is a common phenomenon that modulates the waveform impinging on it to a different frequency. The direction and speed at which

the target is moving determines Doppler [1]. Doppler frequency is expressed as

$$f_d = \frac{2v_t}{c} f_c = \frac{2v_t}{\lambda_c} \tag{2.16}$$

where v_t is a target's radial velocity. Doppler is positive if the illuminated target is moving towards the radar and negative if moving away. If the scatterer is not moving, it has a Doppler frequency of $f_d = 0$. The maximum unambiguous Doppler frequency of a pulse-Doppler radar is

$$f_{d,\max} = \pm \frac{f_r}{2} \tag{2.17}$$

Ambiguity in this context is the point at which velocities become overlapping due to the Doppler frequency wrapping around the spectrum [1]. Doppler frequency is often expressed in a normalized as

$$\omega_d = \frac{f_d}{f_r} = f_d \cdot T_r \tag{2.18}$$

Interestingly, the Doppler of an target is seen across slow-time samples as a linear phase progression. Since frequency is the time derivative of phase, the slope of the phase progression corresponds to a Doppler frequency. A target's phase progression across slow-time samples is described by its *temporal steering vector*

$$\mathbf{c}_t(\omega_d) = \begin{bmatrix} 1 & e^{j2\pi\omega_d} & \dots & e^{j2\pi(M-1)\omega_d} \end{bmatrix}^T \tag{2.19}$$

where $(\bullet)^T$ denotes transposition. This vector structure is the called the Vandermonde structure where each consecutive element is a multiple of the preceding element increased by a single integer [2]. In this case, the integer corresponds to the pulse number and normalized Doppler frequency leading to a sampled sinusoidal vector. Although, a constant PRF is considered for the form of the temporal steering vector, it can be modified to staggered PRF formulations which causes a non-linear phase progression.

In addition to obtaining velocity information, MTI radar determines a target angular location

in the scene by distinguishing reflections direction-of-arrival (DoA) using digital beamforming techniques on the ULA [2]. Consider a N-element ULA receives a reflected plane wave from a point target in the scene. The elements spaced d meters apart at a elevation of ϑ_t and azimuth ϕ_t on the aircraft platform. The length of the array is $L = Nd$. The spacing between elements, d, is best keep at $\lambda_c/2$ to minimize the effect of grating lobes [4]. The plane wave impinges on each array element with a time delay from element to element. Based on the operating frequency and spacing, the target *spatial frequency* is defined as

$$\theta_t = \frac{d}{\lambda_c}\cos(\vartheta_t)\sin(\phi_t) = \frac{d}{\lambda_c}\cos(\phi_c) \tag{2.20}$$

where cone angle is ϕ_c. Since the array is uniformly spaced, the time delay of the impinging plane wave from element to element is constant. The delay corresponds to a phase that progresses linearly across the array. Therefore, the target phase progression across elements is defined as *spatial steering vector* is

$$\mathbf{c}_s(\theta_t) = \begin{bmatrix} 1 & e^{j2\pi\theta_t} & \dots & e^{j2\pi(N-1)\theta_t} \end{bmatrix}^T. \tag{2.21}$$

A plane wave received at boresight is received by all elements at the same time and has a spatial, $\theta = 0$. Any plane wave offset of boresight will have a positive or negative frequency depending on if it is received from the left or right, respectively. The Vandermonde structure of the temporal and spatial steering vectors is an embodiment of their coherence in their respective domain [2]. To extract Doppler and spatial frequency, a fast Fourier transform (FFT) is employed to test all possible phase slopes. In the slow-time dimension this process is called *Doppler processing*. The Doppler resolution on target after processing is

$$\Delta f_d = \frac{f_r}{T_{CPI}} = \frac{1}{MT_r} \tag{2.22}$$

In the spatial dimension, utilizing the FFT is called *receive beamforming*. The spatial resolution is

defined by the 3dB beamwidth as

$$\Delta\theta_t = \frac{a_{sw}\lambda_c}{L_{array}} \tag{2.23}$$

where a_{sw} is the beam-broading factor and L_{array} is the length of the array [2].

The target response present in (2.13) has a amplitude response, α, a Doppler frequency, ω_d, and spatial frequency, θ_t. The target response for the target present hypothesis is

$$\mathbf{x}_t(\omega_d, \theta_t, \ell) = \alpha(\ell)\,\mathbf{c}_{st}(\omega_d, \theta_t) \tag{2.24}$$

where $\mathbf{c}_{st}$ is a coupling of the spatial and temporal steering vectors called the *space-time steering vector*. The space-time steering vector is defined as

$$\mathbf{c}_{st}(\omega_d, \theta_t) = \mathbf{c}_t(\omega_d) \otimes \mathbf{c}_s(\theta_t) \tag{2.25}$$

where $\otimes$ denotes Kronecker product [3].

A mismatch between the true target steering vector and estimated steering vector will occur. This is a form of *straddling loss* [2]. This causes a decrease in SNR. Straddling loss can be mitigated by increasing the number of frequency samples through zero-padding the FFT. In both dimensions, tapering is often employed to minimize the sidelobes at the cost of decreasing resolution. Implementing tapering to (2.25) is

$$\widehat{\mathbf{c}}_{st}(\omega_d, \theta_t) = (\mathbf{c}_t(\omega_d) \odot \mathbf{b}) \otimes (\mathbf{c}_s(\theta_t) \odot \mathbf{a}) \tag{2.26}$$

where $\mathbf{b}$ is a $M \times 1$ Doppler taper, $\mathbf{a}$ is a $N \times 1$ spatial taper and $\odot$ denotes Hadamard product. The minimal amount of frequency samples in Doppler processing is the number of pulses. Similarly, beamforming minimal amount is the number of elements in the array.

The target covariance matrix at ℓth range sample is

$$\begin{aligned}\mathbf{R}_t(\ell) &= E\left[\mathbf{x}_t(\omega,\theta,\ell)\mathbf{x}_t^H(\omega,\theta,\ell)\right] \\ &= \sigma_t^2(\ell)\,\zeta_t\mathbf{c}_{st}(\omega_d,\theta_t)\mathbf{c}_{st}^H(\omega_d,\theta_t)\end{aligned} \tag{2.27}$$

where σ_t^2 is the target power [3].

2.2 Clutter from an Airborne Platform

Clutter is the unwanted illuminated scatterers from the Earth (land, sea, weather) and static man-made objects (such as buildings) that surrounds targets. For radar mounted on a stationary platform, clutter is static and corresponds to a Doppler frequency of zero. Dynamic clutter (such as trees blowing in the wind or ocean waves), called *internal clutter motion* (ICM), causes a spread in clutter Doppler bandwidth [4]. Spatially, the clutter scatterers return from all DoAs. For an airborne radar, the clutter is still located in all spatial angles but has Doppler frequency relative to the motion of the radar platform causing Doppler center frequency of the clutter to shift. This motion-induced spectral spread and ICM causes challenges in target detection [4; 14].

Consider the ULA is mounted parallel to the aircraft illuminating abeam onto a scene. The beam swath illuminating the scene can be segmented into range and angle *clutter patches* shown in Figure 2.2. A clutter patch is a aggregate of complex, coherent reflections from smaller scatterers. The ground clutter return for an airborne radar at the ℓth range bin [2]

$$\mathbf{x_c}(\omega_c,\theta_c,\ell) = \sum_{i=0}^{N_c-1}\sum_{j=0}^{N_a-1}\mathbf{a}_{ij}(\ell)\odot\mathbf{c}_{st,ij}(\omega_c,\theta_c) \tag{2.28}$$

where N_c is statistically independent clutter patches and N_a is the number of unambiguous ranges. Clutter in positive angular frequency (in front of the aircraft) will appear to be moving toward the radar and vice versa. The perceived dynamic nature of ground clutter causes a coupling of the spatial and temporal signals.

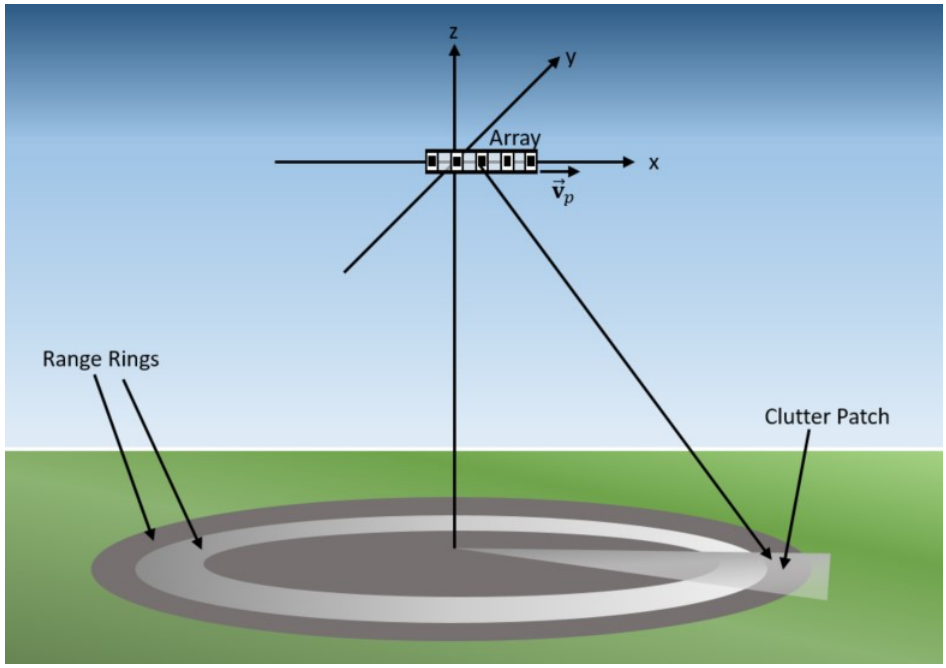

Figure 2.2: Clutter Patch in a Radar Scene [2]

More specifically, clutter Doppler frequency becomes a function spatial frequency, platform velocity, PRI (or PRF), and element array spacing [3]

$$\omega_c = \frac{2v_p T_r}{d}\theta_c. \tag{2.29}$$

This can be subsummed into a single coefficient β which is the interelement spacing traveled during one PRI

$$\beta = \frac{2v_p T_r}{d}. \tag{2.30}$$

In Figure 2.3, an illustrative example of β is presented for a three element array traveling through space for three pulses.

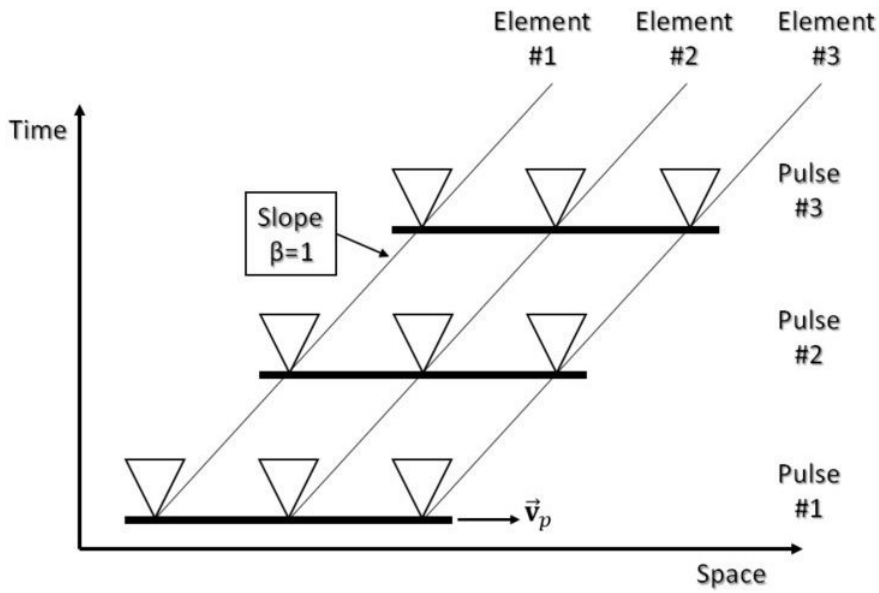

Figure 2.3: 3-element Array Traveling for 3 Pulses with a $\beta = 1$ [3]

In Figure 2.4, a two-dimensional power spectral density of clutter for multiple β values is presented. Note the ridge that forms in the two-dimensional clutter power spectral density [2] due to coupling. For a $\beta = 1$, the Doppler and angle are unambiguous. When $0 < \beta < 1$, the data is becomes spatially ambiguous. When $\beta > 1$ it becomes Doppler ambiguous [3]. Without ICM, the clutter bandwidth extends between $\pm(2v_p \cos\phi_c)/\lambda_c$ as a function of range. Longer ranges correspond to smaller cone angles leading to wider bandwidths and vice versa [14]. ICM further extends the bandwidth.

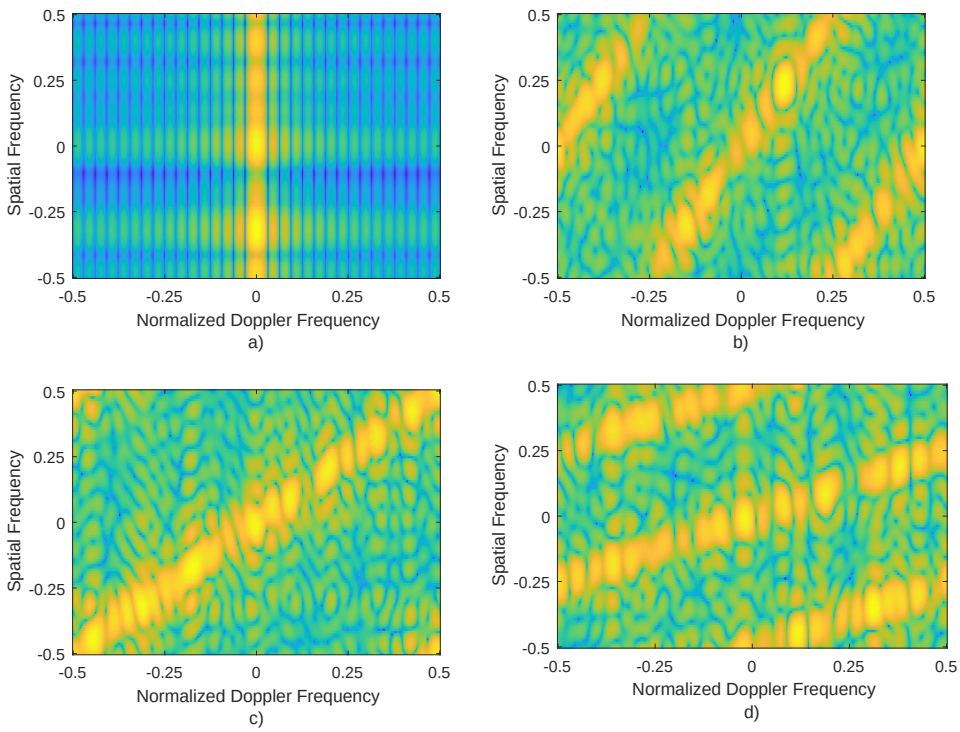

Figure 2.4: Clutter Ridges [3], a) Stationary Platform, $\beta = 0$ b) Moving Platform, Spatial ambiguity, $\beta = .5$ c) Moving Platform, No ambiguity $\beta = 1$ d) Moving Platform, Doppler ambiguity $\beta = 2$

The clutter covariance matrix is

$$\mathbf{R}_c(\ell) = \sum_{i=0}^{N_c-1} \sum_{j=0}^{N_a-1} \mathbf{A}_{ij}(\ell) \odot \mathbf{c}_{st}(\omega_c, \theta_c) \mathbf{c}_{st}^H(\omega_c, \theta_c) \tag{2.31}$$

where $\mathbf{A}_{ij}(\ell)$ is the clutter space-time amplitude correlation [2]. If the amplitudes are correlated from pulse-to-pulse and channel-to-channel, then $\mathbf{A}_{ij}(\ell) = \sigma_{c,ij}^2(\ell)\mathbf{1}_{MN}$. The matrix $\mathbf{1}_{MN}$ is a $MN \times MN$ matrix of all ones.

2.3 Receiver Thermal Noise

In the universe, any blackbody with a temperature above absolute zero generates random motion of charged particles known as thermal noise. For a radar operating at in the microwave band of

the electromagnetic spectrum internal thermal noise dominates over environmental thermal noise [15]. Assuming elements from ULA are independent and mutually uncorrelated, the noise correlation between two elements is [3]

$$E\left[v_{mn_1}v_{mn_2}^*\right] = \sigma_v^2\delta_{n_1-n_2} \tag{2.32}$$

Furthermore, assume the samples for a single element are temporally uncorrelated from pulse to pulse, then the noise correlation between two pulses is

$$E\left[v_{m_1n}v_{m_2n}^*\right] = \sigma_v^2\delta_{m_1-m_2} \tag{2.33}$$

In both cases, σ_v^2 is thermal noise power and δ is the Kronecker delta defined as

$$\delta(m) = \begin{cases} 1, \ m = 0 \\ 0, \ m \neq 0 \end{cases} \tag{2.34}$$

Since the elements and pulses are uncorrelated, the covariance matrix of the space-time noise is [3]

$$\begin{aligned} \mathbf{R}_v(\ell) &= E\left[\mathbf{v}(\ell)\mathbf{v}^H(\ell)\right] \\ &= \sigma_v^2\mathbf{I}_{MN} \end{aligned} \tag{2.35}$$

where $\mathbf{I}_{MN}$ is a $MN \times MN$ identity matrix.

Chapter 3

Multi-Waveform Space-Time Adaptive Processing

The angle-Doppler coupling described in the last chapter can cause deleterious effects in detection performance. The platform-motion effects causes a clutter Doppler frequency shift and increases the clutter Doppler bandwidth. Slower moving targets close to the clutter Doppler frequencies will be harder to detect. MTI filters were originally developed combat it.

One of the earliest forms of clutter cancellation that atones for the frequency shift is displace-phase center antenna (DPCA). The technique would compensate by electronically steering the phase array dependent on the platform velocity and pulse repetition frequency [14]. Another method is the time-averaged-clutter coherent airborne radar (TACCAR) developed by MIT Lincoln Laboratory. TACCAR essentially shifts the clutter spectrum back to zero-Doppler [4].

Although these techniques are indeed useful in the cancellation of clutter, they are not optimal. In a seminal paper by Breenan and Reed [5], a theoretically analysis of adaptive signal processing was presented. In another paper by Reed, Mallet, and Breenan, the introduction of adaptive processing spatial signals from an array and temporal signals from multiple pulses was presented [16]. The launch of digital era in the late 20th century lead to the proliferation of digital signal processing. Combining digital age advancement with the optimal, adaptive receive processing to combat motion-induced clutter effects lead to the birth of *space-time adaptive processing* [14].

Space-time adaptive processing (STAP) is an optimal two-dimensional clutter cancellation technique for airborne radar. STAP maximizes signal-to-interference-plus-noise ratio (SINR) by adapting to the space-time clutter returns [3; 2]. The improvement in SINR increases the minimum detectable velocities. This allows for increase detection of slow moving targets.

Consider the target absent (null) hypothesis in (2.13) which describes full knowledge of the

clutter and noise without any targets. A $MN \times MN$ interference covariance matrix for each range sample is formed from the null hypothesis[3]

$$\mathbf{R}_o(\ell) = E\left[\mathbf{z}_{h_0}(\ell)\mathbf{z}_{h_0}^H(\ell)\right]. \tag{3.1}$$

The interference covariance is optimal (also called clairvoyant) since it completely characterizes the space-time clutter. The optimal maximum SINR adaptive filter is developed using the clairvoyant covariance matrix and clutter space-time steering vectors to form a adaptive angle-Doppler filter[3]

$$\mathbf{w}_o(\omega,\theta,\ell) = \mathbf{R}_o^{-1}(\ell)\mathbf{c}_{st}(\omega,\theta). \tag{3.2}$$

The covariance matrix will place frequency nulls at Doppler and spatial frequencies corresponding to the clutter. The maximum number of nulls that can be placed is the *degrees of freedom* (DoF), which is MN for STAP. Typically, a single spatial frequency is examined over the entire Doppler spectrum. The STAP adaptive filter can also be presented as a minimum variance space-time beamformer, generalized sidelobe canceller [2], and maximum SNR [14]. The covariance is optimal under the maximum likelihood estimator [17].

These are all within the class of sample matrix inversion (SMI) techniques [6] and a covariance matrix of this form is called a *sample covariance matrix*. Other classes include QR-decomposition and subspace sample matrix inversion [3].

Since the clutter and noise has been characterized, application of the STAP filter is performed to the target present hypothesis to yield target-only response.

$$\alpha(\omega,\theta,\ell) = \mathbf{w}_o^H(\omega_c,\theta_c,\ell)\mathbf{z}(\ell) = \mathbf{c}_{st}^H(\omega_c,\theta_c)\mathbf{R}_o^{-1}(\ell)\mathbf{z}(\ell) \tag{3.3}$$

This response is known as the test statistic and is feed through a detector [3]. Square-law and constant false alarm rate [1] detectors are typically used.

Perfect knowledge of the optimal covariance matrix can not be known. The terrain must be

statistically modeled for the covariance. Take sea clutter for example in the detection of a boat. Depending on a storm or time of the year, the rapid nature of the waves may change. Another example is a littoral environment where the flight path along a coast must be completely characterized in order to have the best covariance. Too many natural variables exist within the clutter to be modelled perfectly. Error in prediction of the clutter can lead to an incorrect covariance matrix. The best way to incorporate the environment into the covariance is by estimating it using spatial and temporal captured return signals [3]. Fortunately, their is an abundance of clutter compared to targets and the majority of the fast-time snapshots will correspond to the null hypothesis. One form of interference covariance estimation is *sliding window processing* (SWP):

$$\hat{\mathbf{R}}\left(\ell_{CUT}\right) = \frac{1}{n\left(L\right)} \sum_{\substack{\ell \in L \\ \ell \neq \ell_{CUT}}} \mathbf{z}\left(\ell\right) \mathbf{z}^{H}\left(\ell\right) \tag{3.4}$$

The ℓth range cell being estimated is the *cell-under-test* (CUT). Recall, L is the number of range cells after discretization. The CUT and samples contiguous to the CUT called *guard cells* are removed from the covariance estimation to prevent self-cancellation. If the CUT and guard cells were included, it would be similar to using the target present hypothesis for a optimal covariance in (3.1) thereby causing some self-cancellation. After removal of the CUT and guard cells, the remaining cells within L is called the *training data* or *sample support* (in most literature this data is referred to as secondary data). The cardinality of L, $n\left(L\right)$, describes the number of training data samples after removal of guard cells and CUT.

Another technique for covariance estimation is *block processing*. Here, one covariance matrix is formed for multiple consecutive samples (a block) of data. Block processing computation speed is increased, the accuracy of estimation of the covariance matrix is decreased. Block processing is commonly used for censoring techniques to remove cells that are statistical outliers to the CUT.

The primary metric used to analyze the adaptive filter is SINR [3]. The test statistic described in (3.3) can be expanded using the target present hypothesis from (2.13) such that $\hat{\alpha}\left(\theta,\omega\right) = \mathbf{w}^{H}\left(\ell,\theta,\omega\right)\mathbf{x}_{t}\left(\ell\right) + \mathbf{w}^{H}\left(\ell,\theta,\omega\right)\left(\mathbf{x}_{c}\left(\ell\right) + \mathbf{v}\left(\ell\right)\right)$. The signal power is defined as the $P_{s} = \left|\mathbf{w}^{H}\left(\ell,\theta,\omega\right)\mathbf{x}_{t}\left(\ell\right)\right|^{2}$

and interefernce-plus-noise power as $P_n = \left|\mathbf{w}^H(\ell,\theta,\omega)(\mathbf{x}_c(\ell)+\mathbf{v}(\ell))\right|^2$. The ratio of these powers defines the SINR [3]

$$\begin{aligned}\mathrm{SINR}(\omega,\theta,\ell) = \frac{P_s}{P_n} &= \frac{\left|\mathbf{w}^H(\omega,\theta,\ell)\,\mathbf{c}_{st}(\omega,\theta)\right|^2}{\mathbf{w}^H(\omega,\theta,\ell)\,\mathbf{R}_o(\ell)\,\mathbf{w}(\omega,\theta,\ell)} \\ &= \frac{\left|\mathbf{c}_{st}^H(\omega,\theta)\,\hat{\mathbf{R}}^{-1}(\ell)\,\mathbf{c}_{st}(\omega,\theta)\right|^2}{\mathbf{c}_{st}^H(\omega,\theta)\,\hat{\mathbf{R}}^{-1}(\ell)\,\mathbf{R}_o(\ell)\,\hat{\mathbf{R}}^{-1}(\ell)\,\mathbf{c}_{st}(\omega,\theta)}\end{aligned} \tag{3.5}$$

The SINR metric essentially quantifies how much the estimated covariance matrix deviates from the optimal covariance. Assuming perfect estimation of the covariance matrix, i.e. $\hat{\mathbf{R}}(\ell) = \mathbf{R}_o(\ell)$ yields the optimal (maximum) SINR defined as

$$\mathrm{SINR}_{opt}(\omega,\theta,\ell) = \mathbf{c}_{st}^H(\omega,\theta)\,\mathbf{R}_o^{-1}(\ell)\,\mathbf{c}_{st}(\omega,\theta) \tag{3.6}$$

Due to the necessity of the optimal covariance in SINR, adaptive filter performance is primarily tested in simulation. To see the amount of SINR loss, it is normalized by space-time SNR

$$\eta(\omega,\theta) = \frac{SINR(\omega,\theta)}{SNR_o} \tag{3.7}$$

where $SNR_o = MN\xi$ [3]. As previously mentioned, $\theta = \theta_{look}$ will be sub-summed and the algorithm will search over the Doppler spectrum.

A couple more metrics used to analyze performance of a STAP filter are improvement factor and minimum detectable velocity. The improvement factor is the ratio of two SINR responses. The ratio of SINR to optimal SINR is typically used.

$$IF(\omega) = \frac{SINR(\omega)}{SINR_o(\omega)} \tag{3.8}$$

The *minimum detectable Doppler* (MDD) is the lowest Doppler before a predetermined SINR loss

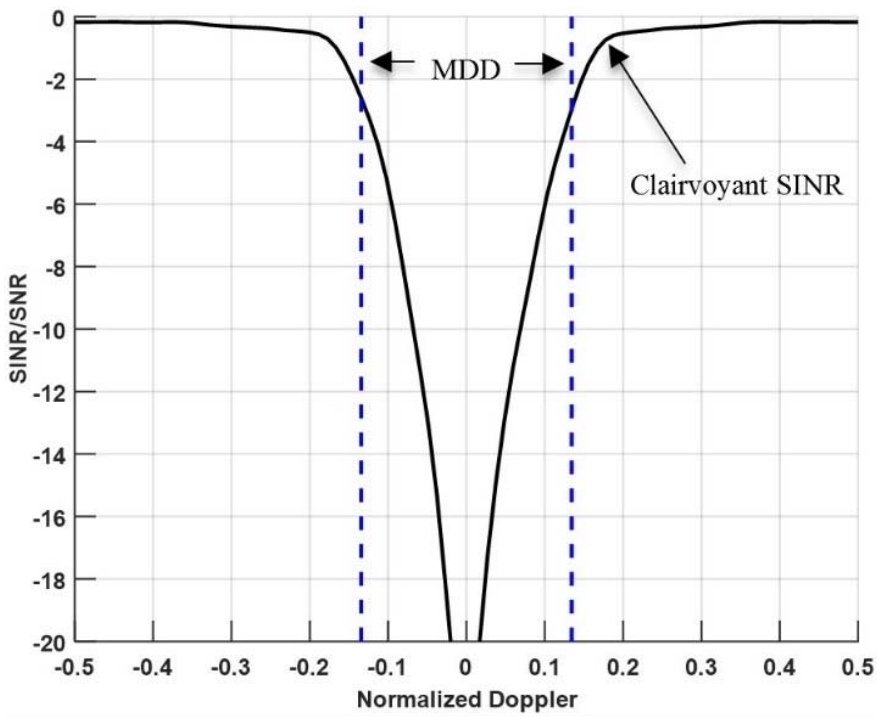

Figure 3.1: Minimum Detectable Doppler of a Clairvoyant SINR

is unacceptable (typically $\eta = 3dB$). Define ω_{min} as the MDD

$$\omega_{\min}(\eta) = \frac{1}{2}(\omega_U(\eta) - \omega_L(\eta)) \tag{3.9}$$

where $\omega_L(\eta)$ and $\omega_U(\eta)$ where upper and lower frequencies MDD frequencies. The minimal detectable velocity is simply found multiplying MDD by half wavelength. In Fig. 3.1, an example of MDD at $\omega_{min}(\eta = 3dB)$ for a arbitrary clairvoyant SINR is presented

In [8; 9; 10], a new form of the improvement factor as a function range sample intervals as a worst case SINR over Doppler frequencies outside of clutter notch. A similar metric is introduced called *average improvement factor* for detectable velocities

$$AIF(n(L)) = E_\omega\left[\frac{SINR(\omega \geq \omega_{\min}(\eta), n(L))}{SINR_o(\omega \geq \omega_{\min}(\eta))}\right]. \tag{3.10}$$

The frequencies greater than the MDD, $\omega \geq \omega_{\min}(\eta)$, is determined using the optimal SINR at

$\eta = 3dB$. The SCM from (3.4) can be estimated with different number of training data samples, $n(L)$. Likewise, STAP SINR is will also be determined based on the $n(L)$. The number of range samples is increase by $n(L) = 2, 4, \ldots, 2MN$ to insert a single range sample on each side of the CUT as more samples are added to the training data. Next, SINR performance over all Doppler frequencies outside clutter notch is averaged.

STAP research is driven by developing robust techniques to increase the accuracy of covariance estimation which, in turn, will provide more accurate clutter cancellation. Reed, Mallet, and Breenen provided a theoretical bound to the amount of training data that is needed to have an SINR loss within 3dB of the optimal [6]. Accordingly, the loss between estimated covariance related to the optimal covariance is beta-distributed with the following mean

$$E[\eta] = \frac{L+2-MN}{L-1} \tag{3.11}$$

Solving for L, the amount of training data to have at less a 3dB loss, must be $L = 2MN - 3$ known as the Reed, Mallet, Breenen (RMB) rule. Recall that number of DoF is MN. The rule is typically generalized to $L = 2MN$

A myriad of problems arise with getting adequate sample support. First, the range interval may not be covered to obtain enough sample support due to instantaneous bandwidth constraints [3]. Secondly, RMB rule makes a assumption that the clutter is independent and identically distributed (i.i.d) [7]. This assumption refers to the clutter having the sample distribution yet uncorrelated from one snapshot to snapshot. The homogeneous assumption also implies that all of the training data have the same covariance estimate $E\left[\hat{R}(\ell)\right] = \hat{R}$ [7]. Practically, this is not the case and the i.i.d assumption is quite often broken. From the earlier example, a littoral environment comprising of land and sea have two completely different statistically characteristics. Deleterious environmental effects such as ICM, clutter reflectively, clutter discretes, and/or weather cause the i.i.d. assumption to be broken. All these clutter heterogeneities lead to less accurate covariance estimation [3]. Additionally, processing effects such as a target within the training data of the covariance matrix

(causing self-cancellation), array mismatch, and aircraft crab further challenge accurate covariance estimation [8; 9; 10].

Multi-waveform space-time adaptive processing (μ-STAP) [8; 9; 10] addresses clutter heterogeneity by utilizing a multi-datacube formulation that causes a multiplicative increase in sample support and homogenized training sample to be more i.i.d. Multi-waveform STAP was introduced in two forms: multiple input, multiple output (MIMO) and single input, multiple output (SIMO). MIMO μ-STAP transmits from multiple array elements simultaneously and receives the illuminated scatterers from each waveform on the array elements. Pulse compression is applied to the receive data using their respective match filter. SIMO μ-STAP transmits only one waveform (similar to STAP) and pulse compresses the receive data with multiple pulse compression filters as if they were transmitted. SIMO μ-STAP can be is related to multiresolution STAP approaches [18; 19] that generate low-resolution GMTI data by using high-resolution SAR imaging [8; 9; 10]. In both MIMO and SIMO, multiple pulse compression datacubes are outputted. The primary waveform and match filter is the equivalent to a traditional STAP. Therefore, STAP is a single input, single output (SISO) approach and a subset of μ-STAP.

Consider K number secondary pulse compression filters. The SIMO μ-STAP pulse compression responses are similar to (2.5) is

$$\begin{aligned} z_{prime}(m,n,t) &= h_{prime}(t) * y(m,n,t) \\ z_{sec,1}(m,n,t) &= h_{sec,1}(t) * y(m,n,t) \\ &\vdots \\ z_{sec,K}(m,n,t) &= h_{sec,K}(t) * y(m,n,t) \end{aligned} \tag{3.12}$$

where $h_{prime}(t)$ the primary pulse compression filter and $h_{sec,k}(t)$ are the secondary pulse compression filters for $k = 1,2,\ldots,K$. The filter lengths are the same as the transmit waveform. The match filter defined in (2.5) is used for the primary pulse compression filter in the first equation in (3.12). The secondary filters are designed to have low cross-correlation with the primary. The new datacubes will have a homogenization of the range samples data due to the smearing caused by the

low-cross correlation filters. Examples of secondary filters include the reverse complex-conjugate of the match filter or complex-conjugate of the match filter.

The primary SCM after discretization and orientation into snapshots is

$$\hat{\mathbf{R}}_{prime}\left(\ell_{\mathrm{CUT}}\right)=\frac{1}{n\left(L_{prime}\right)}\sum_{\substack{\ell\in L\\ \ell\neq\ell_{\mathrm{CUT}}}}\mathbf{z}_{prime}\left(\ell\right)\mathbf{z}_{prime}^{H}\left(\ell\right) \tag{3.13}$$

where $L_{prime}\in L$. The cardinality of $n\left(L_{prime}\right)$ is taken since is no longer the number of snapshots in the set. The secondary SCM is

$$\hat{\mathbf{R}}_{\mu,NP}\left(\ell_{\mathrm{CUT}}\right)=\frac{1}{n(L_{sec})K}\sum_{k=1}^{K}\sum_{\ell\in L}\mathbf{z}_{sec,k}\left(\ell\right)\mathbf{z}_{sec,k}^{H}\left(\ell\right) \tag{3.14}$$

where NP denotes non-primary covariance matrix. When $K=1$, this is considered SISO μ-STAP. Note that the CUT is included in this estimation such that $L_{sec}>L_{prime}$. This is due to the homogenization of the clutter that μ-STAP causes. Leaving the CUT will spread large clutter discretes that may reside in the CUT. The μ-STAP SCM is a summation between the primary SCM and the non-primary SCM

$$\hat{\mathbf{R}}_{\mu}\left(\ell_{\mathrm{CUT}}\right)=\hat{\mathbf{R}}_{prime}\left(\ell_{\mathrm{CUT}}\right)+\hat{\mathbf{R}}_{\mu,NP}\left(\ell_{\mathrm{CUT}}\right) \tag{3.15}$$

The estimated space-time weight vector to maximize SINR is

$$\hat{\mathbf{w}}\left(\omega,\theta,\ell_{CUT}\right)=\hat{\mathbf{R}}_{i}^{-1}\left(\ell_{CUT}\right)\mathbf{c}_{st}\left(\omega,\theta\right) \tag{3.16}$$

where $\hat{\mathbf{R}}_{i}\left(\ell_{CUT}\right)$ is replaced with the either the estimate for the primary (STAP) SCM, non-primary SCM, or μ-STAP SCM with the potential for each to be diagonally loaded. Diagonal loading is employed to ensure the covariance matrix is full rank.

$$\hat{\mathbf{w}}\left(\omega,\theta,\ell_{CUT}\right)=\left(\hat{\mathbf{R}}_{i}\left(\ell_{CUT}\right)+\sigma_{v}^{2}\mathbf{I}\right)^{-1}\mathbf{c}_{st}\left(\omega,\theta\right) \tag{3.17}$$

where σ_{v}^{2} is the receiver noise power. The adaptive filter (weight vector) is applied to pulse com-

pressed data to form the test statistic

$$\hat{\alpha}\left(\theta,\omega,\ell_{CUT}\right)=\hat{\mathbf{w}}^{H}\left(\ell_{CUT},\theta,\omega\right)\mathbf{z}\left(\ell_{CUT}\right) \tag{3.18}$$

Multi-waveform STAP was found to benefit the covariance estimation in the presence of clutter heterogeneity. μ-STAP has shown to be effective in the estimation of the SCM because the number of independent sample data is increased by a factor of K. Under low sample support and/or presence of heterogeneous data, μ-STAP provides enhances detection performance over STAP [8; 9; 10]. However, STAP and μ-STAP both have high computational cost associated with it due to the estimation and inversion of a covariance matrix on every range sample. Partially adaptive techniques for STAP have been examined extensive [3]. In Chapter 5, these algorithms are applied to new form of μ-STAP presented in Chapter 4.

Chapter 4

Post Pulse Compression Multi-Waveform Space-Time Adaptive Processing

Implementation of μ-STAP in legacy radars is challenging due to the modifications needed. Most of these radars implements pulse compression prior to analog-to-digital conversion. The original SIMO μ-STAP formulation utilizes a pre-pulse compressed space-time datacube to generate multiple pulse compressed datacubes through multiple pulse compression filters. Therefore, an alternative SIMO μ-STAP to generate multiple homogenized datacubes *post pulse compression* is introduced. Post multi-waveform space-time adaptive processing (Pμ-STAP) uses a single pulse compression datacube then applies multiple *homogenization filters* to generate multiple datacubes for covariance estimation. The objective of SIMO Pμ-STAP is to induce a smearing and homogenization of the space-time samples to SIMO μ-STAP. The generation of the homogenized pulse compressed data is similar to the pulse compression stage in (3.12)

$$\begin{aligned} q_{\text{prime}}(m,n,t) &= g_{\text{prime}}(t) * z_{\text{prime}}(m,n,t) \\ q_{\text{sec},1}(m,n,t) &= g_{\text{sec},1}(t) * z_{\text{prime}}(m,n,t) \\ &\vdots \\ q_{\text{sec},k}(m,n,t) &= g_{\text{sec},1}(t) * z_{\text{prime}}(m,n,t) \end{aligned} \tag{4.1}$$

where g_{prime} is the primary homogenization filter and $g_{sec,k}$ are the kth secondary homogenization filters for $k = 1,2,\ldots,K$. The primary filter is a time-delayed impulse designed to align the fast-time snapshots appropriately with secondary filters while the initial pulse compression response is unaffected. Secondary filters have a uniform amplitude and a stochastic phase. For a filter length

T, primary and secondary filters respectively are

$$\begin{aligned} g_{prime}(t) &= \delta\left(t - \frac{T}{2}\right) \\ g_{sec,k}(t) &= \frac{1}{\sqrt{T}} e^{j2\pi\theta_k(t)} \end{aligned} \tag{4.2}$$

where $\delta(\bullet)$ is the Dirac delta function and $0 \leq t \leq T$. The phase of the secondary filters have a uniform distribution $\theta_k(t) \sim U(-0.5, 0.5)$ for $k = 1, 2, \ldots, K$.

The primary, non-primary, and Pμ-STAP SCMs are estimated in a similar manner to (3.13-3.15)

$$\hat{\mathbf{R}}_{P\mu,prime}(\ell_{CUT}) = \frac{1}{n(L_{prime})} \sum_{\substack{\ell \in L_{prime} \\ \ell \neq \ell_{CUT}}} \mathbf{q}_{prime}(\ell)\, \mathbf{q}_{prime}^{H}(\ell) \tag{4.3}$$

$$\hat{\mathbf{R}}_{P\mu,NP}(\ell_{CUT}) = \frac{1}{n(L_{\text{sec}})K} \sum_{k=1}^{K} \sum_{\ell \in L_{prime}} \mathbf{q}_{sec,k}(\ell)\, \mathbf{q}_{sec,k}^{H}(\ell) \tag{4.4}$$

$$\hat{\mathbf{R}}_{P\mu}(\ell_{\text{CUT}}) = \hat{\mathbf{R}}_{P\mu,prime}(\ell_{\text{CUT}}) + \hat{\mathbf{R}}_{P\mu,NP}(\ell_{\text{CUT}}). \tag{4.5}$$

The Pμ-STAP filter is generated similar to (3.17). The adaptive Pμ-STAP SINR is developed from (3.5).

A common characteristics Pμ-STAP has with μ-STAP is the ability to vary the number of secondary filters. Unlike μ-STAP, a key attribute is the ability to also vary secondary filter length regardless of the transmit waveform. In the following subsections, in-depth analysis of homogenization filters new characteristics are examined. After, Pμ-STAP performance is compared with STAP and μ-STAP in heterogeneous high-fidelity simulated datasets

4.1 Homogenization Filter Length

The pulse compression stage in Pμ-STAP sets non-smeared, SNR-maximized mainlobe and sidelobe responses in the autocorrelation. The homogenization filter decorrelates (similar to the low-cross correlation filters in Chapter 3) to smear the mainlobe response. In μ-STAP, application

of secondary pulse compression filters sets the smeared mainlobe and sidelobe responses. Consequently, secondary pulse compression filters must be optimized based on the primary waveform. If the secondary filters are not designed to have low-cross correlation with the transmit waveform, homogenization does not occur. Fortunately, for GMTI the transmit waveform is known a priori and generation of these secondary filters is fairly simple.

The amount of decorrelation is dependent on the length of the homogenization filters. This allows more flexibility in their design. The filter length dictates the amount of power reduction and extent of mainlobe and sidelobe responses. To see this effect, a LFM waveform with a time-bandwidth product of $B\tau = 100$ is match filtered then homogenized with different filter lengths. In the following figures, filter lengths of $BT = 5, \frac{B\tau}{2}, B\tau, 2B\tau$ corresponding to $BT = 5, 50, 100, 200$ are examined. In order to have even order linear FIR filters, some lengths were adjusted to $BT = 5, \frac{B\tau}{2} - 1, B\tau - 1, 2B\tau - 1$ corresponding to $BT = 5, 49, 99, 199$. The primary homogenization filter response is presented in black and the secondary filter is presented in red.

Consider filter length of $BT = 5$ presented in Figure 4.1. The primary filter response has mainlobe and sidelobe response typical of a LFM with the first sidelobe being 13dB down of the mainlobe. The decorrelation is obvious. The mainlobe decrease by -10dB. The sidelobes also decreases. Mainlobe smearing is at a minimum. Even a small filter will cause significant loss.

Next, a filter length of $BT = B\tau/2 - 1$ is depicted in Fig. 4.2. The mainlobe smearing is more evident than in the previous figure. Note, based on filter the dynamic range of the mainlobe smearing can drop -40dB. For this filter length, the range is primarily localized between -15 and -30db. Also spurious responses occur in the secondary response sidelobes. However, due to the aggregation in the covariance, these will be averaged out. Now consider $BT = B\tau - 1$ in Fig. 4.3. The mainlobe smearing increases. Also, the maximum power decreases by -3dB with a increased dynamic range. The mainlobe extends to half of the sidelobes in the primary response. Finally, consider the final length of $BT = 2B\tau - 1$ in Fig. 4.4. As a result, the mainlobe smearing will span the entire extent of the match filter response.

In summary, secondary mainlobe smearing and power reduction is proportional to the length

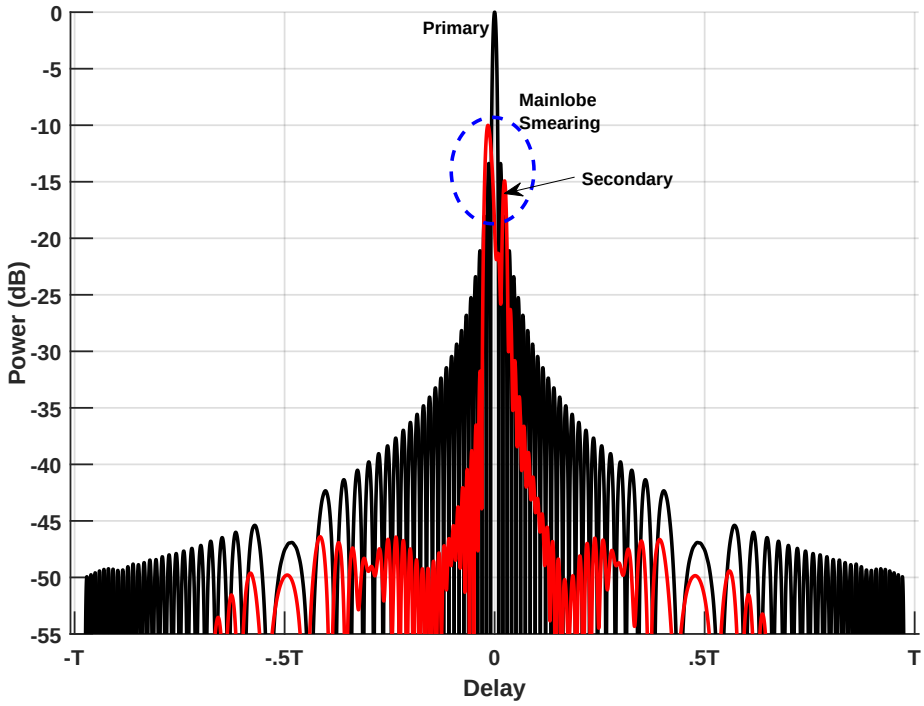

Figure 4.1: Primary and Secondary Homogenization Response for $BT = 5$

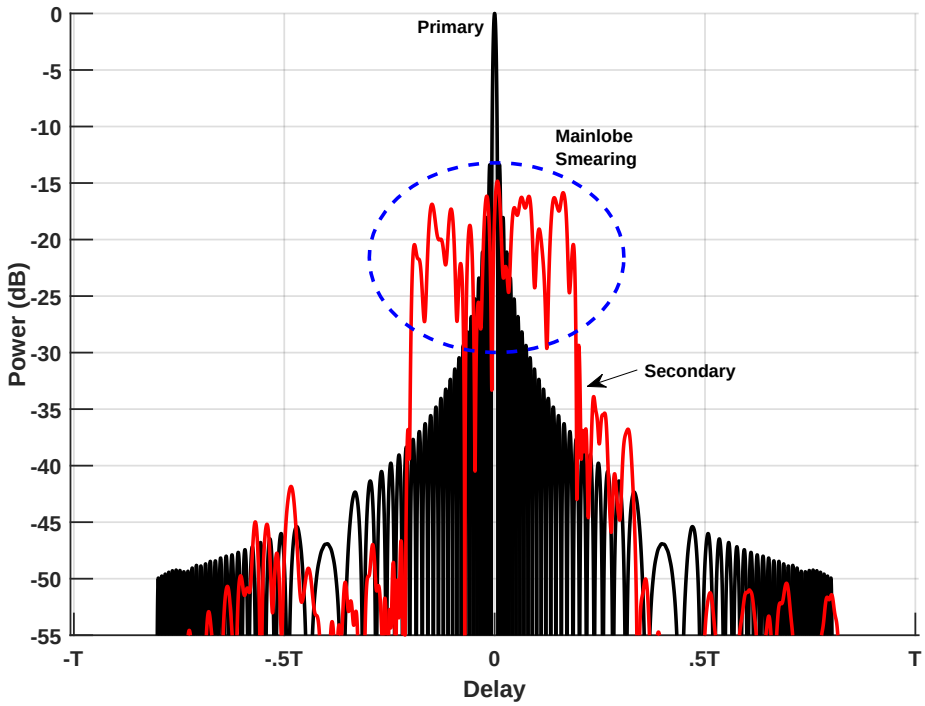

Figure 4.2: Primary and Secondary Homogenization Response for $BT = B\tau/2 - 1$

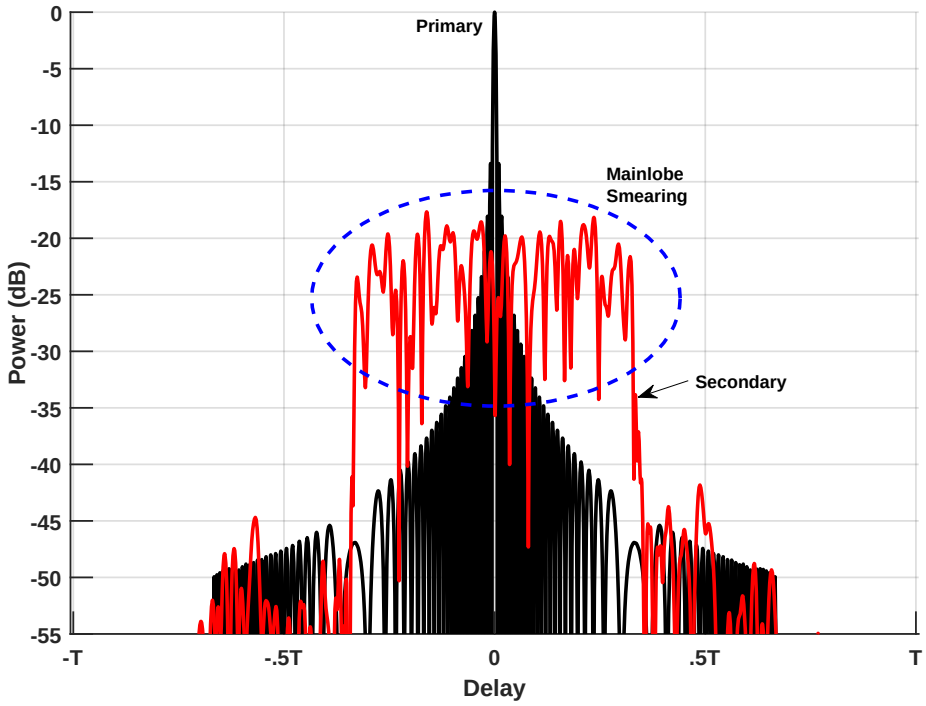

Figure 4.3: Primary and Secondary Homogenization Response for $BT = B\tau - 1$

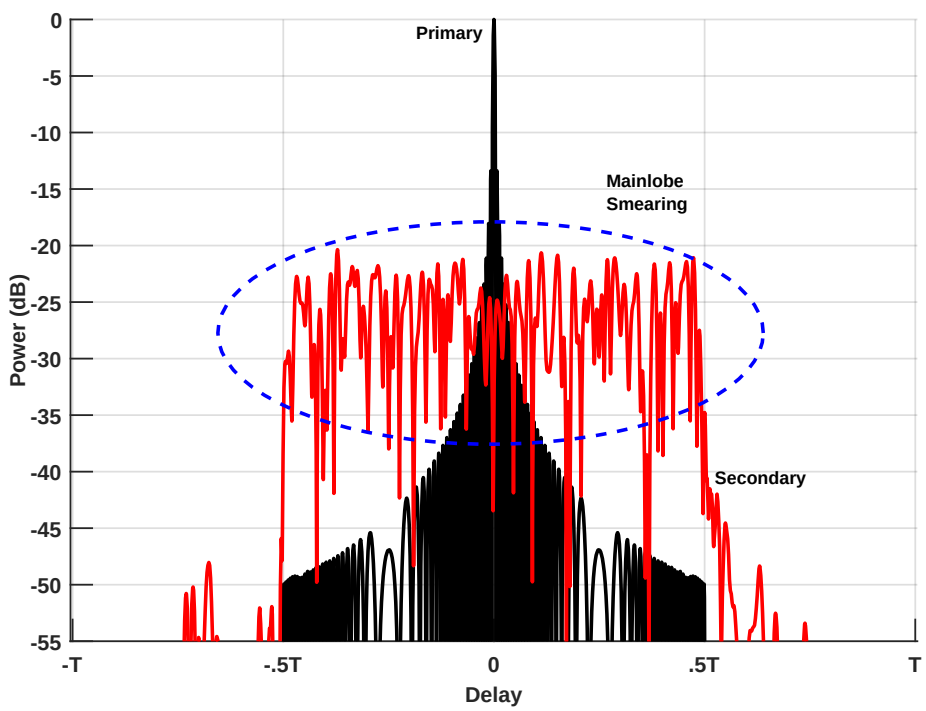

Figure 4.4: Primary and Secondary Homogenization Response for $BT = 2B\tau - 1$

of the homogenization filter. The width of the smearing is equal to the length of the filter. In order for the secondary filter mainlobe response to span the entire primary filter response (mainlobe and sidelobes), the filter length needs to be $BT = 2B\tau - 1$. Interestingly, this is equivalent to the size of the linear convolution (autocorrelation) between the transmit waveform and match filter. In addition to mainlobe smearing, sidelobes of the receive data will expend further out. This will expand the length of the secondary datacube as well. Increasing the number samples possible for covariance estimation.

To understand the benefit of different filter lengths have on covariance estimation, an SINR loss analysis was performed using Monte Carlo simulation. A airborne radar traveling at an interelement spacing of $\beta = 1$ is illuminating a scene with a LFM waveform from a for a $N = 5$ element ULA and processing $M = 21$ pulses in a CPI. A heterogeneous clutter scene is examined. First, homogeneous clutter is generated similar to [8; 9; 10] by dividing the azimuthal range ring into 246 equal-size angle clutter patches. The scattering from each patch is i.i.d. complex Gaussian. The additive noise is similarly modeled as Gaussian noise. The clutter-to-noise ratio (CNR) is approximately 54dB. Heterogeneous clutter is generated by randomly modulating the power of complex Gaussian homogeneous clutter patches for each range and angle clutter patch using a Weibull distribution with a shape parameter of 1.7 [20; 21]. The additional magnitude modulation is randomly distributed from [0, 30] dB. A uniformly distributed ICM is introduced across $\pm 2\%$ of the normalized Doppler response [8; 9; 10]. A total of 50 Monte Carlo trials were implemented.

Using (4.3-4.5), covariance estimation was performed using homogenized pulse compressed data generated for filter lengths of $BT = B\tau/2 - 1, B\tau - 1, 2B\tau - 1$. Four homogenization filters were implemented. In [8; 9; 10], an extensive analysis of the number of secondary filters to enhance covariance estimation was examined. It was shown that having four secondary pulse compression filters for received processing provides the best performance. Based on the similarities of μ-STAP and Pμ-STAP, it can be expected that the same amount of filters would be necessary. In the succeeding subsection, this notion is confirmed in a less extensive analysis. In Figure 4.5, SINR loss from the optimal covariance matrix is compared between STAP and Pμ-STAP. The amount

Table 4.1: Simulated Test Flight 1 Parameters

linear FM waveform, $B\tau = 100$
N=5 elements in ULA
M=21 pulses in CPI
$\beta = 1$ interelement spacing in one PRI

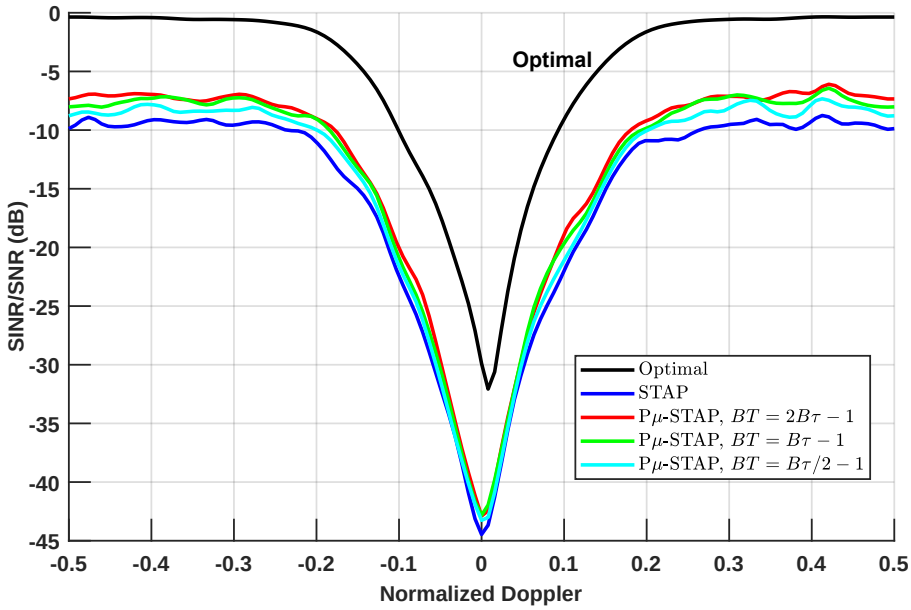

Figure 4.5: SINR Loss for Various Homogenization Filter Lengths

of training samples satisfies RMB rule. As filter length increases, SINR increases and minimum detectable velocities decreases. In all instances, Pμ-STAP SINR and MDV performance is greater than STAP. The main contributor to the benefit is the increase in sample support. Recall Pμ-STAP sample support is a factor of K greater than STAP by virtue of the additional datacubes. Thus, STAP has $2MN - 3$ in contrast to $2KMN - 3K$ for $P\mu$-STAP. The average improvement factor ratio between SINR and optimal SINR is examined in Figure 4.6. Note that two range samples is the minimum (one sample on each side of CUT).

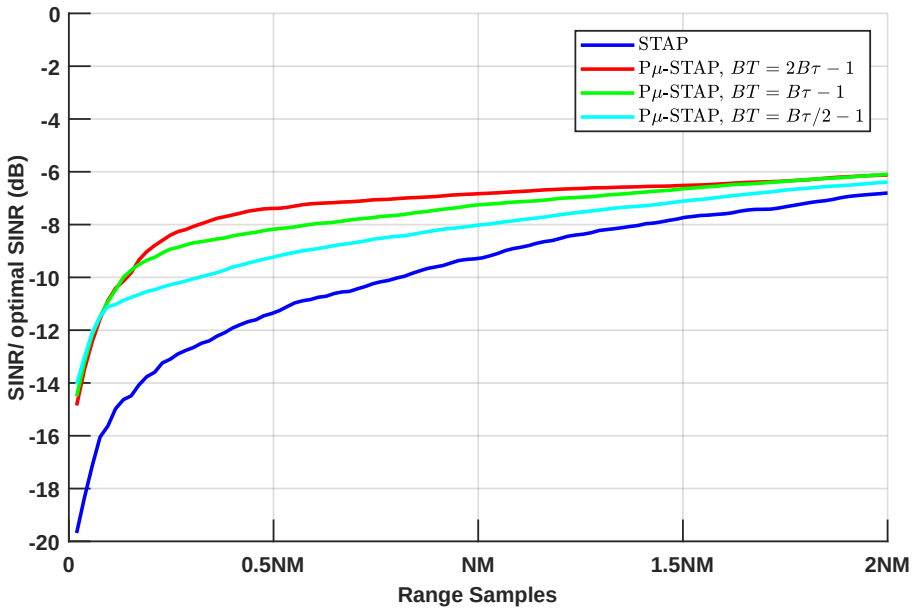

Figure 4.6: Average Improvement Factor for Various Homogenization Filter Lengths

For very low amounts of range samples in the covariance, Pμ-STAP AIF for all different filter lengths are about the same. At 0.5MN (1/4 of the RMB rule), the performance benefit of different homogenization lengths is seen. The highest length of $BT = 2B\tau - 1$ is 2dB greater than $BT = B\tau/2 - 1$ and 4dB greater than STAP. For all filter lengths, Pμ-STAP outperforms STAP. As more samples are added to the training data, STAP performance begins to increase. Henceforth, we will consider the homogenization length to be $BT = 2B\tau - 1$.

4.2 Number of Secondary Filters

A analysis is performed for the number of homogenization filters to affirm the results in [8; 9; 10]. Recall that the number of secondary filters, K, provides a multiplicative increases the number of training samples. The additional data is not independent. Therefore, simply adding additional filters will not satisfy the RMB rule. Furthermore, [8; 9; 10] showed a that four secondary filters is adequate. Any additional filters would provide very minimal improve. Using the simulated test parameters from Table 4.1, SINR loss and AIF are implemented with STAP and Pμ-STAP in homogeneous and heterogeneous clutter previously described in the last section. A Monte Carlo

Table 4.2: Training Data Combinations in SINR Analysis of Number Secondary Filters

Training Data	**Line style/color**
primary	solid blue
primary, secondary $K = 1$	solid green
primary, secondary $K = 2$	solid red
primary, secondary $K = 3$	solid teal
primary, secondary $K = 4$	solid purple
secondary $K = 1$	dotted green
secondary $K = 2$	dotted red
secondary $K = 3$	dotted teal
secondary $K = 4$	dotted purple

simulation of 50 trials was performed.

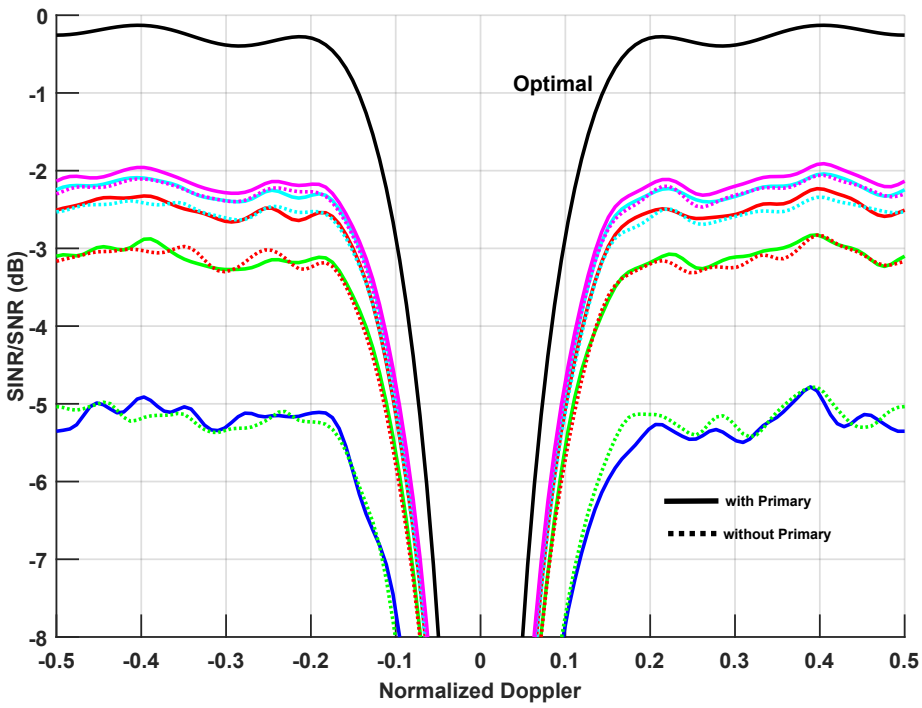

Figure 4.7: SINR Loss at $0.5MN$ for Various Number of Secondary Filters in Homogeneous Clutter

First, SINR with low-sample support in homogeneous clutter is considered since this will be the primary regime in heterogeneous clutter. Low sample support will be considered as one-fourth of the RMB rule, i.e. $n(L) = 2MN/4 = 0.5MN$. Additionally, SISO Pμ-STAP (secondary covariance matrices only) (3.14) is presented to provide a one-to-one comparison to SISO STAP. Table 4.2

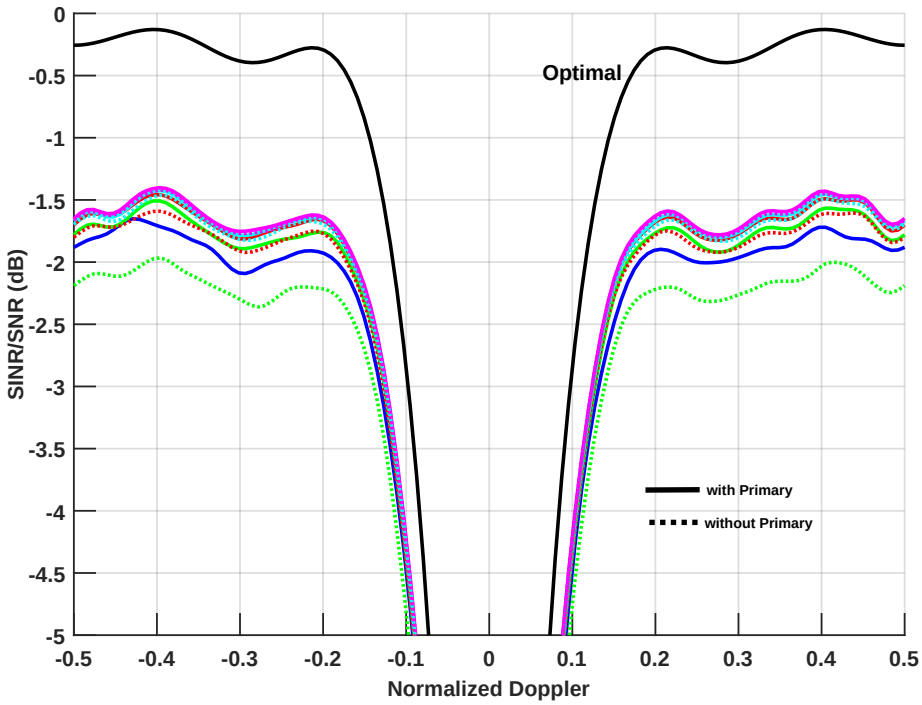

Figure 4.8: SINR Loss at $2MN$ for Various Number of Secondary Filters in Homogeneous Clutter

describes the different training data combinations used in the SINR analysis.

In Figure 4.7, SISO Pμ-STAP response is one par with STAP response with some subtle variability with SINR. As the number of secondary filters increase, with or without the primary, the SISO Pμ-STAP SINR boosts by 2dB-3dB. Interestingly, using primary with $K = k$ secondary filters Pμ-STAP has similar response to using no primary with secondary $K = k+1$ Pμ-STAP. Therefore, if the primary homogenization response is not used, simply adding an additional secondary response will provide similar SINR. The minimum detectable velocity also benefits from the addition secondary filter responses. At $\eta = -8db$ SINR loss, MDD increases from $\omega_{min,prime}(\eta = -8dB) = -0.10$ to $\omega_{min,P\mu}(\eta = -8dB) = -0.07$, a 30% increase. Next, SINR loss is presented at $n(L) = 2MN$ range samples. Analysis of homogeneous clutter allows for a fair comparison of STAP when enough training samples are available to satisfy the RMB rule. In Figure 4.8, unlike low sample support, a SISO Pμ-STAP does not provide the same benefits. The increase sample support provides a boost to the STAP performance. However, even at $2MN$ SIMO Pμ-STAP provides an SINR benefit. The minimum detectable velocities are fairly similar for the different filter

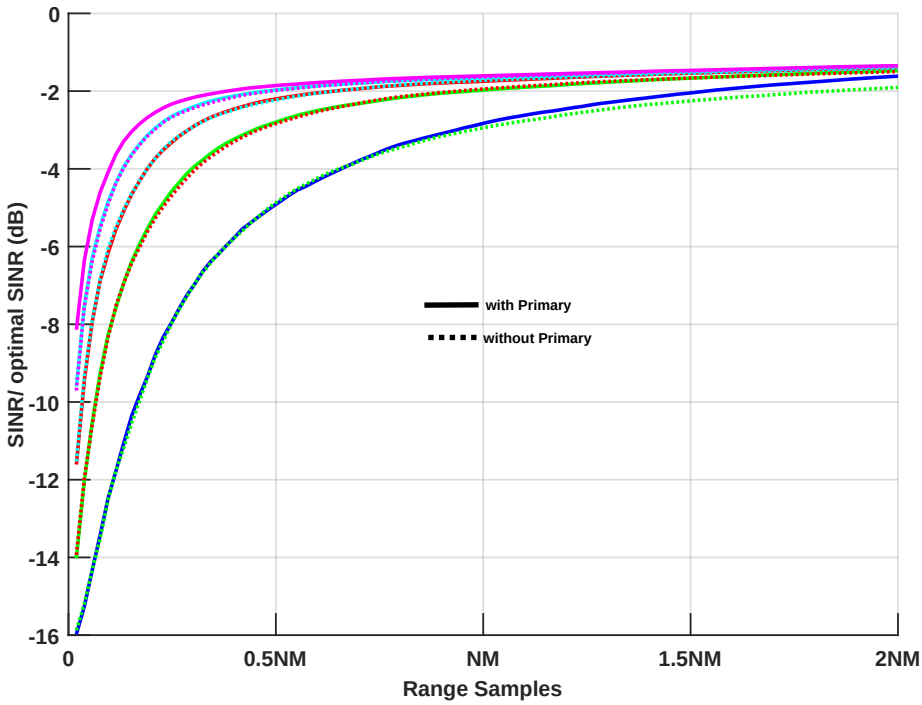

Figure 4.9: Average Improvement Factor for Various Number of Secondary Filters in Homogeneous Clutter

combinations. Finally, average improvement factor is presented for the filter combinations in Figure 4.9. The AIF benefit at $0.5MN$ and $2MN$ from SINR in Figs. 4.7-4.8 are seen. As the sample support of the covariance estimation decreases, STAP performance decreases at a greater rate than SIMO Pμ-STAP. Each combination shows a asymptotic bound on performance. As the number of secondary filters increases, the number of ranges samples in the training data Pμ-STAP needs to reach this bound decreases. Again, SISO Pμ-STAP provides the same performance as STAP.

The different filter combinations in heterogeneous clutter will now be presented. In Figures 4.10-4.11, SINR Loss is shown at $n(L) = 0.5MN$ and $n(L) = 2MN$, respectively. The affect heterogeneous clutter has on SINR performance is clear. In Fig. 4.10, the maximum SINR loss of the different combinations is $\eta = -7.0dB$ compared to $\eta = -1.4dB$ in homogeneous clutter. The performance benefit of Pμ-STAP over STAP is still the same. A 2-3dB improvement is still observed and MDD increases. Fig 4.11 shows that SISO Pμ-STAP has a greater SINR loss than STAP and SIMO Pμ-STAP provides a marginal increase in SINR. In Fig 4.12, AIF is presented. In com-

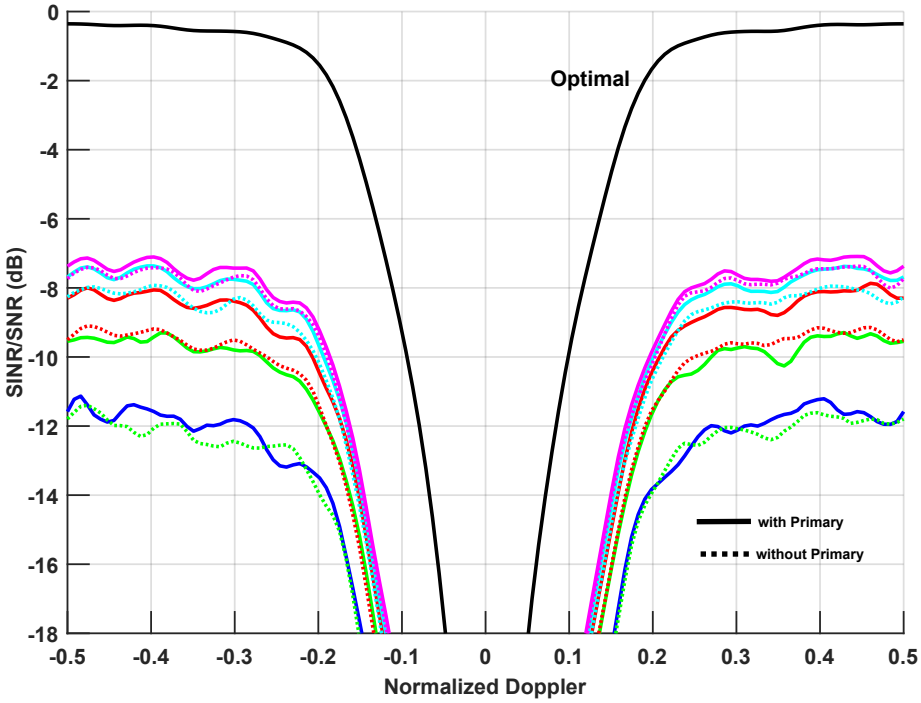

Figure 4.10: SINR Loss at $0.5MN$ for Various Number of Secondary Filters in Heterogeneous Clutter

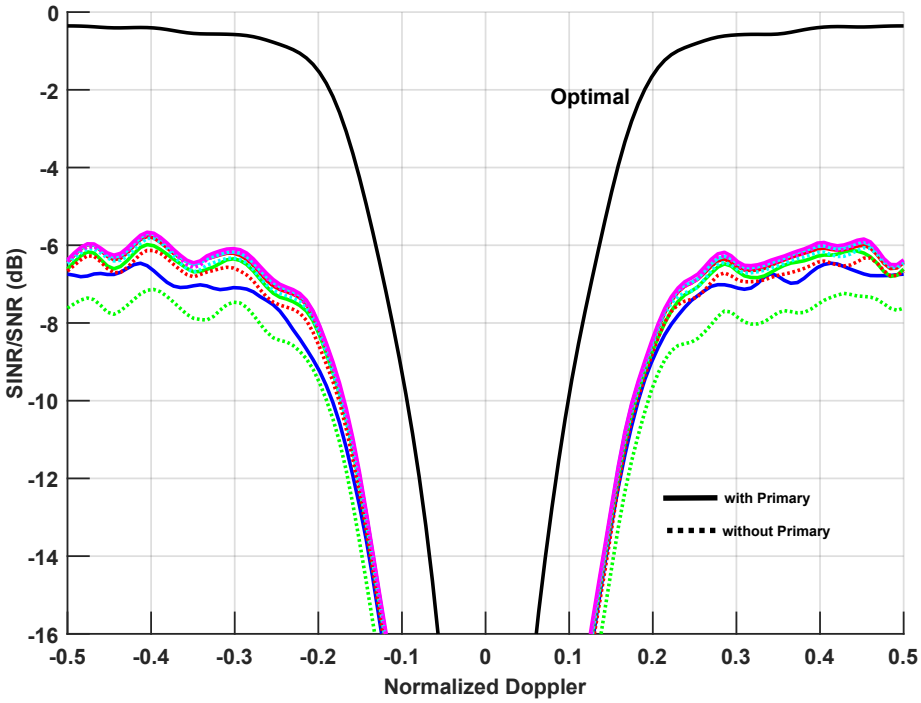

Figure 4.11: SINR Loss at $2MN$ for Various Number of Secondary Filters in Heterogeneous Clutter

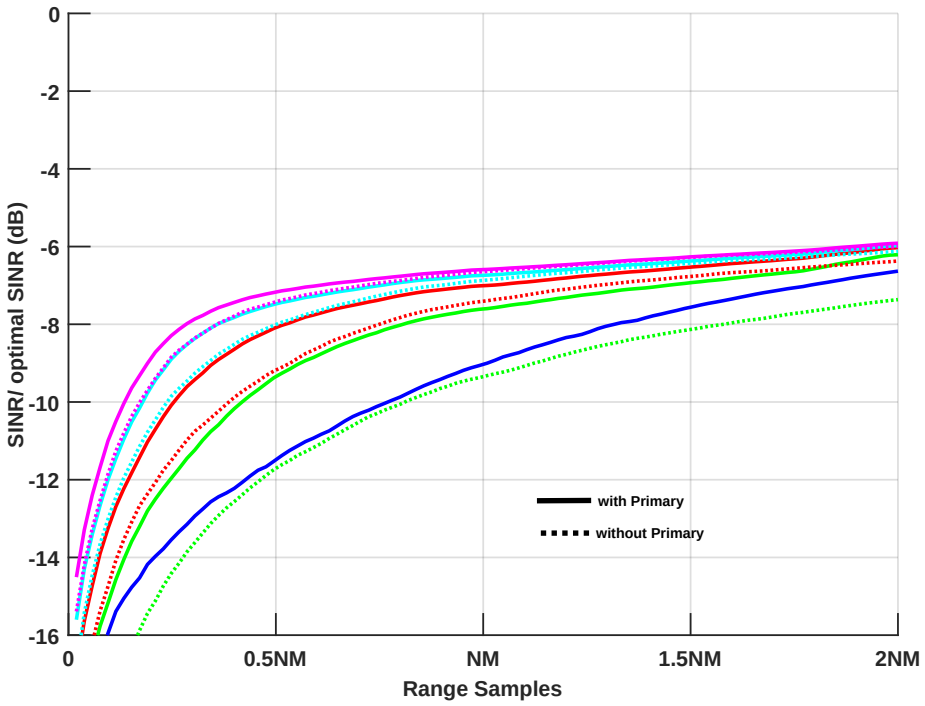

Figure 4.12: Average Improvement Factor per Range Sample Intervals for Various Number of Secondary Filters in Heterogeneous Clutter

parison to homogeneous (Fig. 4.9), there is a -4dB or more decrease in AIF for all combinations. SISO Pμ-STAP is no longer robust enough to contend with STAP. Otherwise, the performance improvement trends are the same. SIMO Pμ-STAP AIF increases with the number of secondary filters and needs less samples to do it.

In summary, Pμ-STAP provides greater minimal detectable velocity, less SINR loss, and greater improvement factor with less samples in the training data than STAP. This was presented in low and high sample support regimes in homogeneous and heterogeneous clutter. Similar to [8; 9; 10], four secondary filters were shown to have the best benefit in performance. Henceforth, all Pμ-STAP results will contain four secondary filters unless otherwise specified.

4.3 μ-STAP and Pμ-STAP Performance Comparison

Now that the basic characteristics of the homogenization filters in SIMO Pμ-STAP has been concluded. A comparison to its counterpart, SIMO μ-STAP, can now be conducted. In this section,

an SINR analysis of these algorithms are compared in heterogeneous clutter. A description of the heterogeneous clutter generation was provided in section 4.1. In addition, two rigorous forms of clutter heterogeneity is presented: clutter discrete in the CUT and targets in the training samples [8; 9; 10]. A clutter discrete is a stationary scatterer that has a high power return. A clutter discrete localized in a single range cell without similar clutter in training data will not be characterized by the SCM. Therefore, the clutter discrete in a CUT will not be nullified [8; 9; 10; 22]. Targets in training samples that have similar scatterer characteristics as a potential target in the CUT will cause self-cancellation. In [8; 9; 10], μ-STAP was shown to provide a substantial benefit in SINR and worst-case improvement factor over STAP in these heterogeneous scenarios. Here, Pμ-STAP will provide a similar analysis to determine if it is also robust under similar circumstances. For completeness, SISO forms of STAP, μ-STAP, and Pμ-STAP is also presented.

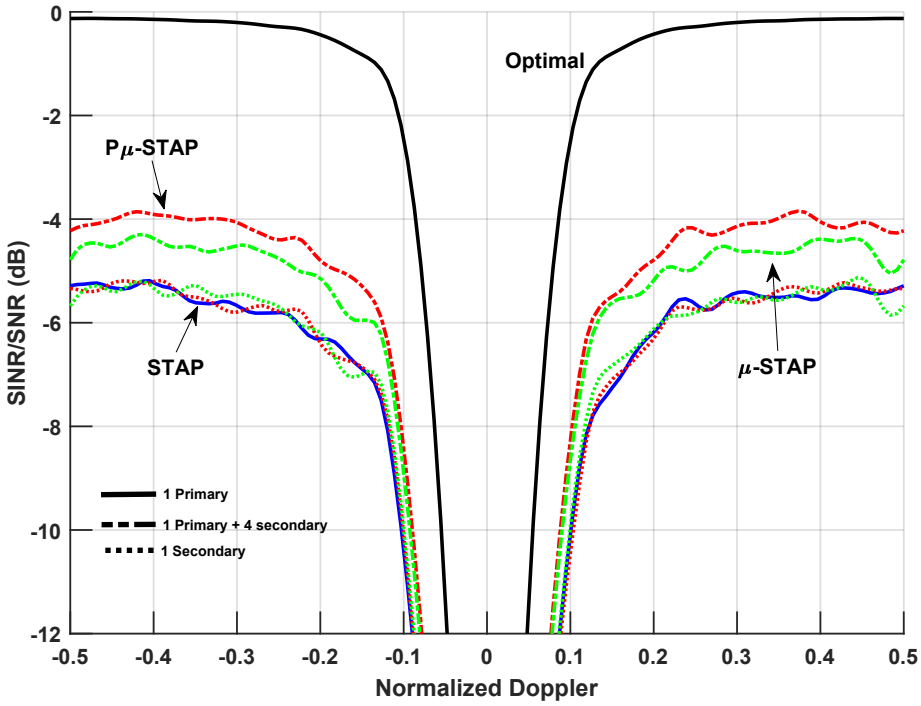

Figure 4.13: μ-STAP and Pμ-STAP SINR Loss at $0.5MN$ in Heterogeneous Clutter

This analysis begins with examining these algorithms in heterogeneous clutter. In Figure 4.13, SINR loss in the low sample support regime is presented. Table 4.3 shows the different algorithms

and their corresponding line style and color. All SISO algorithms have similar SINR. Interestingly, SIMO Pμ-STAP has better SINR performance than SIMO μ-STAP. This may due to several different things. One being the relationship between the number of samples in the training data and homogenization filter length since Pμ-STAP secondary filter lengths can be increases beyond the μ-STAP filter length. Another option may be that applying homogenization after pulse compression preserved some fidelity allowing for more robustness. More research need to be conducted to examine this further. For the purposes of this analysis, the importance is that Pμ-STAP has equal or greater performance than μ-STAP. Fig. 4.14 shows the AIF. At full support, μ-STAP has a better improvement factor than Pμ-STAP. Also, STAP is overall better than SISO μ-STAP and SISO Pμ-STAP algorithms.

The analysis continues with a high power 20dB clutter discrete in the CUT within a heterogeneous scene shown in Figure 4.15. The degradation of clutter discrete causes a overall decrease in SINR loss and imbalance in SINR across detectable Doppler frequencies varying a couple decibels. At low sample support, Pμ-STAP again outperforms μ-STAP. But, there is no improvement in minimum detectable velocity. SISO μ-STAP and SISO μ-STAP are more robust to the clutter discrete than STAP. This is further seen in the AIF in Fig. 4.16. STAP initially has better AIF but the other SISO algorithms rapidly increase with increasing sample support.

Finally, targets in the training data is examined. In Figure 4.19, ten targets were placed in training samples (5 one each side of CUT after guard cells) in a heterogeneous clutter. The target power of each was 15dB SNR. The impact of self-cancellation is seen at $\omega = 0.49$. SISO and SIMO Pμ-STAP is more robust to the clutter discrete with the former having the edge. All other algorithms

Table 4.3: Training Data Combinations in Performance Comparison

Algorithm	**Line style/color**
STAP	solid blue
SISO μ-STAP	dotted green
SISO Pμ-STAP	dotted red
SIMO μ-STAP	dashed green
SIMO Pμ-STAP	dashed red

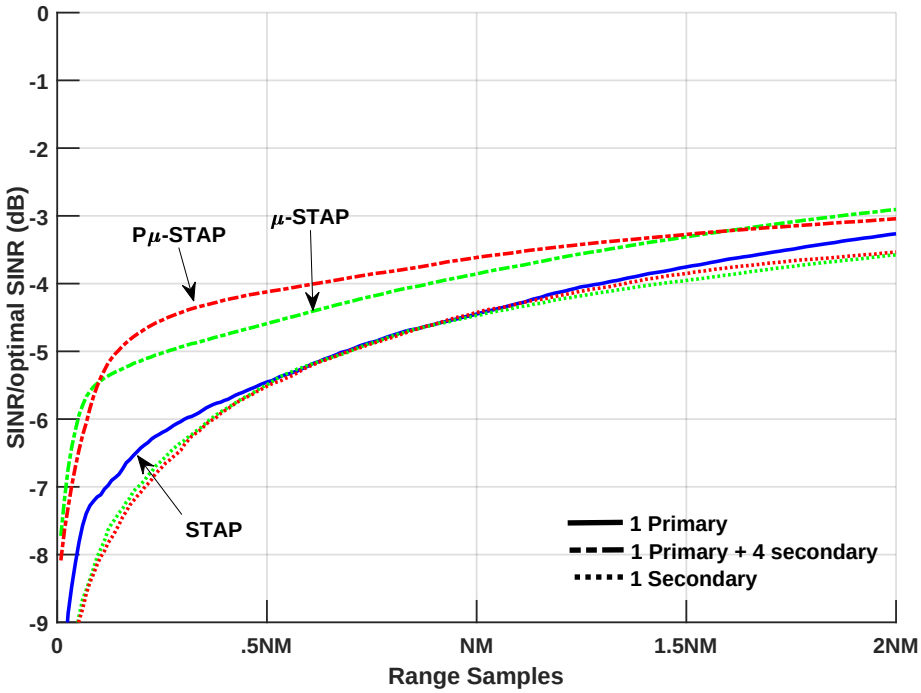

Figure 4.14: μ-STAP and Pμ-STAP Average Improvement Factor in Heterogeneous Clutter

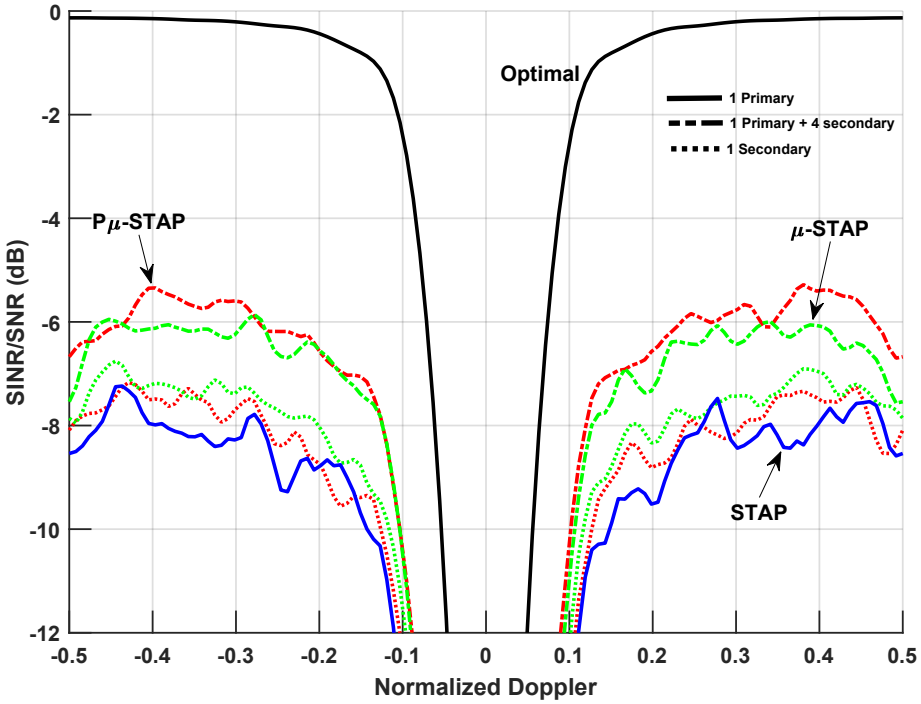

Figure 4.15: μ-STAP and Pμ-STAP SINR Loss at $0.5MN$ with Clutter Discrete in CUT

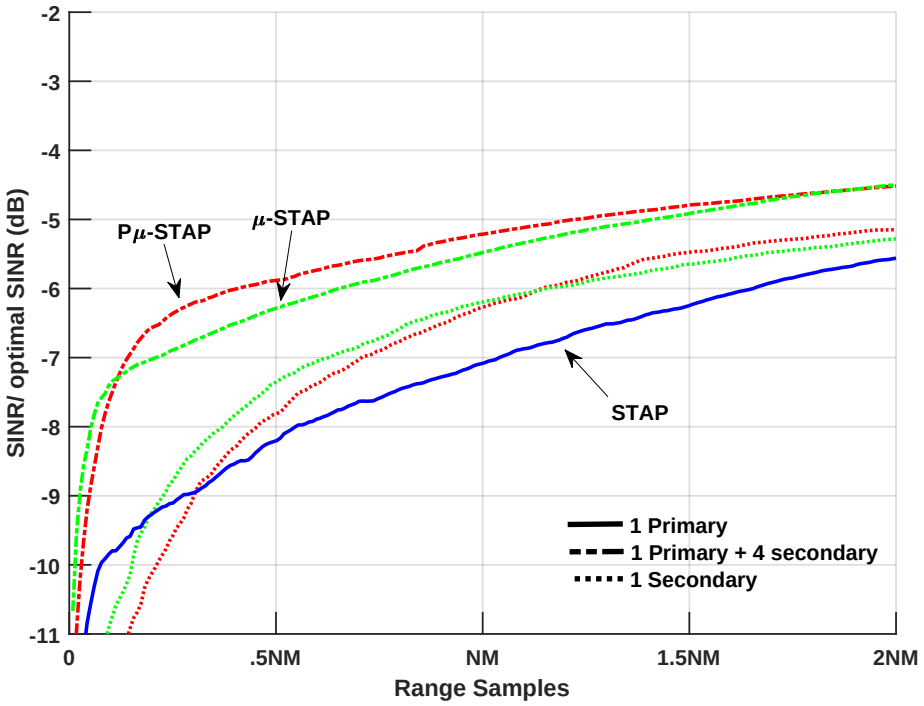

Figure 4.16: μ-STAP and Pμ-STAP Average Improvement Factor with Clutter Discrete in CUT

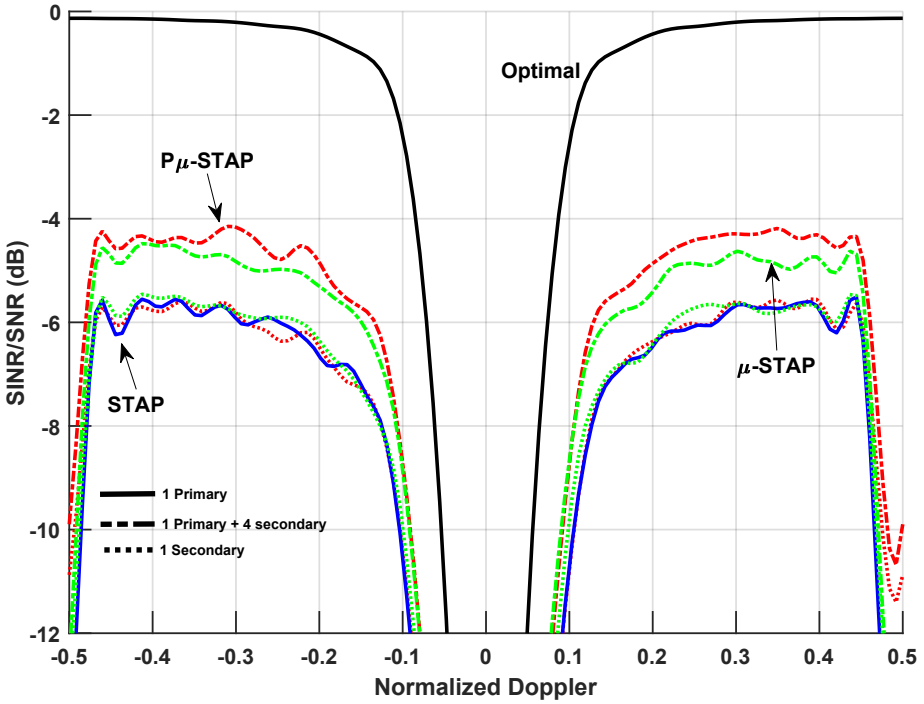

Figure 4.17: μ-STAP and Pμ-STAP SINR Loss at $0.5MN$ with Targets in Training Data

under performed. The AIF was also examined. The results were similar to heterogeneous clutter without self-cancellation (Fig. 4.14). Since the effect of self-cancellation is best seen in SINR, it is not pertinent to present.

To summarize, in the presence of clutter discrete and self-cancellation, SISO μ-STAP and SISO Pμ-STAP provide a improvement in performance over SISO STAP. However, for a simple heterogeneous scene SISO STAP outperforms them. Incorporating additional secondary filters to the family of μ-STAP algorithms will provide a improvement in detection performance. Overall, Pμ-STAP has similar or greater performance than μ-STAP. Whether it be pre- or post-pulse compression, smearing for identically distributed data and multiple datacubes will provide a performance benefits over STAP.

4.4 Pμ-STAP in High Fidelity Knowledge Aided Radar Architecture

Up to this point, analyses were performed on control simulated datasets that provided a great baseline to the behavior of Pμ-STAP in heterogeneous clutter. A primary attribute of Pμ-STAP is its ability to be performed on pulse compressed data without the necessity a priori knowledge of the transmit waveform. As a true test of performance, Pμ-STAP was examined in a simulated, high-fidelity Knowledge Aided Sensor Signal Processing and Expert Reasoning (KASSPER) dataset developed as a challenge by Defense Advanced Research Projects Agency (DARPA) in 2002 [23]. KASSPER using knowledge aided adaptive radar architecture that incorporates environmental clutter knowledge that operational radars encounter [24]. In KASSPER, the airborne platform is traveling at $100m/s$. A 8×11 UPA is vertically beamformed to $N = 11$ elements spaced at $d = 10.9cm$. At a PRF of $f_r = 1284$, $M = 32$ pulses are collected in a CPI. Therefore, low sample support will be $0.5MN = 88$ and full sample support is $2MN = 352$. The interelement spacing traveled in one PRI is $\beta = 0.923$. The dataset spans 35-50 km for 1000 range samples.

SINR Loss at low sample support for KASSPER range CUTs 26, 236, and 400 are presented. Each provide different deleterious effects to the STAP filter. STAP and Pμ-STAP are presented in blue and red, respectively. In Figure 4.18, similar SINR response to a clutter dis-

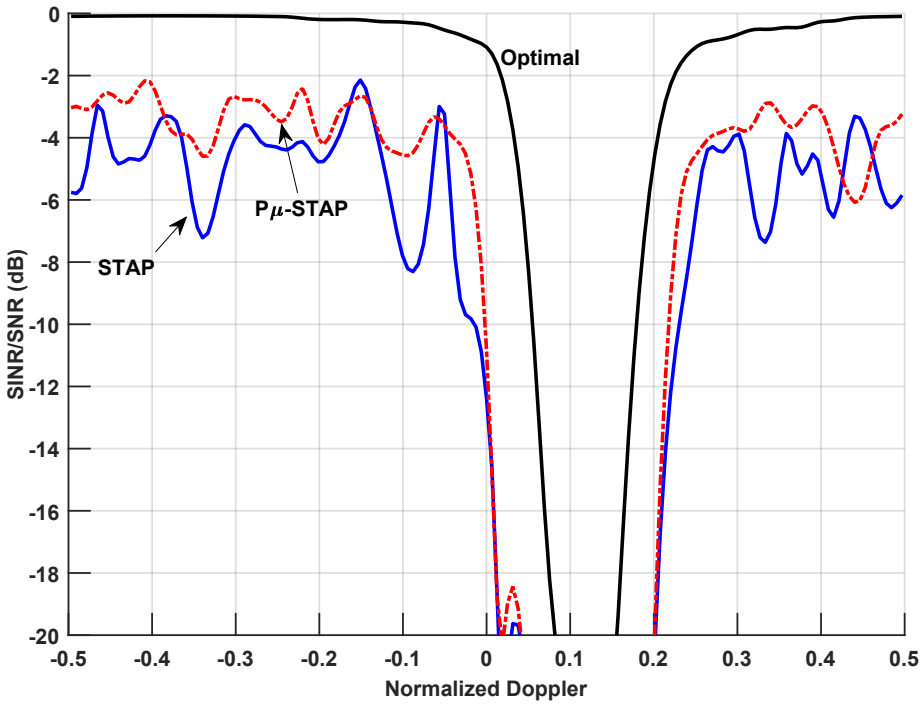

Figure 4.18: SINR Loss in KASSPER Range Sample 27

crete in the CUT is seen. In detectable Doppler frequencies where STAP has a large SINR loss ($\omega = -0.32. - 0.09, 0.32$), P$\mu$-STAP provides the expected improvement in SINR. In addition, Pμ-STAP increases the MDD. Although there is an improvement, this is a strong contrast to the previous results (4.15). In the control results, Pμ-STAP was 2-3dB in improvement and STAP never performed better than Pμ-STAP at any Doppler frequencies. Here, STAP outperforms at $\omega = .25, .45$.

This benefit over Pμ-STAP is further seen in the AIF in Fig. 4.19. In the lower sample support regimes, Pμ-STAP is greater STAP. As $n(L)$ increases, STAP performance suppresses Pμ-STAP. Also, Pμ-STAP shows a dip in performance as number of samples increases. The improvement factor shows $AIF_{P\mu}(MN) < AIF_{P\mu}(0.5MN)$. In all previous results, as the number of samples increased so did AIF such that $AIF_{P\mu}(MN) > AIF_{P\mu}(0.5MN)$. Therefore, P$\mu$-STAP shows its benefit may be scenario dependent.

In CUT 236 presented in Figure 4.20, STAP SINR degradation is very significant falling as low as -18dB in frequencies outside of the clutter notch. This degradation is similar to targets in

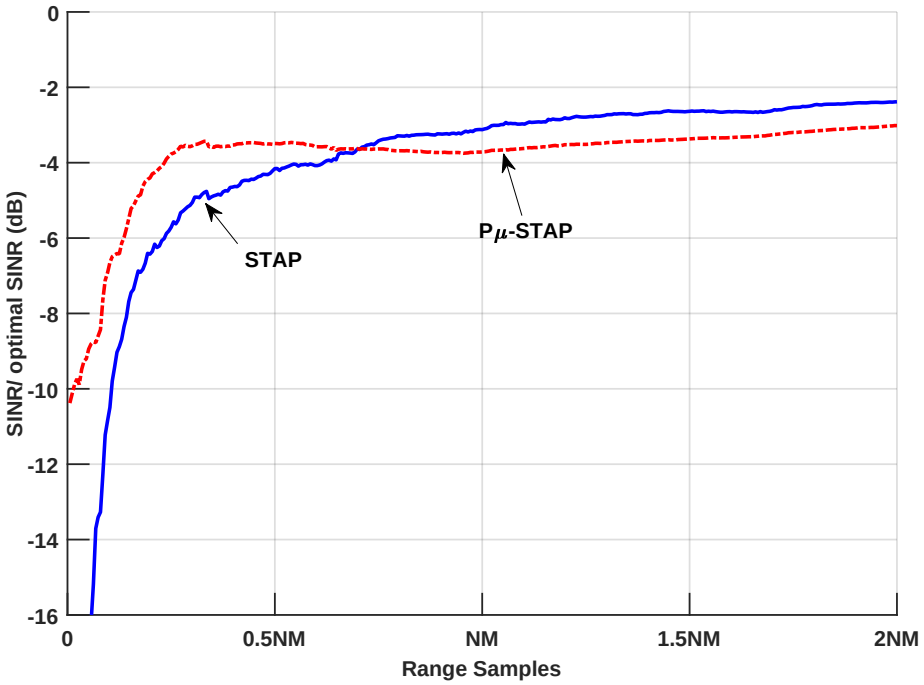

Figure 4.19: Average Improvement Factor in KASSPER Range Sample 27

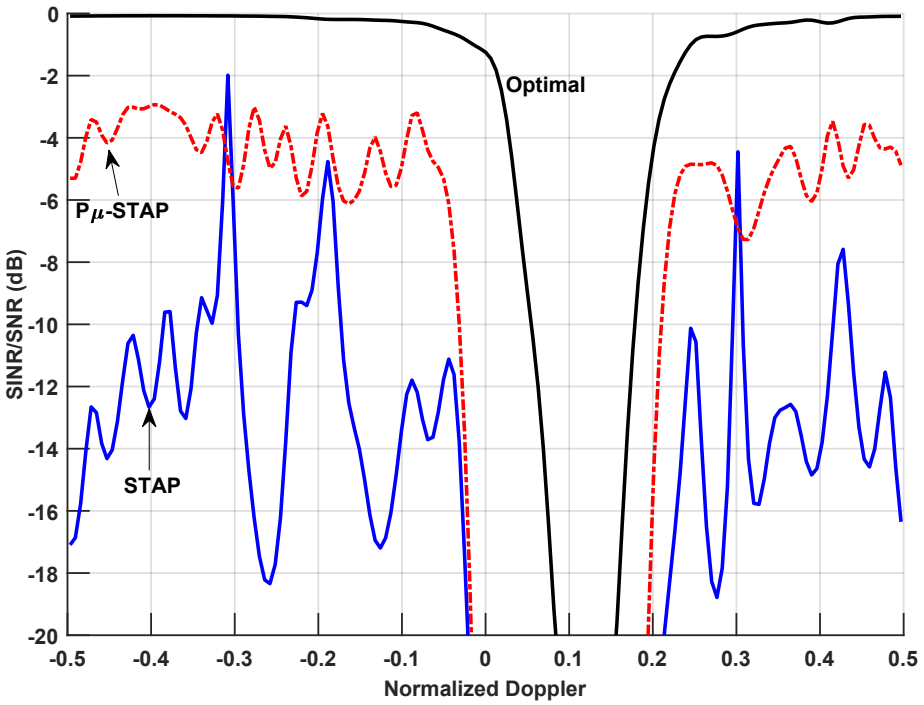

Figure 4.20: SINR Loss in KASSPER Range Sample 236

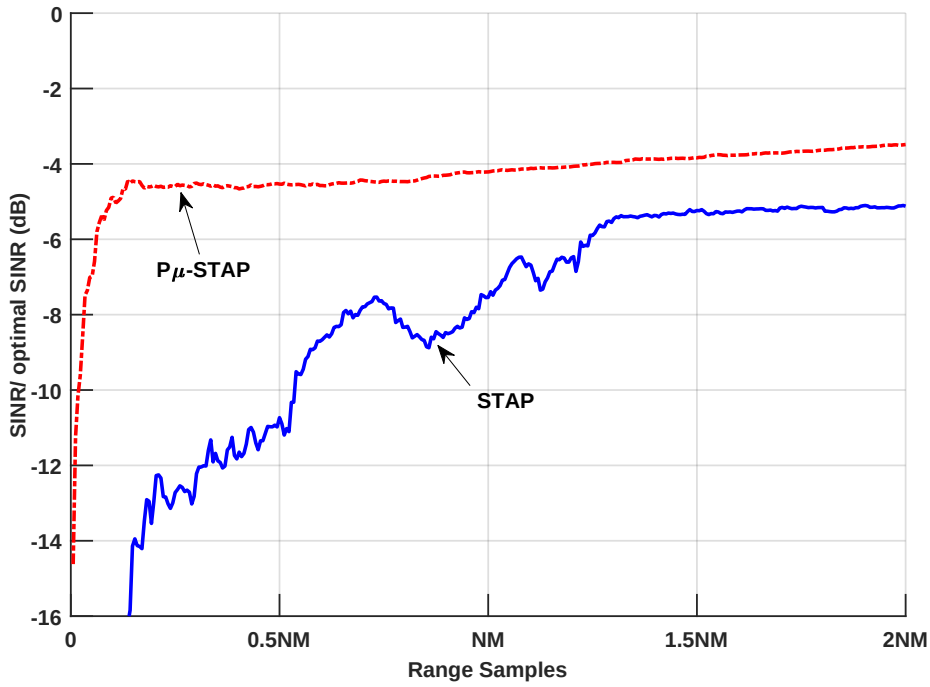

Figure 4.21: Average Improvement Factor in KASSPER Range Sample 236

the training data (Fig. 4.17) presented in the previous section. Pμ-STAP, in contrast, maintains a SINR performance having no less than $\eta = -7dB$. However, there are some frequencies where STAP still outperforms Pμ-STAP ($\omega = -0.31, 0.31$). Examination of AIF in 4.21 shows the stark improvement in SINR Pμ-STAP as a function of range sample intervals. Pμ-STAP reaches the asymptotic bound with very low sample support then slightly increases. Examining CUT 236 shows the great benefit Pμ-STAP can have in detection performance in the presence of significant heterogeneity. However, test CUT 400 shows the first instance of Pμ-STAP under performing.

In Figure 4.22, SINR loss in CUT 400 in low sample support is presented. Due to the high performance of STAP, the training data and test cell are homogeneous. Pμ-STAP performance is still excellent where $\eta_{P\mu} > -2.5dB$ in the detectable velocities. However, homogenization causes a opposite effect making the training data less i.i.d. In Fig 4.3, Pμ-STAP AIF shows that it does not need much support to have high SINR. Nevertheless, STAP performance is better as sample support increases.

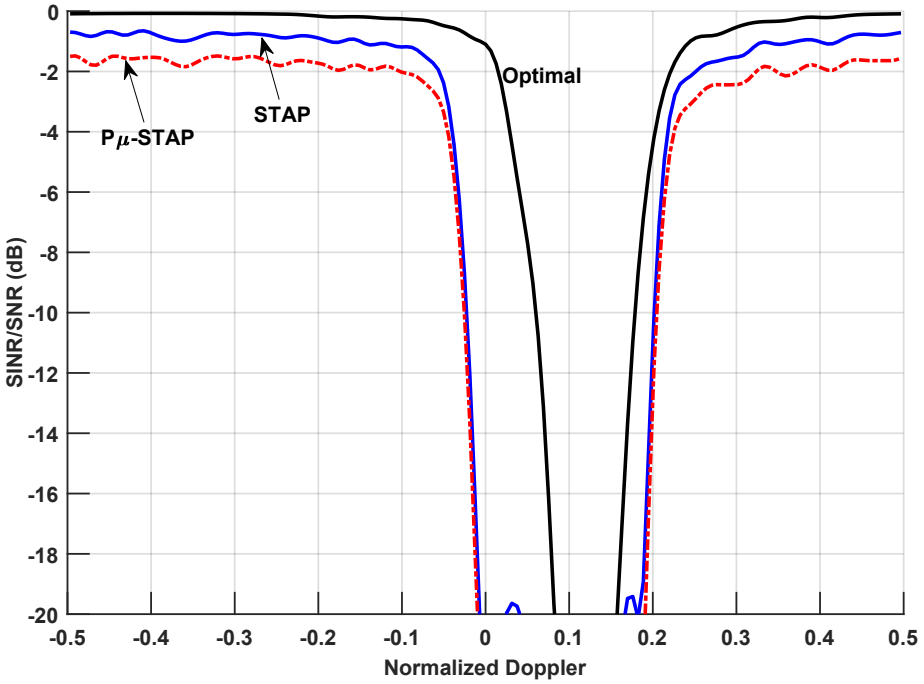

Figure 4.22: SINR Loss in KASSPER Range Sample 400

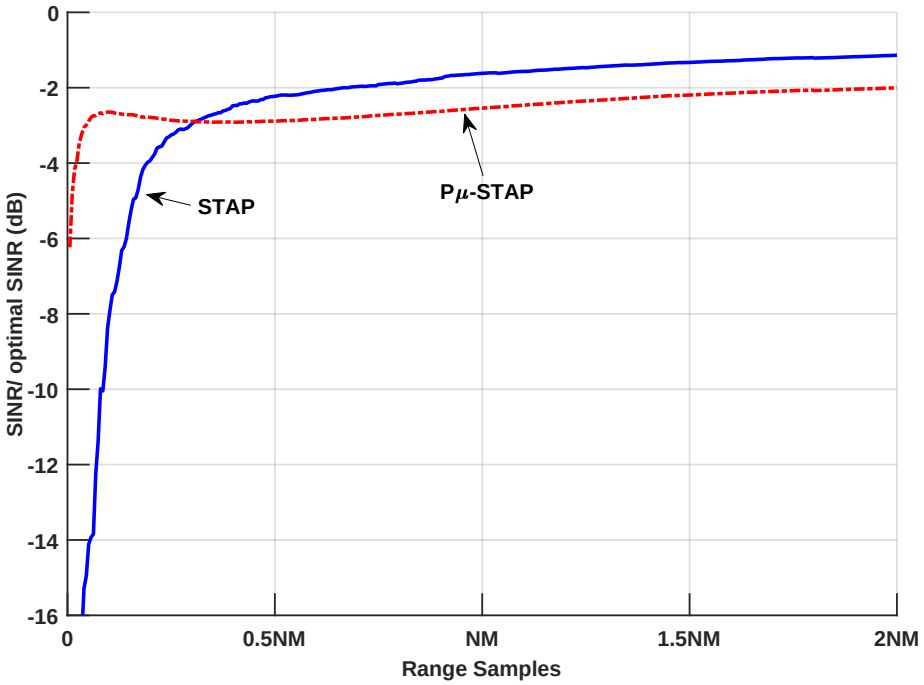

Figure 4.23: Average Improvement Factor in KASSPER Range Sample 400

In summary, the large performance boost Pμ-STAP provides in heterogeneous cells comes at the small expense of degradation in homogeneous cells. If this can be accepted, then Pμ-STAP is applicable under any circumstance. Otherwise, Pμ-STAP is an environment specific algorithm and needs to be further implemented on heterogeneous datasets to confirm this.

Chapter 5

Partially Adaptive Multi-Waveform Space-Time Adaptive Processing

Fully adaptive space-time adaptive processing has been assumed to this point. Fully adaptive refers to using all available degrees of freedom for clutter cancellation. Sample support necessary to satisfy RMB of $2MN-3$ may not be attainable due to constraints on the instantaneous bandwidth [3]. Also, the number of homogeneous samples in a range interval may not be available for accurate estimation of the fully adaptive covariance matrix. Additionally, inverting and estimating a covariance matrix for every range cell can be computationally expensive making it not be feasible for real-time application. The number of operations to estimate and invert covariance matrix is $\mathscr{O}(M^2N^2L)$ and $\mathscr{O}(M^3N^3)$, respectively [2]. Sample support constraints and computational cost is directly related to the amount of pulses and elements. Reduction of either will lead to less sample support requires and faster computations.

Partially adaptive STAP consist of reducing the temporal and/or spatial samples thereby reducing the amount of samples needed to satisfy the RMB rule. For temporal reduction, sub-CPIs is formed from the CPI either pre- or post-Doppler processing. Similarly, spatial reduction occurs when beamforming is performed on subarrays. In [3], a in-depth analysis of partially adaptive algorithms with STAP showed that partially adapting the STAP filter will improve the aforementioned challenges. Furthermore, partial adaptations improves clutter cancellation over fully adaptive. Still, it is not very robust in the presence of heterogeneous clutter.

Fully adaptive μ-STAP and Pμ-STAP is very robust to clutter heterogeneity as seen in the previous chapter. In addition, it outperforms STAP when each is faced with limited sample sup-

port. However, they have similar computation complexity as fully adaptive STAP. Although their inversion cost reminds the same, estimation slightly increases to $\mathscr{O}\left(M^2N^2\left(L_p+KL_s\right)\right)$. Since this is a common challenge, similar analysis of partially adaptive techniques for this multi-datacube formulation is necessary to determine if it will still provide the clutter estimation benefits.

The partial adaptation considered will be data-independent, e.g. non-adaptive, using DFT matrices [25]. Another method is principle components method. This uses a eigendecomposition of the estimated covariance matrix is to create a orthogonality projection remove the clutter[2; 25]. A eigendecomposition is has the same computational cost as a matrix inversion. Therefore, this method has a high computationally expense.

A overview of partially adaptive STAP from [3] will now be presented. Dimension reduction is performed using a linear transformation which characterizes the nature of the reduction, whether it be temporal, spatial or both. Define matrix $\mathbf{T}$ as a transformation matrix. In general, the transformation is applied to the covariance matrix and space-time steering vector as

$$\tilde{\mathbf{R}} = \mathbf{T}^H\mathbf{R}\mathbf{T} \tag{5.1}$$

$$\tilde{\mathbf{c}}_{\mathbf{st}} = \mathbf{T}^H\mathbf{c}_{st} \tag{5.2}$$

where $\mathbf{R}$ is the STAP covariance matrix. The transformed adaptive filter is therefore

$$\tilde{\mathbf{w}} = \tilde{\mathbf{R}}^{-1}\tilde{\mathbf{c}}_{st} = \left(\mathbf{T}^H\mathbf{R}\mathbf{T}\right)^{-1}\mathbf{T}^H\mathbf{c}_{st} \tag{5.3}$$

For analysis purposes to compare with fully adaptive STAP, it is best to map the transformed filter on the full dimension space by

$$\begin{aligned}\tilde{\mathbf{w}}_{\mathbf{c}} &= \mathbf{T}\tilde{\mathbf{w}} \\ &= \mathbf{T}\left(\mathbf{T}^H\mathbf{R}\mathbf{T}\right)^{-1}\mathbf{T}^H\mathbf{c}_{st}\end{aligned} \tag{5.4}$$

The incorporation of μ-STAP and Pμ-STAP consist of simply replacing their covariance matrix

with the STAP covariance matrix within (5.4).

Figure 5.1 diagrams the four possible combinations of dimension reduction. Element-space pre-Doppler is full array pre-beamforming, sub-CPI pre-Doppler processing temporal reduction. Element-space post-Doppler is full array pre-beamforming, sub-CPI post-Doppler processing temporal reduction. Beam-space pre-Doppler is a sub-array post-beamforming, sub-CPI pre-Doppler processing spatio-temporal reduction. Beam-space post-Doppler is a sub-array post-beamforming, sub-CPI post-Doppler processing spatio-temporal reduction. Some form of coherent integration is useful in the dimension reduction. Therefore, element-space pre-Doppler will be excluded from analysis.

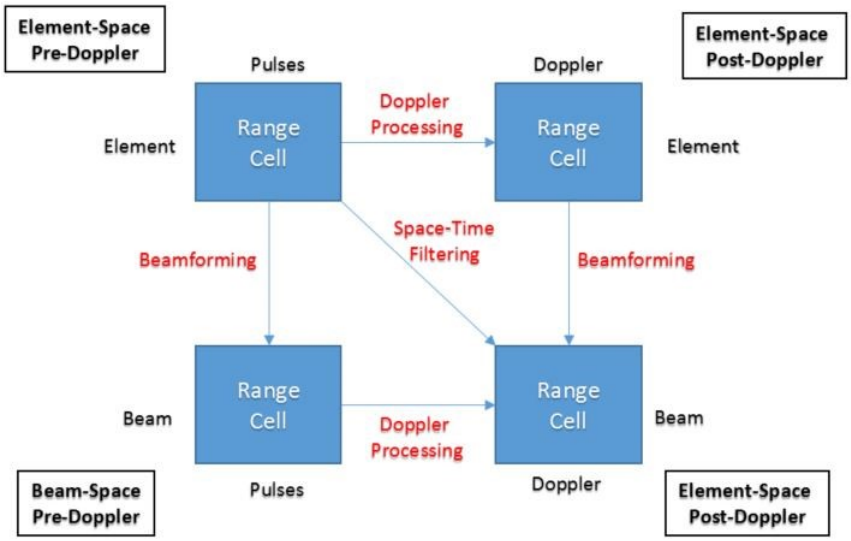

Figure 5.1: Partially Adaptive Algorithms [3]

The incorporation of the family of μ-STAP algorithms is fairly straight forward. The receiver processing chain for partially adaptive Pμ-STAP is presented in Figure 5.2. The receive data is pulse compressed and passed through the match filter. Discretization is perform using a analog-to-digital converter. After, homogenization is performed using Pμ-STAP filters. Covariance estimation is performed then aggregated to produce the Pμ-STAP covariance matrix. The covariance is transformed then feed into the STAP processor. In the processor, the space-time steering vectors are transformed, the partially adaptive filter is created, and applied to the pulse compressed

data, $\mathbf{z}(\ell)$. Whether it is MIMO, SIMO pre-pulse compression, or SIMO post-pulse compression μ-STAP, a single covariance is generated after aggregation (3.15,4.5). Therefore, the following partially adaptive techniques is generalized to the family of μ-STAP algorithms.

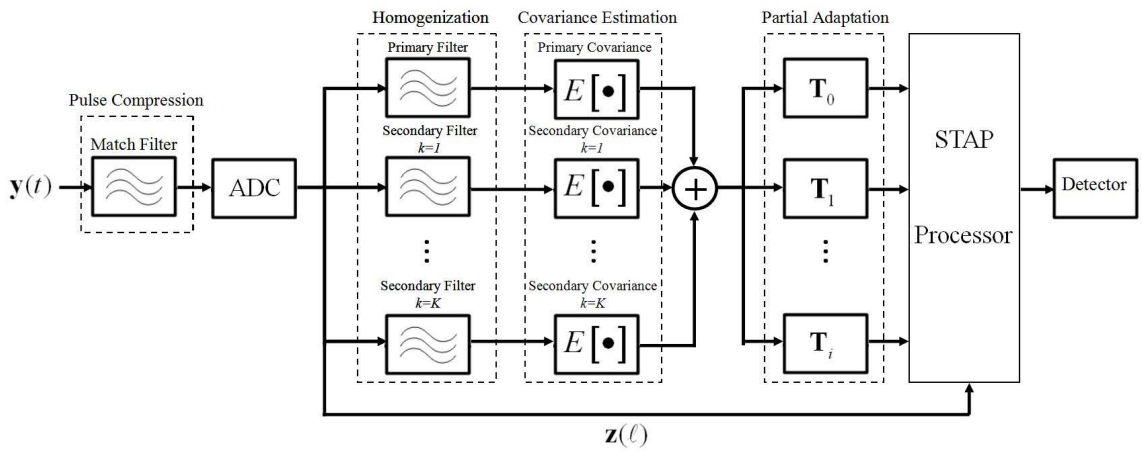

Figure 5.2: Recieve Processing Chain for Partial Adaptive μ-STAP

In the following sections, a similar SINR analysis to Chapter 4 is performed. A $N = 11$ element uniform linear array with $d = \lambda_c/2$ spacing emits $M = 21$ pulses in a CPI. The platform is traveling at $\beta = 1$. Table 5.1 shows the simulated test flight parameters. The waveform is a optimized polyphase-coded FM waveform [12; 13] with a $B\tau = 100$. PCFM waveforms use continuous phase modulation form a code to generate a non-linear FM waveform. Non-linear FM waveform provide great sidelobe benefits. Generation of this waveform is outlined in Appendix A of [10]. Four homogenization filters with a length of $BT = 2B\tau - 1$ are used. In Figure 5.3, the primary (in black) and secondary homogenization response for a optimized PCFM is depicted. The three clutter scenarios are examined: heterogeneous, clutter discrete in CUT, target in training data. The clutter-to-noise ratio is 54dB. Additive noise is complex white Gaussian. The following sections will now present the transformation matrix generation injunction with $\mu - STAP$.

Table 5.1: Simulated Test Flight 2 Parameters

Optimized PCFM waveform, $B\tau = 100$
N=11 elements in ULA
M=21 pulses in CPI
$\beta = 1$ interelement spacing in one PRI

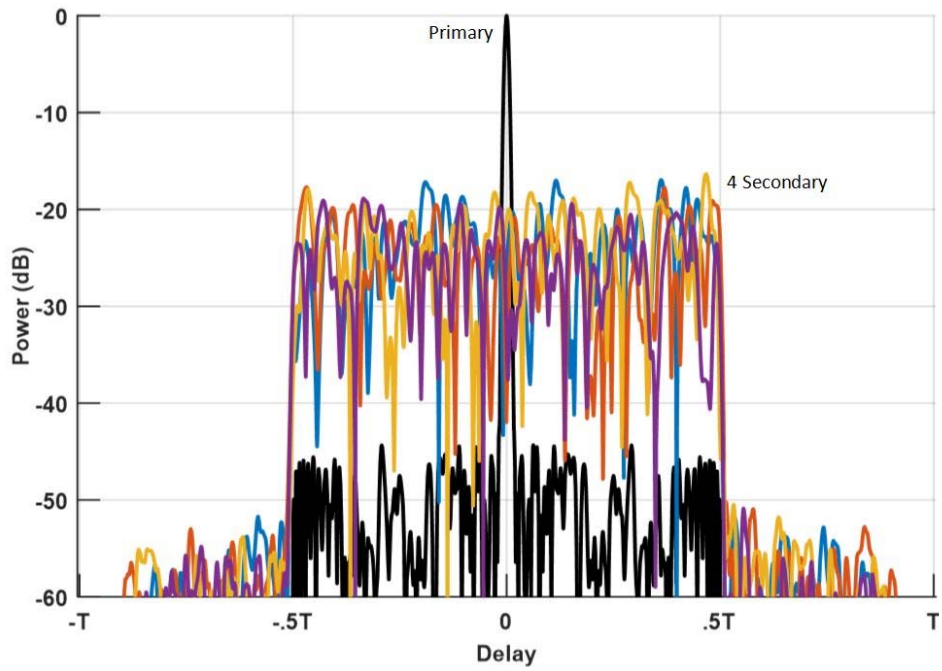

Figure 5.3: Primary and Secondary Homogenization Filter Responses for PCFM Waveform

5.1 Element-Space Post-Doppler

In this section, Element-space multi-window post-Doppler μ-STAP is presented. This work was previously presented in [26]. Element-space multi-window post-Doppler (ESPoD) μ-STAP employs different Doppler filters to the pulsed echoes received at each antenna element. In other words, for ESPoD the processing in Doppler is non-adaptive and localized to a set of D_t Doppler bins. Spatial processing is then fully adaptive across the antenna elements. Therefore, each antenna element has an identical bank of D_t filters for the mth Doppler bin to form a space-time transformation matrix

$$\mathbf{T}_m = \tilde{\mathbf{F}}_m \otimes \mathbf{I}_N \tag{5.5}$$

where $\tilde{\mathbf{F}}_m$ is an matrix consisting of $M \times D_t$ filters of D_t length-M for the mth Doppler bin and I_N is a $N \times N$ identity matrix corresponding to the N antenna elements [3]. The set of filters used to form the Doppler filter bank in (5.5) can be selected in two ways: PRI-staggered [3] and adjacent-Bin [27].

PRI-staggered develops a Doppler filter that is a subset of the entire Doppler filters and slides this filter over sub-CPIs. A set of M' sub-CPIs is given a set of M pulses by

$$M' = M - D_t + 1 \tag{5.6}$$

Define $\mathbf{U} = [\mathbf{u}_0 \quad \mathbf{u}_1 \quad \cdots \quad \mathbf{u}_{M-1}]$ as a $M' \times M$ DFT matrix constructed from the first M' rows of a DFT matrix where each $\mathbf{u}_m$ is length $M' \times 1$. Also, define $\mathbf{b}_1$ as a $M' \times 1$ taper. The mth Doppler filter is defined as [3]

$$\mathbf{f}_m = \mathbf{b}_1 \odot \mathbf{u}_m^* \tag{5.7}$$

where $\odot$ is a Hadamard product and $(\bullet)^*$ denotes complex conjugation. A $M \times D_t$ Toeplitz matrix is formed for the mth Doppler filter bank

$$\tilde{\mathbf{F}}_m = \begin{bmatrix} \mathbf{f}_m(0) & 0 & \cdots & \cdots & 0 & 0 \\ \mathbf{f}_m(1) & \mathbf{f}_m(0) & \ddots & & \vdots & \vdots \\ \vdots & \mathbf{f}_m(1) & \ddots & \ddots & \vdots & \vdots \\ \mathbf{f}_m(M'-1) & \vdots & & \ddots & 0 & \vdots \\ 0 & \mathbf{f}_m(M'-1) & & & \mathbf{f}_m(0) & 0 \\ \vdots & 0 & \ddots & & \mathbf{f}_m(1) & \mathbf{f}_m(0) \\ \vdots & \vdots & \ddots & \ddots & \vdots & \mathbf{f}_m(1) \\ \vdots & \vdots & & \ddots & \mathbf{f}_m(M'-1) & \vdots \\ 0 & 0 & \cdots & \cdots & 0 & \mathbf{f}_m(M'-1) \end{bmatrix} \tag{5.8}$$

Adjacent-bin post-Doppler combines spatial samples from D_t neighboring Doppler bins centered about the mth center bin such that the Doppler bins used for adapting to the mth bin are

indexed as $m-P,\ldots,m,\ldots,m+P$, where

$$P=(D_t-1)/2 \tag{5.9}$$

A similar DFT matrix $\mathbf{U}$ used for adjacent-Bin except $\mathbf{u}_m$ is length $M\times 1$. Define $\mathbf{b}_2$ as a $M\times 1$. The tapered mth Doppler filter is defined as

$$\mathbf{f}_m=\mathbf{b}_2\odot\mathbf{u}_m^* \tag{5.10}$$

The mth Doppler filter bank used in (5.5) is then given as

$$\tilde{\mathbf{F}}_m=[\mathbf{f}_{m-P}\cdots\mathbf{f}_m\cdots\mathbf{f}_{m+P}] \tag{5.11}$$

For adjacent-Bin, note that D_t must be odd and the Doppler filter bank should wrap around the edges of the Doppler space. Tapering differs for PRI-staggered and adjacent-Bin. In order to ensure the matrix is full-rank, a tapering must be applied to the PRI-staggered. Typically a 20-30dB Chebychev taper is suffice. The same is not necessary for adjacent-Bin. A uniform taper is typically used unless additional sidelobe suppression is warranted. The transformed covariance for μ-STAP (3.13) or Pμ-STAP (3.17) using general transformation formulation described in (5.1) and the ESPoD transformation matrix is

$$\begin{aligned}
\tilde{\mathbf{R}}_{\mu,m}(\ell)&=\mathbf{T}_m^H\hat{\mathbf{R}}_{\mu}(\ell)\mathbf{T}_m\\
\tilde{\mathbf{R}}_{\mu,m}(\ell)&=\mathbf{T}_m^H\hat{\mathbf{R}}_{\text{prime}}(\ell)\mathbf{T}_m+\mathbf{T}_m^H\hat{\mathbf{R}}_{\mu,NP}(\ell)\mathbf{T}_m\\
\tilde{\mathbf{R}}_{\mu,m}(\ell)&=\tilde{\mathbf{R}}_{\text{prime},m}(\ell)+\tilde{\mathbf{R}}_{\mu,NP,m}(\ell)
\end{aligned} \tag{5.12}$$

Similarly, the ESPoD transformed space-time steering vector is

$$\tilde{\mathbf{c}}_{st,m}(\theta,\omega)=\mathbf{T}_m^H\mathbf{c}_{st}(\theta,\omega) \tag{5.13}$$

Therefore, the mth transformed μ-STAP adaptive filter is obtained in a similar fashion to (5.3) is

$$\begin{aligned}\tilde{\mathbf{w}}_m(\ell,\theta,\omega) &= \tilde{\mathbf{R}}_m^{-1}(\ell)\,\tilde{\mathbf{c}}_{st,m}(\theta,\omega)\\ &= \left(\mathbf{T}_m^H\hat{\mathbf{R}}(\ell)\,\mathbf{T}_m\right)^{-1}\mathbf{T}_m^H\mathbf{c}_{st}(\theta,\omega)\end{aligned} \tag{5.14}$$

where $\hat{\mathbf{R}}(\ell)$ corresponds to primary only, non-primary, or μ-STAP sample covariance matrix. Note that difference in line style/color combinations than in previous chapters as shown in Table 5.2. A solid line denotes a STAP, dashed line denotes SIMO Pμ-STAP, and dotted line denotes SISO Pμ-STAP. The different color represent a different reduction amount.

Table 5.2: Training Data Combinations in SINR Analysis of Partial Adaption

Training Data	**Line style/color**
Fully adaptive, SISO STAP	solid blue
Fully adaptive, SIMO Pμ-STAP $K=4$	dashed blue
Fully adaptive, SISO Pμ-STAP $K=1$	dotted blue
Partially adaptive, SISO STAP	solid red
Partially adaptive, SIMO Pμ-STAP $K=4$	dashed red
Partially adaptive, SISO Pμ-STAP $K=1$	dotted red
Partially adaptive, SISO STAP	solid green
Partially adaptive, SIMO Pμ-STAP $K=4$	dashed green
Partially adaptive, SISO Pμ-STAP $K=1$	dotted green

In the first analysis, ESPoD is examined in heterogeneous clutter. The post-Doppler algorithms reduce $M=21$ to $D_{t,1}=5$ and $D_{t,2}=11$ pulses in each sub-CPI to compare the two sample support regimes. Partial adaptivity does not occur over element-space. Therefore, the number of elements remain the same at N. For tapering, PRI-Staggered processing uses a 20dB Chebychev taper and adjacent-Bin processing is uniformly tapered. Fully adaptive STAP algorithms are also shown for completeness.

5.1.1 Heterogeneous Clutter

Low sample support of $.5NM=115.5$ will have enough samples to satisfy RMB rule reducing to $2ND_{t,1}=110$. Therefore, a SINR loss analysis will be performed at $n(L)=2ND_{t,1}$. Consider

PRI-Staggered algorithm presented in Fig. 5.4 Partially adaptation provides a benefit of performance for STAP and Pμ-STAP. A lobing effect occurs when reducing to $D_{t,1} = 5$. It consistent for STAP and Pμ-STAP. This effect was similarly seen in [3]. It is due to mismatch loss from implementing the staggered Doppler filters. Note this doesn't occur at $D_{t,1} = 11$. Nonetheless, Pμ-STAP provides a benefit over STAP. The amount of benefit Pμ-STAP has over STAP decreases proportionally with decreeing number of pulses in a sub-CPI. This is expected since the sample support for partially adaptive STAP satisfies the RMB rule. Overall, STAP SINR loss is less than Pμ-STAP.

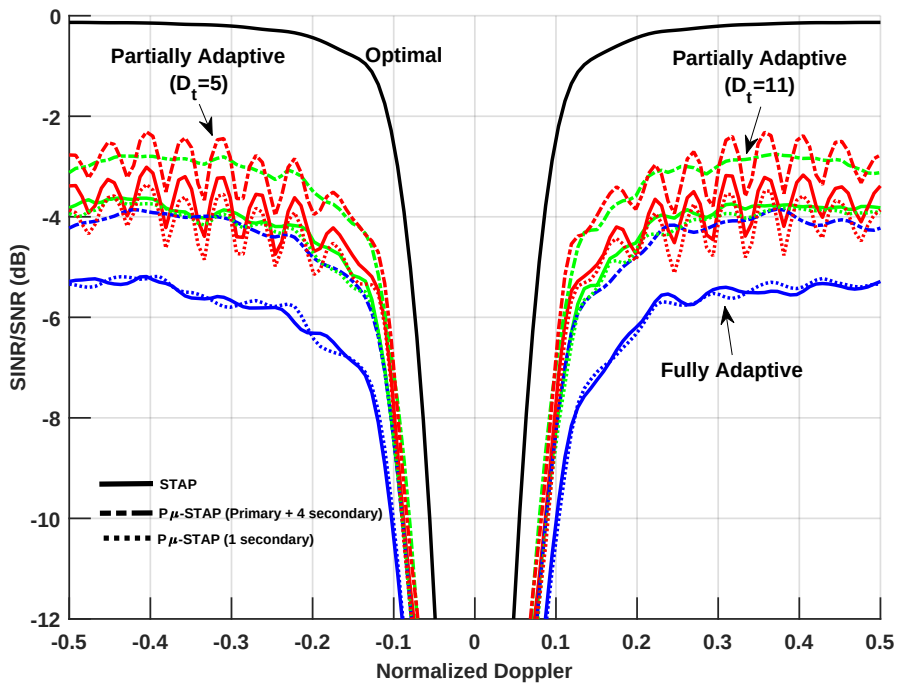

Figure 5.4: ESPoD PRI-Staggered SINR Loss at $2ND_t$ in Heterogeneous Clutter

Figure 5.5 shows the average improvement factor for ESPoD. AIF between between $D_{t,1} = 5$ and $D_{t,2} = 11$ for Pμ-STAP is indistinguishable. Based on the lack of straddling by $D_{t,2} = 11$ seen in SINR Loss from Fig. 5.4, it can be consider as superior. Both are better than STAP. As sample support increases, STAP reduction of $D_{t,1} = 5$ improves at a faster rate than $D_{t,2} = 11$. ESPoD adjacent-Bin will now be considered in Figure 5.6. The filter mismatch is consistent in STAP and Pμ-STAP. The greater the amount of reduction, the greater the benefit. For each reduction

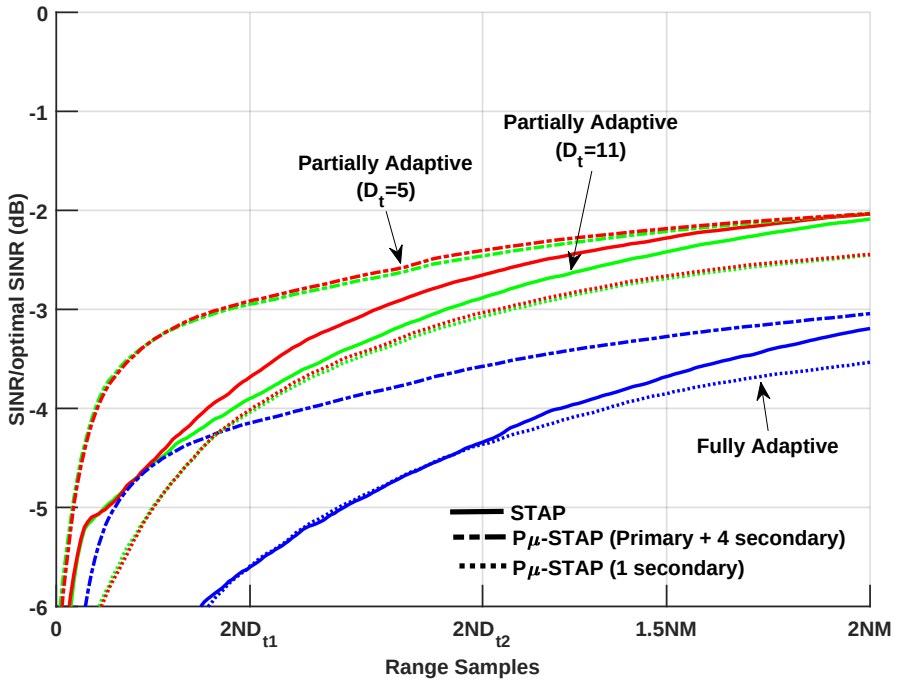

Figure 5.5: ESPoD PRI-Staggered Average Improvement Factor in Heterogeneous Clutter

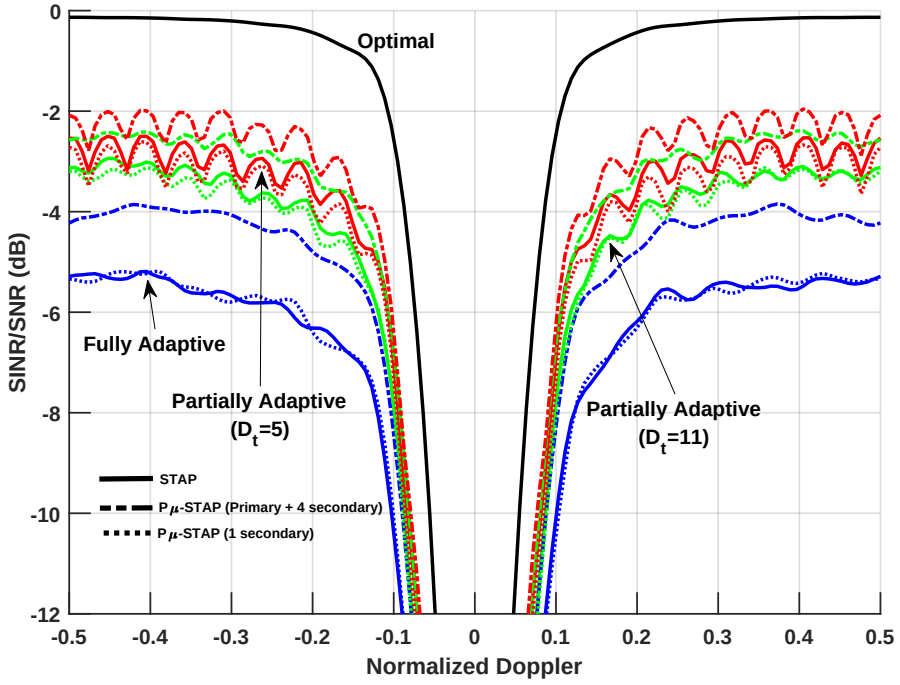

Figure 5.6: ESPoD Adjacent-Bin SINR Loss at $2ND_t$ in Heterogeneous Clutter

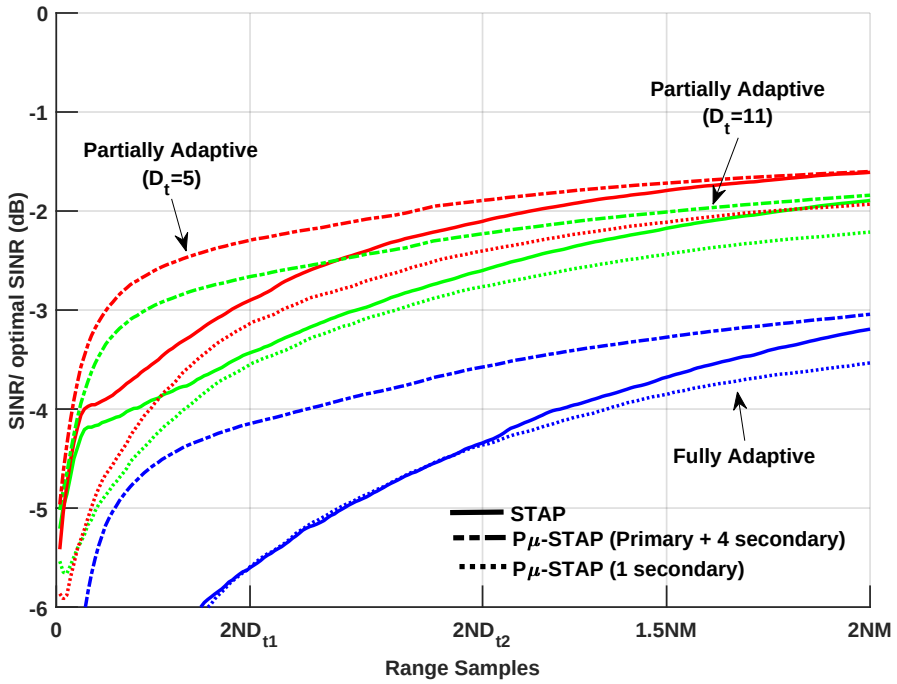

Figure 5.7: ESPoD Adjacent-Bin Average Improvement Factor in Heterogeneous Clutter

Pμ-STAP is marginally better than STAP. In Figure 5.7, the AIF of adjacent-Bin ESPoD. As the number of sub-CPIs are reduced, Pμ-STAP provides dwindling improvement over STAP. In spite of this, Pμ-STAP compared to STAP is in the small sample support regime, which is the most realistic regime for an operational system. Comparing PRI-Staggered (Fig. 5.5) and adjacent-Bin (Fig. 5.7), the latter AIF is greater than the former by .5dB.

In summary, Pμ-STAP is applicable in element-space post-Doppler processing. In each reduction algorithm, Pμ-STAP detection performance is better than STAP. However, the improvement Pμ-STAP has over STAP is not as much as in full adaptation since the RMB rule has been decreased.

5.1.2 Clutter Discrete in CUT

In Figure 5.8, ESPoD PRI-staggered is examined in heterogeneous clutter with a 20dB clutter discrete in the CUT. Pμ-STAP robustness to a clutter discrete in fully adaptive processing also occurs in partial adaptation. STAP performance degradation is greater than Pμ-STAP for both

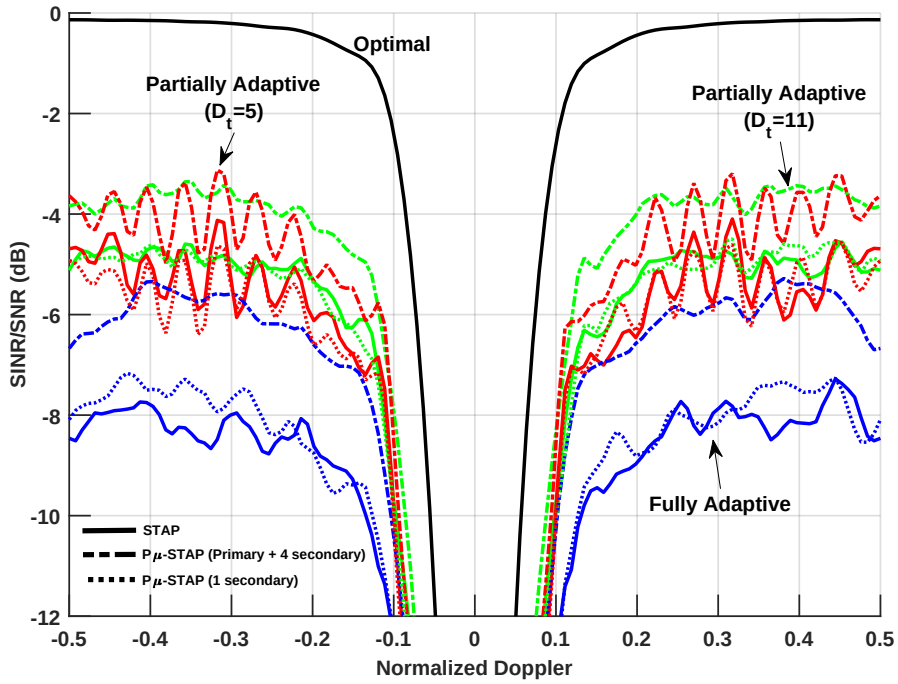

Figure 5.8: ESPoD PRI-Staggered SINR Loss at $2ND_t$ with Clutter Discrete in CUT

reductions. Regarding reduction amounts, $D_{t,2} = 11$ performance is greater than $D_{t,2} = 5$. In ESPoD PRI-staggered for heterogeneous clutter without a clutter discrete, the lower reduction was on average the same as its counterpart. Here, the lower reduction loses fidelity due to clutter discrete. Also, no significant straddling mismatch occurs at $D_{t,2} = 11$. The AIF in Fig. 5.9 further confirms loss in performance of $D_{t,2} = 5$. The performance curve for $D_{t,2} = 5$ is less than $D_{t,2} = 11$ for each STAP algorithm. Pμ-STAP has a $AIF(2ND_{t,2}) = 3.8dB$ and STAP is $AIF(2ND_{t,2}) = 4.9dB$. A full 1dB improvement even with partially adaptive STAP satisfying RMB rule. ESPoD adjacent-Bin SINR loss is presented in Figure 5.10. The adjacent-Bin algorithm is less robust to the clutter discrete as the filter mismatch causing straddling across normalized Doppler is greater than previously seen. Again, the algorithm does not affect STAP or Pμ-STAP independently. Also, Pμ-STAP continues to show a SINR benefit. The AIF in Fig. 5.11 shows adjacent-Bin Pμ-STAP provides a performance increase.

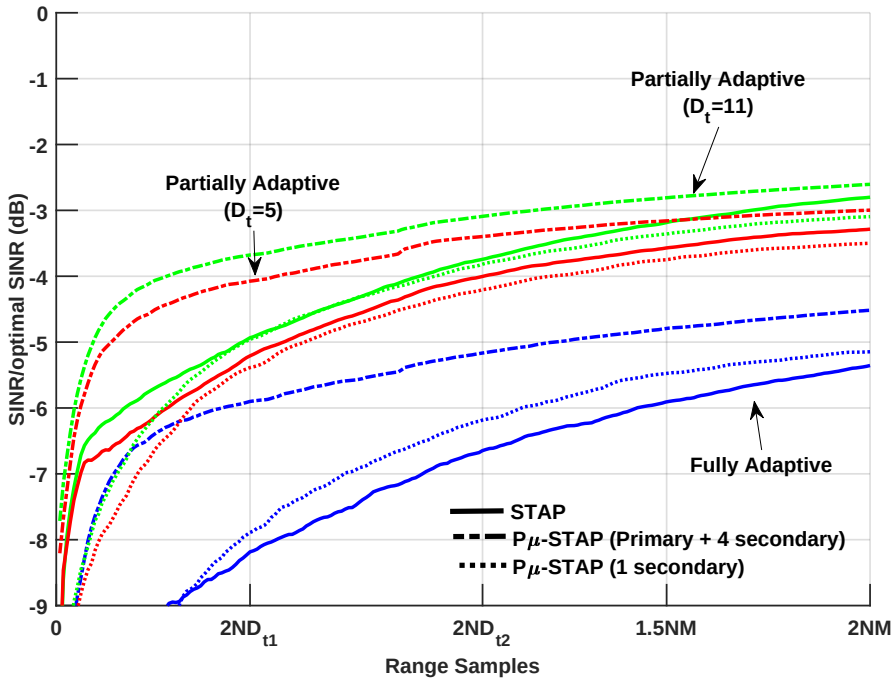

Figure 5.9: ESPoD PRI-Staggered Average Improvement Factor with Clutter Discrete in CUT

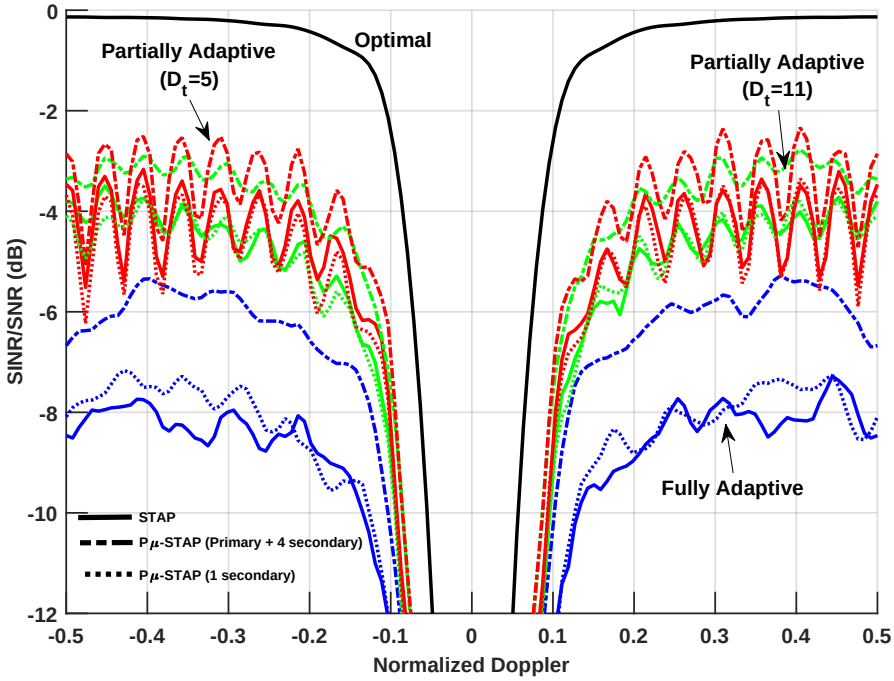

Figure 5.10: ESPoD Adjacent-Bin SINR Loss at $2ND_t$ with Clutter Discrete in CUT

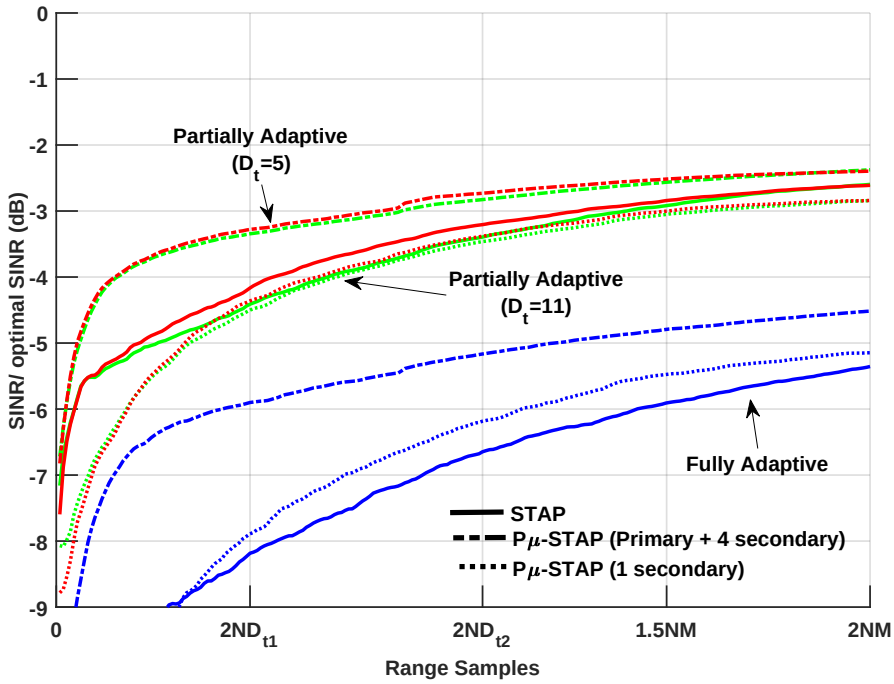

Figure 5.11: ESPoD Adjacent-Bin Average Improvement Factor with Clutter Discrete in CUT

5.1.3 Targets in Training Data

Lastly, ESPoD is examined in heterogeneous clutter with targets in training data. Ten targets were placed in training samples (5 one each side of CUT after guard cells) in a heterogeneous clutter. The target power of each was 15dB SNR. Partially adaptive STAP robustness to self-cancellation is less than fully adaptive Pμ-STAP as seen at $\omega = .49$. It even falls below SISO Pμ-STAP. Each of these are also effected by self-cancellation. However, for Pμ-STAP, a 3dB benefit occurs when reducing to $D_{t,1} =$. For adjacent-Bin in Fig 5.13, the robustness as far better. The self-cancellation notch is greater than fully adaptive performance in one instance.

A couple conclusions can be made about ESPoD. Adjacent-bin provides a higher average improvement factor over PRI-staggered but has higher mismatch loss. If moderate sample support is desired when performing ESPoD, PRI-staggered will provided the best response where mismatch is at a minimal. If low sample support is required, on average, adjacent-Bin will best option. The behavior of these partially adaptive algorithms is consistent in Pμ-STAP and STAP. In spite of these, Pμ-STAP SINR performance was always greater by at least 1dB at low sample support. In

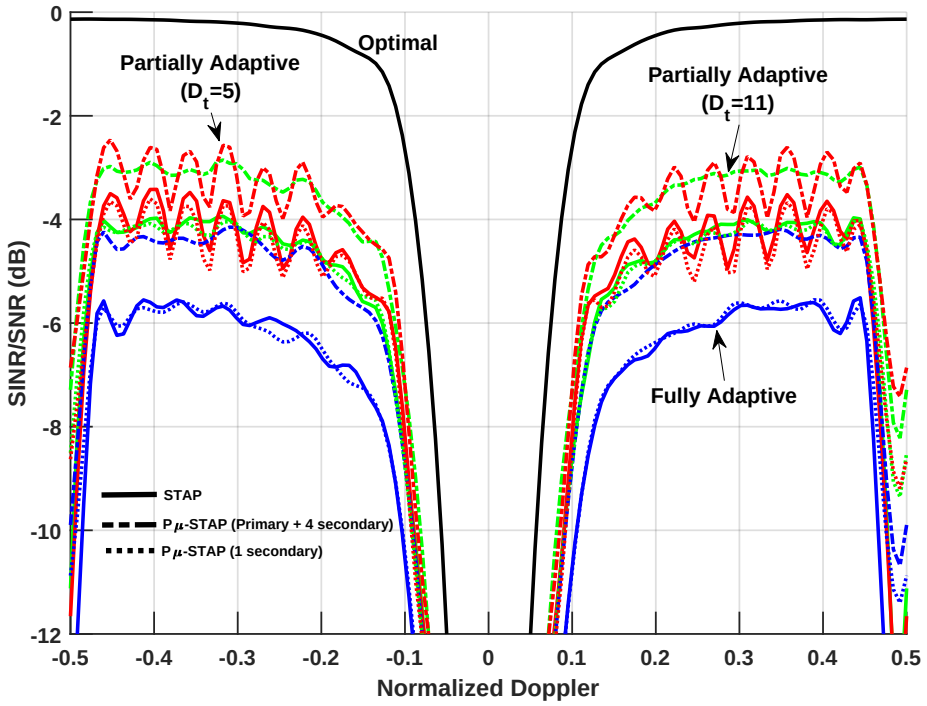

Figure 5.12: ESPoD PRI-Staggered SINR Loss at $2ND_t$ with Targets in Training Data

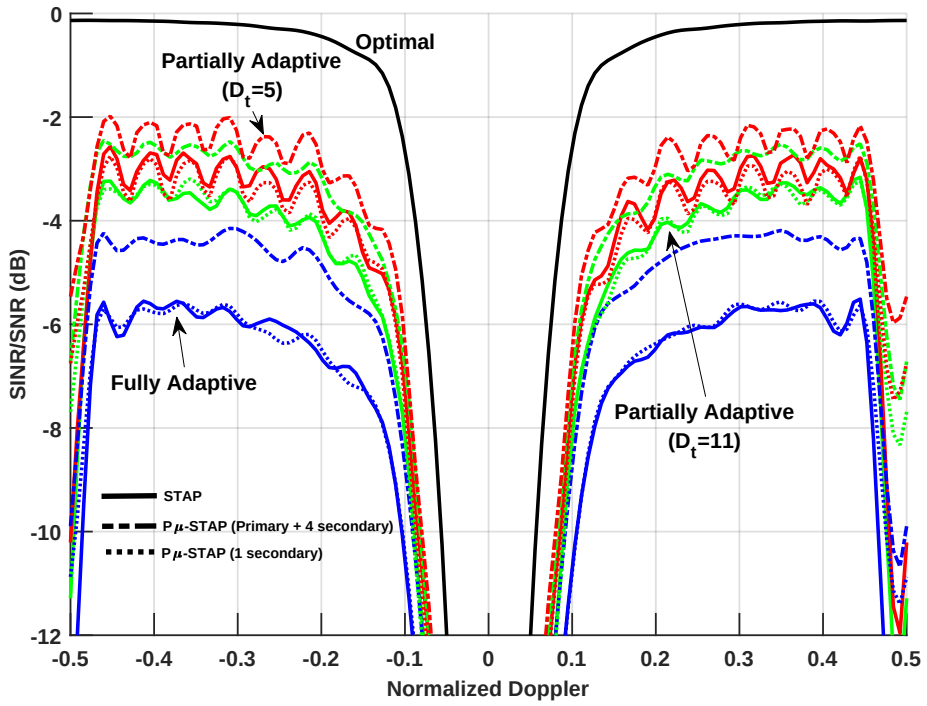

Figure 5.13: ESPoD Adjacent-Bin SINR Loss at $2ND_t$ with Targets in Training Data

the presence of targets in training data, simulated results show both partially adaptive algorithms in Pμ-STAP are very robust.

5.2 Beam-Space Pre-Doppler

Beam-space pre-Doppler (BSPrD) are a set of techniques related to displaced phase center antenna processing (DPCA) [4] and is a dual of element-space post-Doppler, where spatial beamforming is performed before adaptive processing. The temporal adaptive processing may be carried out across the full temporal space, but the amount of pulses within a CPI is often fairly large. Therefore, it is more efficient to reduce the MN-dimensional problem by applying beamformers over a subset of slow-time samples. A CPI of M pulses are subdivided into a set of M' sub-CPIs consisting of D_t pulses determined from (5.6).

Each m'th sub-CPI has an identical bank of D_s beamformers for the nth antenna element to form a $MN \times D_t D_s$ space-time transformation matrix

$$\mathbf{T}_{m'n} = \mathbf{J}_{m'} \otimes \mathbf{G}_n \tag{5.15}$$

where $\mathbf{J}_{m'}$ is a sub-CPI selection matrix for sub-CPI m' and $\mathbf{G}_n$ is the nth beamformer matrix. The space-time dimension reduction total is $D = D_t D_s$. The selection matrix is formed by

$$\mathbf{J}_{m'} = \begin{bmatrix} \mathbf{0}_{m' \times D_t} \\ \mathbf{I}_{D_t} \\ \mathbf{0}_{(M-D_t-m') \times D_t} \end{bmatrix} \tag{5.16}$$

The reduced dimension beamforming matrix $\mathbf{G}_n$ can be structured in two manners: displaced-beam and adjacent-beam. These have similar structures to aforementioned PRI-staggered and adjacent-Bin, respectively. PRI-staggered can be consider as standard DPCA and adjacent-Bin is similar to DPCA using sum and difference beams [3; 4]. For displace-beam pre-Doppler, a set of N'

sub-apertures given a set of N elements are

$$N' = N - D_s + 1 \tag{5.17}$$

Define a $N \times N$ DFT matrix constructed from the first N' rows of a DFT matrix and a_1 be an $N' \times 1$ taper. The nth beamformer is defined as [3]

$$\mathbf{g}_n = \mathbf{b}_{DB} \odot \mathbf{u}_n^* \tag{5.18}$$

A $N \times D_S$ beamformer matrix is then formed in a Toeplitz structure similar to (5.8)

$$\tilde{\mathbf{G}}_n = \begin{bmatrix} \mathbf{g}_n(0) & 0 & \cdots & \cdots & 0 & 0 \\ \mathbf{g}_n(1) & \mathbf{g}_n(0) & \ddots & & \vdots & \vdots \\ \vdots & \mathbf{g}_n(1) & \ddots & \ddots & \vdots & \vdots \\ \mathbf{g}_n(M'-1) & \vdots & & \ddots & 0 & \vdots \\ 0 & \mathbf{g}_n(M'-1) & & & \mathbf{g}_n(0) & 0 \\ \vdots & 0 & \ddots & & \mathbf{g}_n(1) & \mathbf{g}_n(0) \\ \vdots & \vdots & \ddots & \ddots & \vdots & \mathbf{g}_n(1) \\ \vdots & \vdots & & \ddots & \mathbf{g}_n(M'-1) & \vdots \\ 0 & 0 & \cdots & \cdots & 0 & \mathbf{g}_n(M'-1) \end{bmatrix} \tag{5.19}$$

Adjacent-beam combines temporal samples from D_s adjacent beams centered about the nth bin center frequency such that $n-Q, \ldots, n, \ldots, n+Q$, where

$$Q = (D_s - 1)/2. \tag{5.20}$$

The reduced dimension beamformer matrix for the nth antenna element is defined as

$$\tilde{\mathbf{G}}_n = [\mathbf{g}_{n-Q} \cdots \mathbf{g}_n \cdots \mathbf{g}_{n+Q}]. \tag{5.21}$$

In [3], an in-depth analysis of the impact of various beamformer matrix implementations. Here traditional spatial beamforming in a single look direction θ_{look}. The transformation is also applied to the space-time steering vector such that

$$\tilde{\mathbf{c}}_{st,m',n}\left(\theta_{look},\omega\right) = \mathbf{T}_{m'n}^{H}\mathbf{c}_{st}\left(\theta_{look},\omega\right) \tag{5.22}$$

where $\tilde{\mathbf{c}}_{st,m',n}\left(\theta_{look},\omega\right)$ is $D_t D_s \times 1$. These outputs are applied to the μ-STAP SCMs to form

$$\begin{aligned}
\tilde{\mathbf{R}}_{\mu,m',n}\left(\ell\right) &= \mathbf{T}_{m',n}^{H}\hat{\mathbf{R}}_{\mu}\left(\ell\right)\mathbf{T}_{m',n} \\
\tilde{\mathbf{R}}_{\mu,m',n}\left(\ell\right) &= \mathbf{T}_{m',n}^{H}\hat{\mathbf{R}}_{\text{prime}}\left(\ell\right)\mathbf{T}_{m',n} + \mathbf{T}_{m',n}^{H}\hat{\mathbf{R}}_{\mu,NP}\left(\ell\right)\mathbf{T}_{m',n} \\
\tilde{\mathbf{R}}_{\mu,m',n}\left(\ell\right) &= \tilde{\mathbf{R}}_{\text{prime},m',n}\left(\ell\right) + \tilde{\mathbf{R}}_{\mu,NP,m',n}\left(\ell\right)
\end{aligned} \tag{5.23}$$

Therefore, the nth adaptive beamformer for the m' sub-CPI is

$$\begin{aligned}
\tilde{\mathbf{w}}_{m',n}\left(\ell,\theta,\omega\right) &= \tilde{\mathbf{R}}_{m',n}^{-1}\left(\ell\right)\tilde{\mathbf{c}}_{st,m',n}\left(\theta,\omega\right) \\
&= \left(\mathbf{T}_{m',n}^{H}\hat{\mathbf{R}}\left(\ell\right)\mathbf{T}_{m',n}\right)^{-1}\mathbf{T}_{m',n}^{H}\mathbf{c}_{st}\left(\theta,\omega\right)
\end{aligned} \tag{5.24}$$

where $\hat{\mathbf{R}}\left(\ell\right)$ corresponds to primary only, non-primary, or μ-STAP sample covariance matrix.

5.2.1 Heterogeneous Clutter

In the following analyses, $N = 11$ is reduced to $D_s = 5$ and $M = 21$ to $D_{t,1} = 5$ and $D_{t,2} = 11$.The multi-dimension reduction decreases sample support of the test parameters to $2D_sD_{t,1} = 50$. SINR loss analysis will be performed at $n(L) = 2D_sD_{t,1}$. The BSPrD analysis begins in Figure 5.14 showing displace-beam with heterogeneous clutter. The lobing effect from mismatch loss for the BSPrD is quite significant. Fortunately, this is consist between STAP and Pμ-STAP. Therefore, it is not a by product of covariance matrices but the reduction algorithms. As typically seen, Pμ-STAP SINR performance is greater than STAP. In Fig. 5.15, AIF for displaced-beam BSPrD is presented. As expected, Pμ-STAP improvement factor is also greater than STAP.

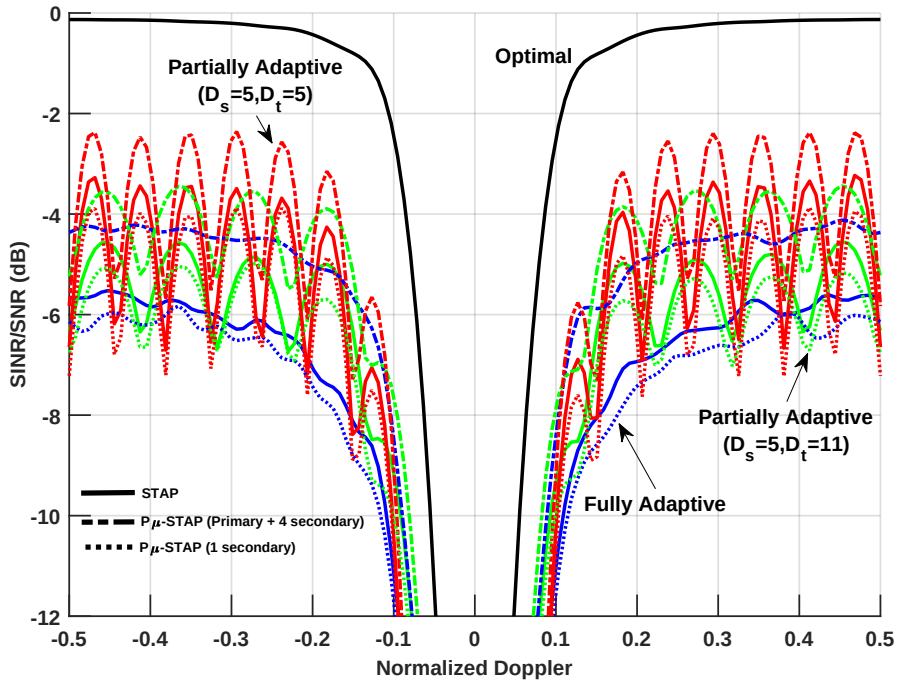

Figure 5.14: BSPrD Displace-Beam SINR Loss at $2D_sD_{t,1}$ in Heterogeneous Clutter

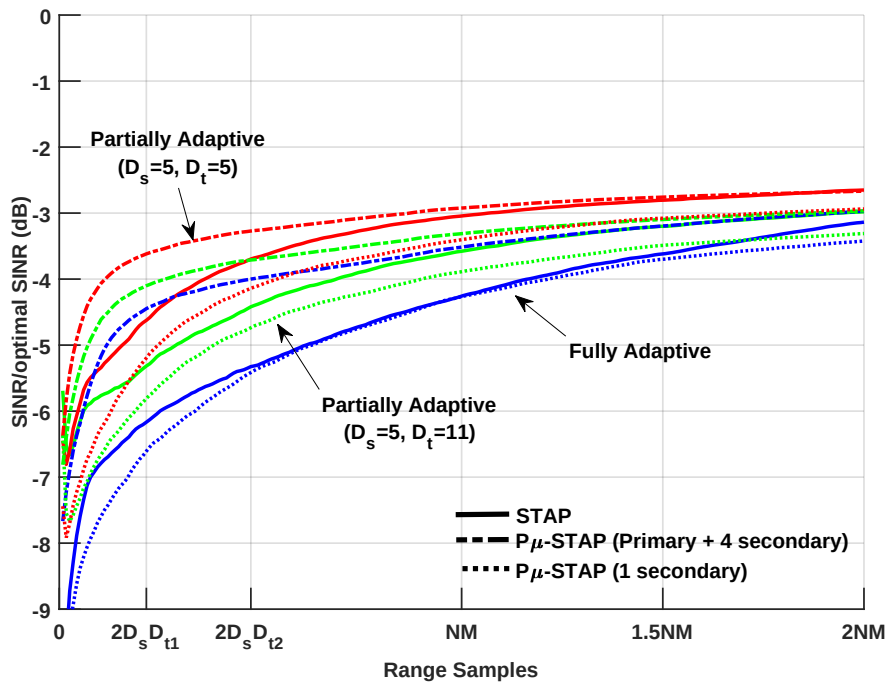

Figure 5.15: BSPrD Displace-Beam Average Improvement Factor in Heterogeneous Clutter

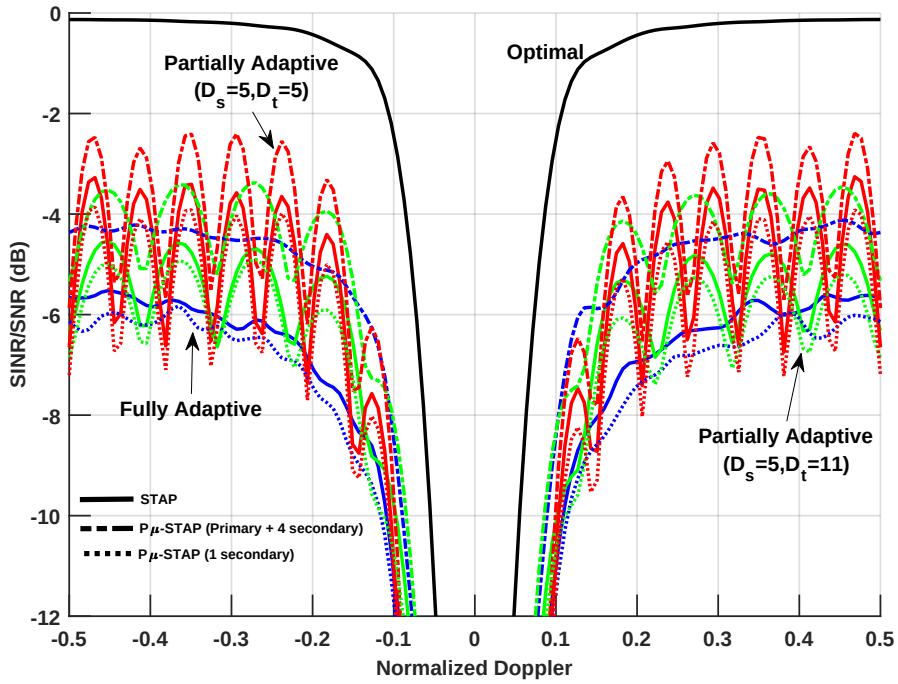

Figure 5.16: BSPrD Adjacent-Beam SINR Loss at $2D_sD_{t,1}$ in Heterogeneous Clutter

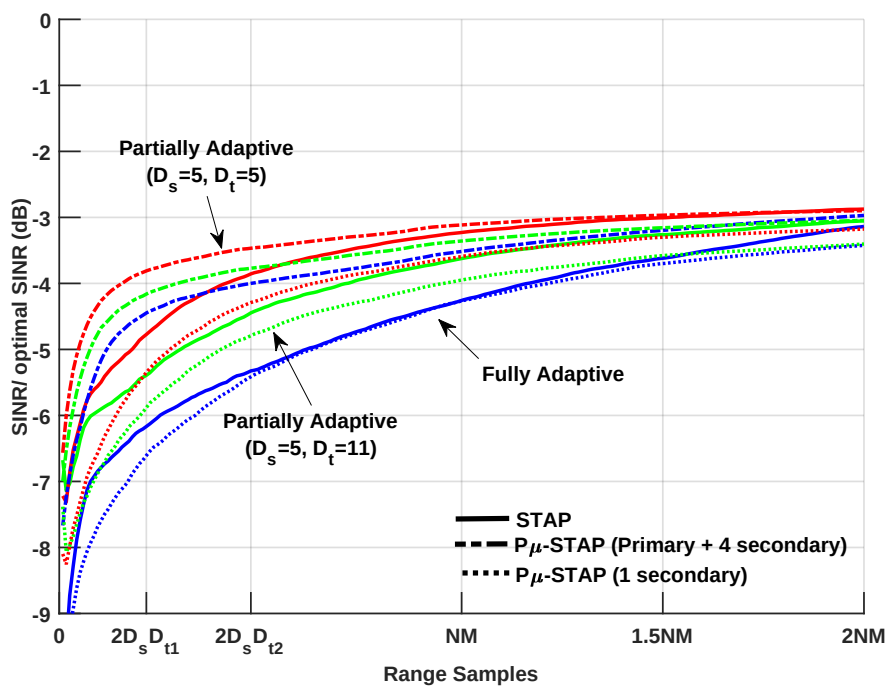

Figure 5.17: BSPrD Adjacent-Beam Average Improvement Factor in Heterogeneous Clutter

Adjacent-beam BSPrD SINR is presented in Figure 5.16. The mismatch is worst than displace-

beam. The results drop below fully adaptive in some Doppler frequencies. The benefit Pμ-STAP has over STAP is much less than being fully adaptive but still is better. Continuing onto the AIF in Fig. 5.17, at $2D_sD_{t,1}$ Pμ-STAP has a 1dB improvement over STAP. At the same point in full adaptation, Pμ-STAP has a 1.5dB benefit. The improvement compared to STAP decreases with reduction. Similar behavior at $2D_sD_{t,2}$.

5.2.2 Clutter Discrete in CUT

Next, BSPrD algorithms will be examined in heterogeneous data with a clutter discrete in the CUT. Figures 5.18-5.19, show the BSPrD displace-beam SINR and AIF, respectively. The clutter discrete has the degrades SINR loss for all the different responses. The robustness Pμ-STAP had in full adaptation is also seen here.

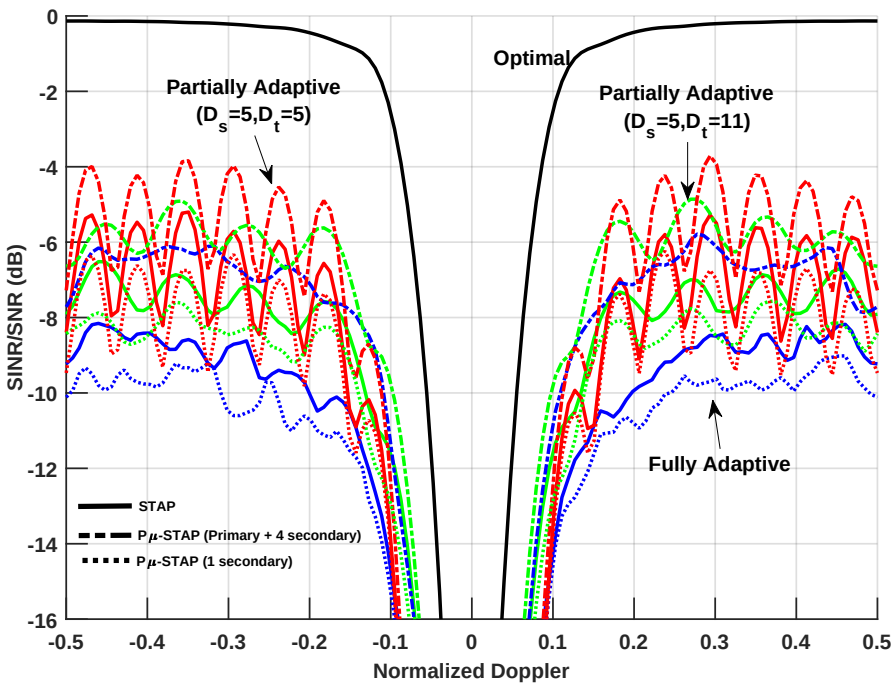

Figure 5.18: BSPrD Displace-Beam SINR Loss at $2D_sD_{t,1}$ with Clutter Discrete in CUT

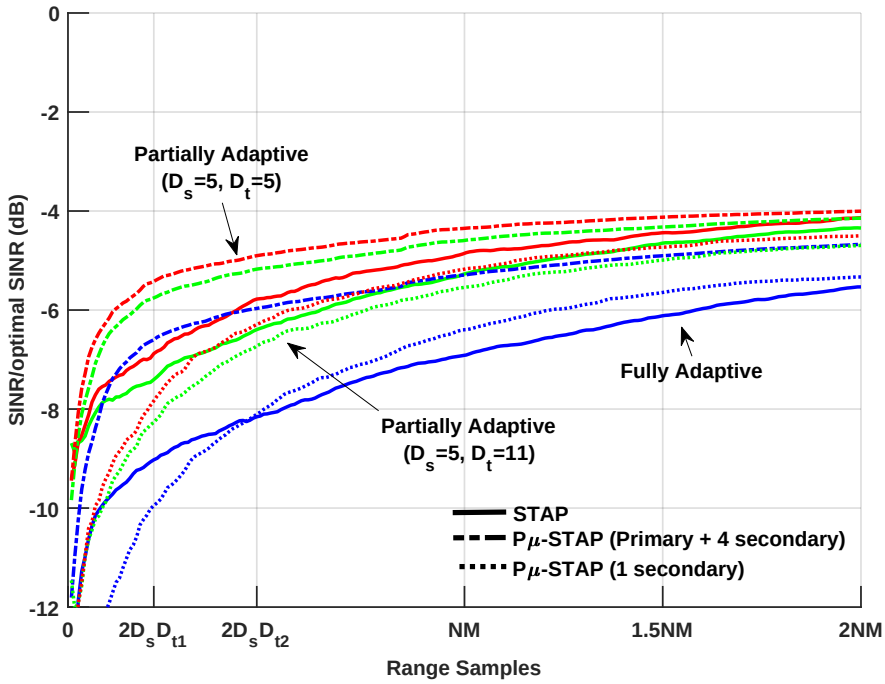

Figure 5.19: BSPrD Displace-Beam Average Improvement Factor with Clutter Discrete in CUT

In Figures 5.20-5.21, adjacent-beam SINR and AIF is presented. The SINR is similar to displace-beam. The MDD at $2D_sD_{t,1}$ decreases to the same frequency as fully adaptive STAP for partially adaptive STAP and partially adaptive Pμ-STAP. At $2D_sD_{t,1}$, MDD at for Pμ-STAP slightly improves above fully adaptive Pμ-STAP. The difference between the two the reductions is a fraction of a decibel throughout Pμ-STAP AIF. In contrast, the difference in AIF in STAP can be a much as 1dB at $2D_sD_{t,2}$.

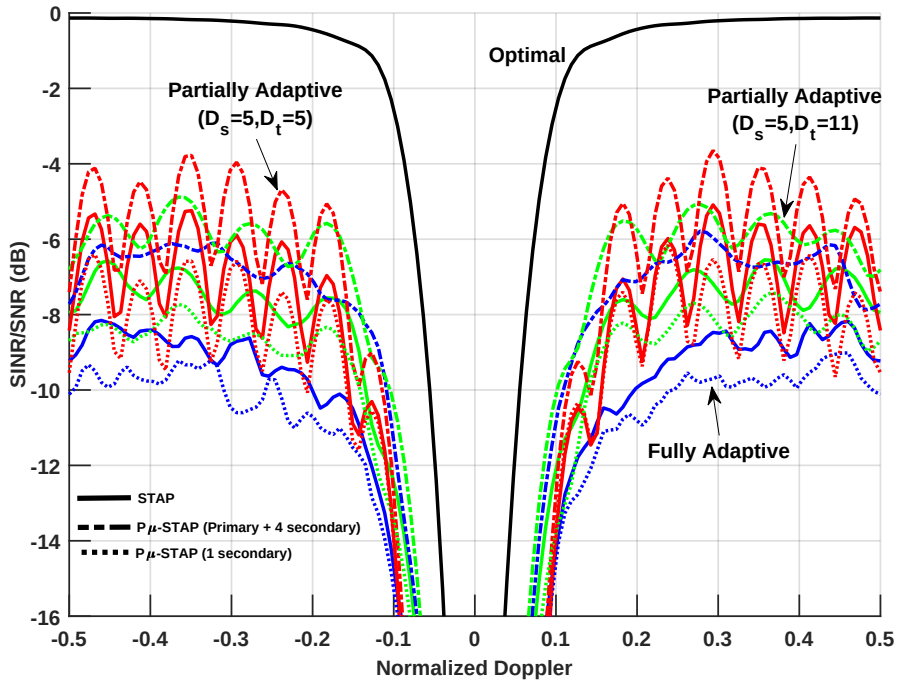

Figure 5.20: BSPrD Adjacent-Beam SINR Loss at $2D_sD_{t,1}$ with Clutter Discrete in CUT

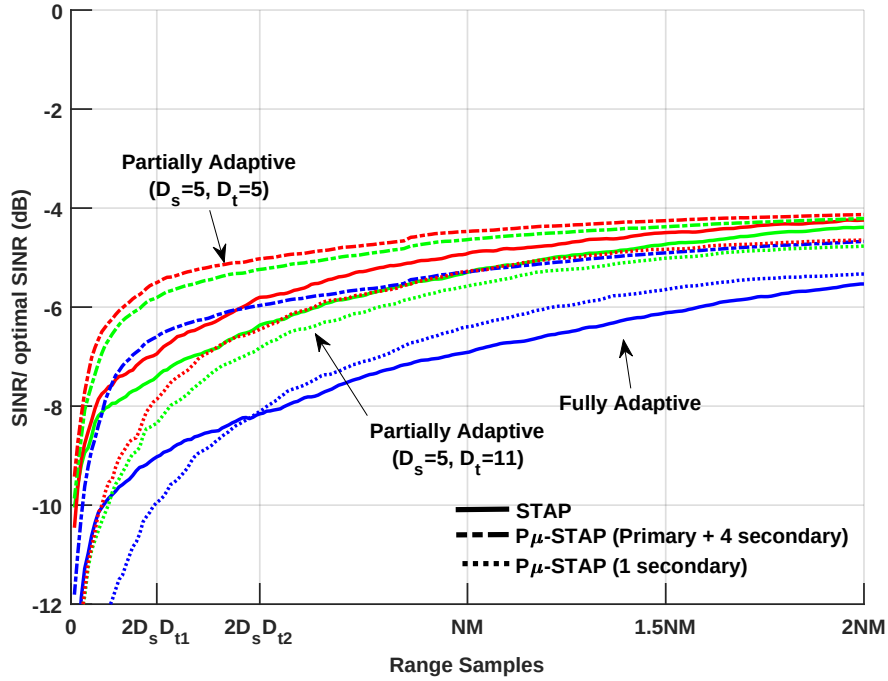

Figure 5.21: BSPrD Adjacent-Beam Average Improvement Factor with Clutter Discrete in CUT

5.2.3 Targets in Training Data

The final section in 5.2 will examine self-cancellation due to targets in the training data. In previous chapters, Pμ-STAP was very robust to this heterogeneity. This carries over into partial adaptation. Figures 5.22 and 5.23 show displace-beam and adjacent-beam BSPrD algorithms, respectively. The self-cancellation is occurring at $\omega = 0.49$. SIMO Pμ-STAP significantly boosts performance such that target cancellation notch is not seen in partially adaption. This is for both reduction amounts and algorithms .

To summarize, BSPrD algorithms consists of mismatch loss that is consistent on STAP and Pμ-STAP. The benefits Pμ-STAP translates to partially adaptive BSPrD. There is SINR loss and higher improvement factors in the presence of a clutter discrete in the CUT and great robustness to a self-cancellation.

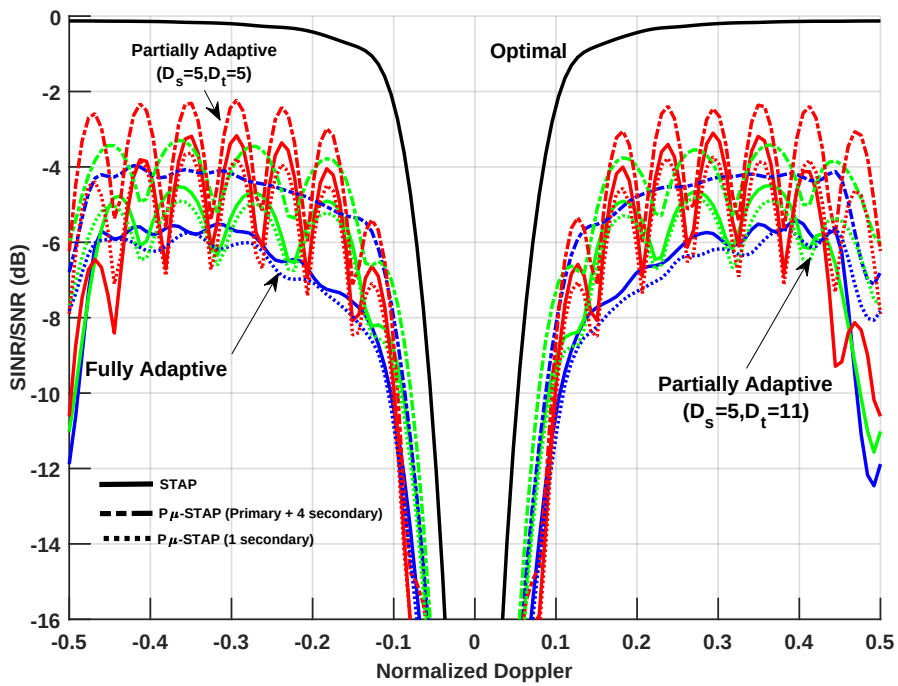

Figure 5.22: BSPrD Displace-Beam SINR Loss at $2D_sD_{t,1}$ with Targets in Training Data

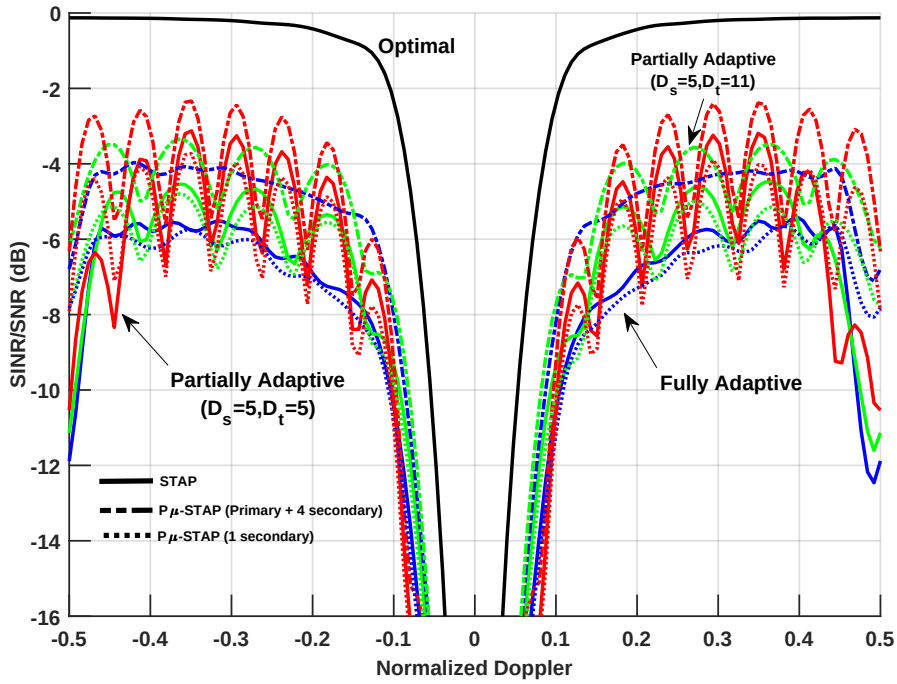

Figure 5.23: BSPrD Adjacent-Beam SINR Loss at $2ND_t$ with Targets in Training Data

5.3 Beam-Space Post-Doppler

Beam-space post-Doppler preprocesses spatial and temporal signals by utilizing the Doppler filter bank $\tilde{\mathbf{F}}_m$ and the beamformer matrix $\mathbf{G}_n$ presented in sections 5.1 and 5.2 [3]. PRI-staggered or adjacent-Bin can be combined with either displace-beam or adjacent-beam. Analogous algorithms from will be paired for reduction such that PRI-staggered (5.8) will be combined with displace-beam (5.19), and adjacent-Bin (5.11) will be combined with adjacent-beam (5.21). Using these algorithms, the transformation matrix for space-time partial adaptive is

$$\mathbf{T}_{mn} = \tilde{\mathbf{F}}_m \otimes \tilde{\mathbf{G}}_n \tag{5.25}$$

which is a $MN \times D_t D_s$ matrix. Applying this linear transformation to the space-time steering vector and μ-STAP SCMs using (5.1-5.2) forms space-time steering vector and SCM set associated with

the mth sub-CPI and nth antenna element as

$$\tilde{\mathbf{c}}_{st,m,n}(\theta,\omega) = \mathbf{T}_{mn}^{H}\mathbf{c}_{st}(\theta,\omega) \tag{5.26}$$

$$\begin{aligned}
\tilde{\mathbf{R}}_{\mu,m,n}(\ell) &= \mathbf{T}_{mn}^{H}\hat{\mathbf{R}}_{\mu}(\ell)\mathbf{T}_{mn} \\
\tilde{\mathbf{R}}_{\mu,m,n}(\ell) &= \mathbf{T}_{mn}^{H}\hat{\mathbf{R}}_{\text{prime}}(\ell)\mathbf{T}_{mn} + \mathbf{T}_{mn}^{H}\hat{\mathbf{R}}_{\mu,NP}(\ell)\mathbf{T}_{mn} \\
\tilde{\mathbf{R}}_{\mu,m,n}(\ell) &= \tilde{\mathbf{R}}_{\text{prime},m,n}(\ell) + \tilde{\mathbf{R}}_{\mu,NP,m,n}(\ell).
\end{aligned} \tag{5.27}$$

The analysis of BSPoD algorithms in heterogeneous clutter scenarios will be presented in the following subsections.

5.3.1 Heterogeneous Clutter

The reduction parameter for BSPoD are similar to BSPrD. SINR loss analysis will be performed at $n(L) = 2D_sD_{t,1}$, the algorithm is reduced to $N = 11$ to $D_s = 5$, and $M = 21$ to $D_{t,1} = 5$ and $D_{t,2} = 11$. Recall multi-dimension low sample support is $2D_sD_{t,1} = 50$. The analysis begins with PRI-staggered and displace-beam SINR and AIF in Figures 5.24 and 5.25 respectively. Incorporation of the Doppler filter bank has significantly diminished the mismatch loss. Pμ-STAP continues to translate in partially adaptive algorithms showing less SINR loss for detectable velocities and improved MDD. The AIF shows that the different reduction amounts are fairly similar for Pμ-STAP.

The analysis continues with adjacent-Bin and adjacent-beam SINR in Figure 5.26. The reduction algorithm provides excellent SINR for STAP. At one Doppler frequency ($\omega = -4.8$) for reduction $D_sD_{t,1}$ it is equal to Pμ-STAP. Nonetheless, Pμ-STAP SINR degrades less in the detectable velocities and higher MDD than STAP. The AIF in 5.27 shows the very small benefit Pμ-STAP has over STAP. STAP is within 1db or less at low sample support over the training sample intervals.

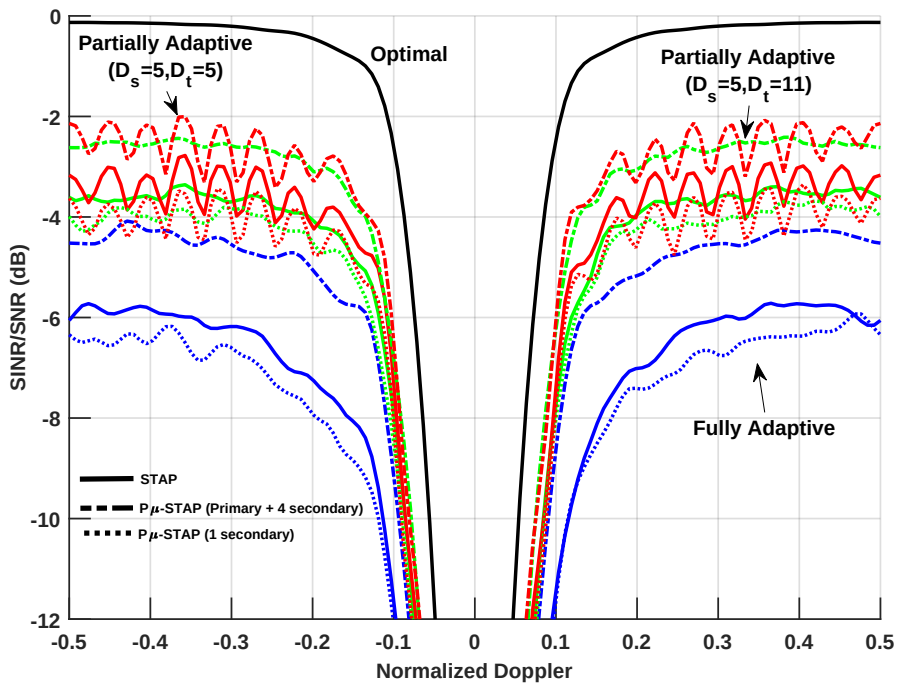

Figure 5.24: BSPoD PRI-Staggered/Displace-Beam SINR Loss at $2D_sD_{t,1}$ in Heterogeneous Clutter

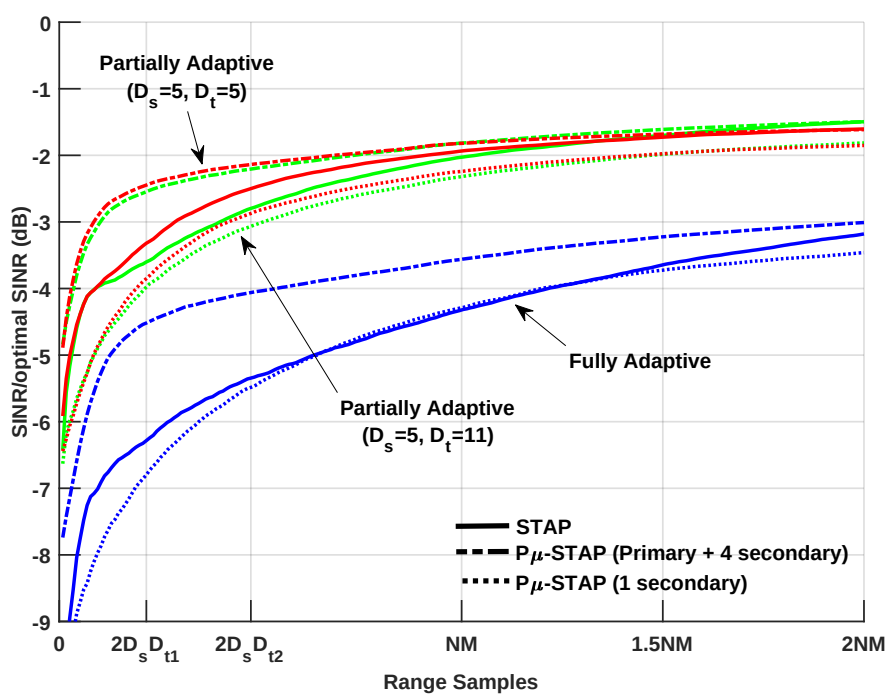

Figure 5.25: BSPoD PRI-Staggered/Displace-Beam Average Improvement Factor in Heterogeneous Clutter

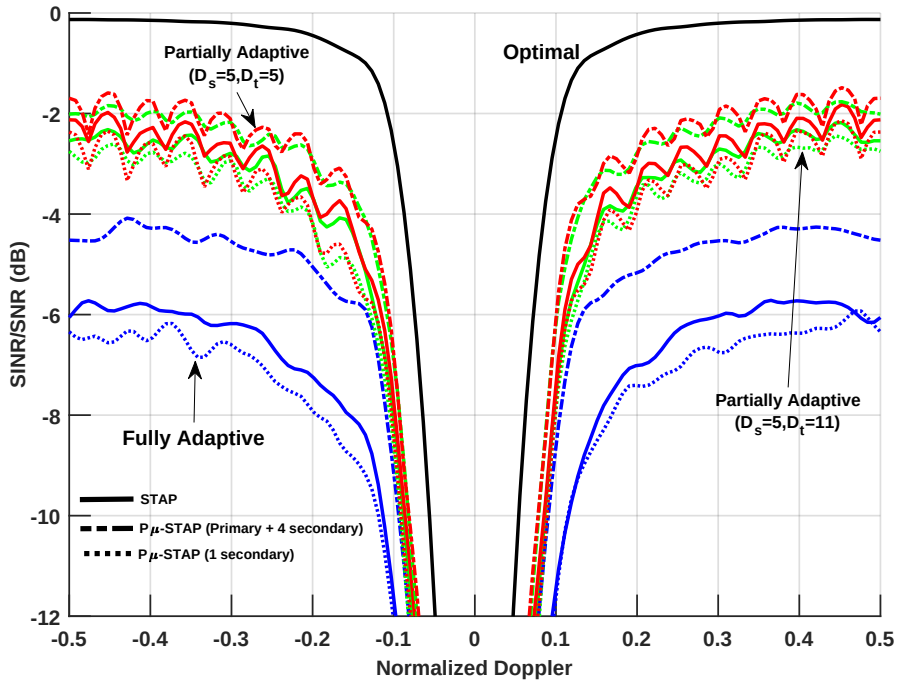

Figure 5.26: BSPoD Adjacent-Bin/Adjacent-Beam SINR Loss at $2D_sD_{t,1}$ in Heterogeneous Clutter

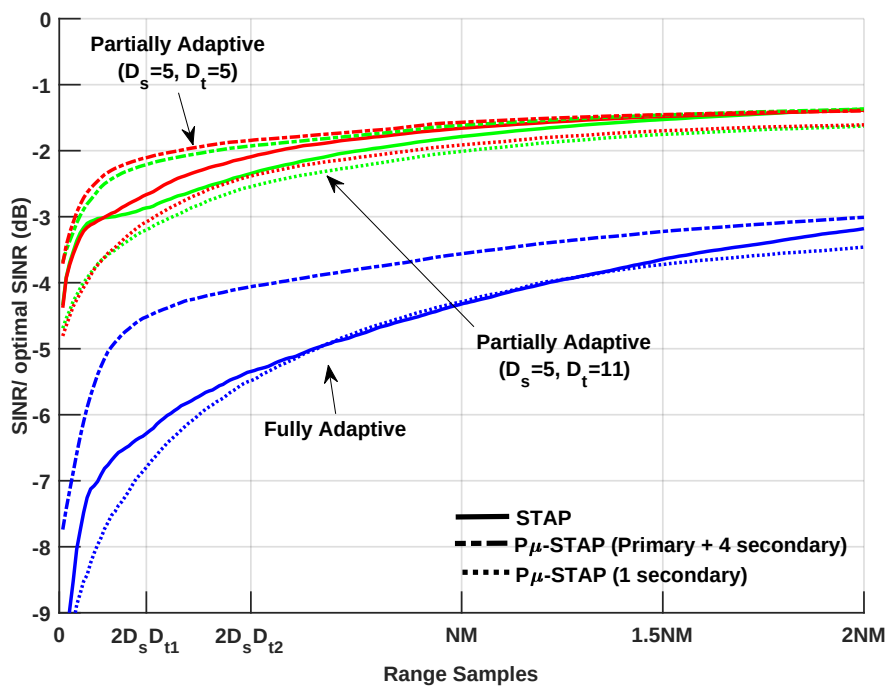

Figure 5.27: BSPoD Adjacent-Bin/Adjacent-Beam Average Improvement Factor in Heterogeneous Clutter

5.3.2 Clutter Discrete in CUT

In Figure 5.28 and 5.29, the PRI-staggered and displaced-beam BSPoD algorithms SINR and AIF are shown. The BSPoD is fairly robust to the heterogeneity. This is similarly seen in [3]. With the addition of Pμ-STAP, the robustness increases. The AIF reduction of $D_s D_{t,1}$ is less than $D_s D_{t,2}$ as the number of training samples increase. In full adaptive SISO Pμ-STAP, there is a benefit over STAP. This does not occur in partial adaptation as SISO Pμ-STAP less STAP.

Adjacent-beam and adjacent-bin results are shown in Figures 5.30 and 5.31. STAP performance is on par with Pμ-STAP in some Doppler frequencies. The MDD is still greater for Pμ-STAP, However the difference in performance between Pμ-STAP and STAP is marginal. this is further depicted in the AIF at $n(L) = 2D_s D_{t,1}$ and $n(L) = 2D_s D_{t,2}$. SISO Pμ-STAP AIF is again below STAP for this reduction algorithm.

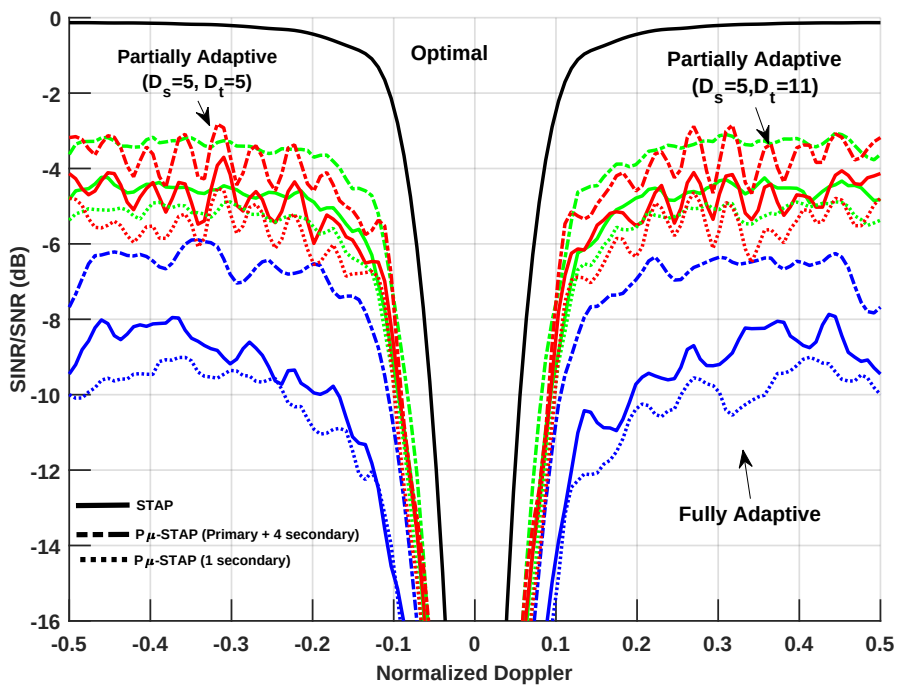

Figure 5.28: BSPoD PRI-Staggered/Displace-Beam SINR Loss at $2D_s D_{t,1}$ with Clutter Discrete in CUT

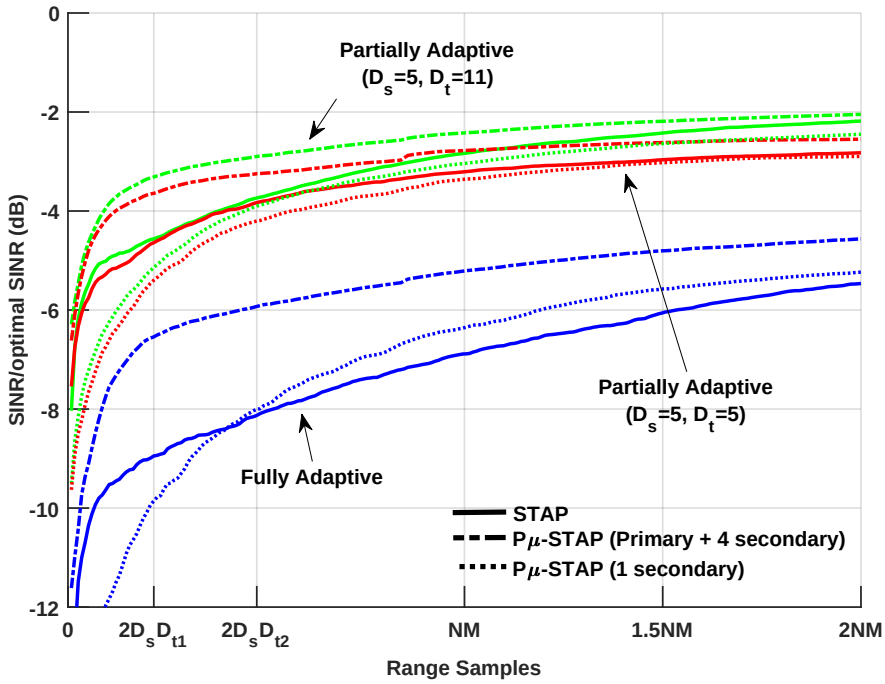

Figure 5.29: BSPoD PRI-Staggered/Displace-Beam Average Improvement Factor with Clutter Discrete in CUT

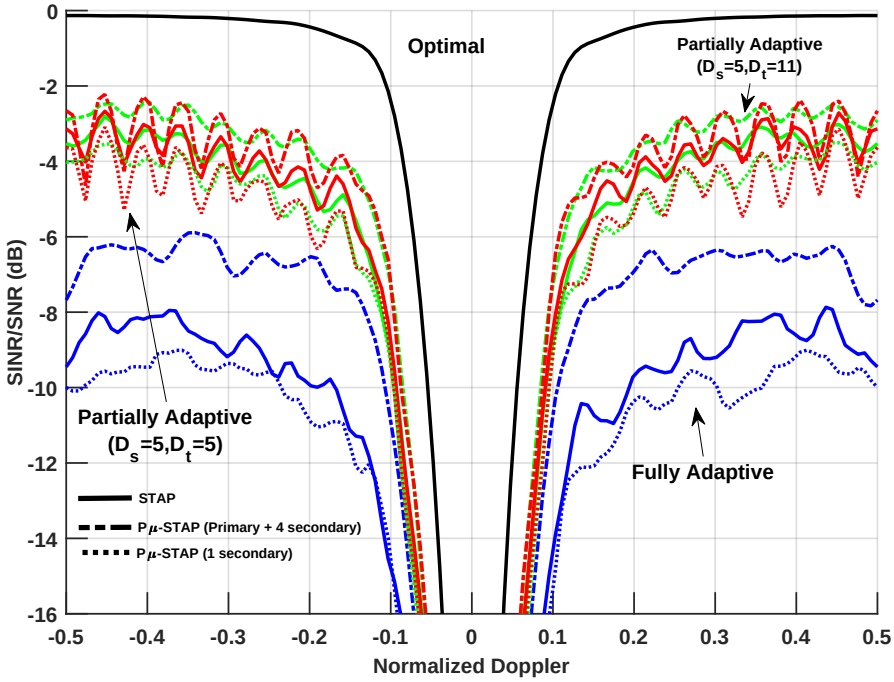

Figure 5.30: BSPoD Adjacent-Bin/Adjacent-Beam SINR Loss at $2D_sD_{t,1}$ with Clutter Discrete in CUT

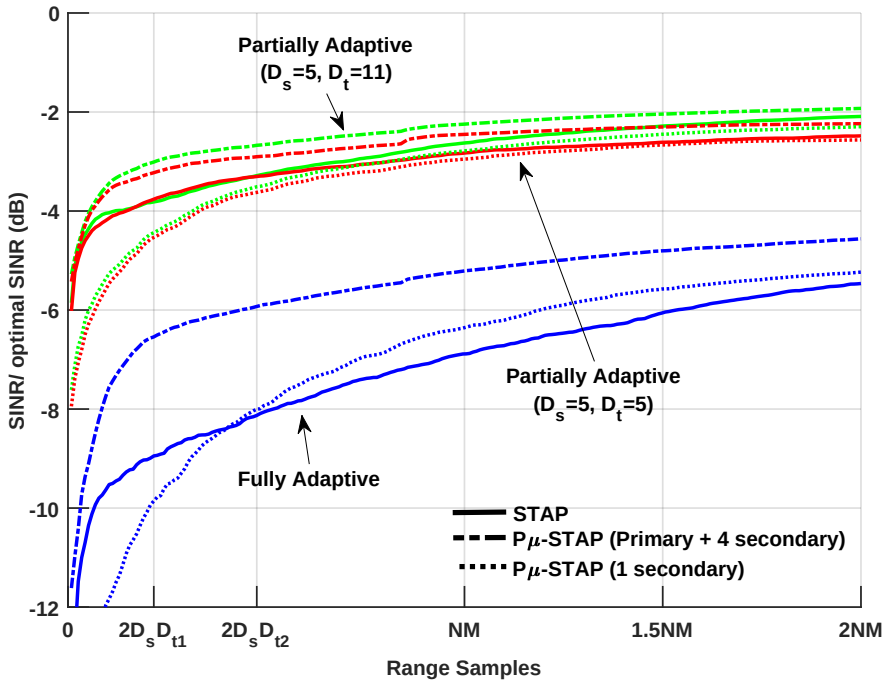

Figure 5.31: BSPoD Adjacent-Bin/Adjacent-Beam Average Improvement Factor with Clutter Discrete in CUT

5.3.3 Targets in Training Data

The final results are the most promising. BSPoD for PRI-staggered/displace-beam in heterogeneous clutter with targets in training data is depicted in Figure 5.32. The benefit of two-dimension space-time reduction provided a significant boost over a one-dimensional reduction as evident in analysis in this section. Utilizing BSPoD with Pμ-STAP provides enough robustness to greatly limit self-cancellation. At $\eta(\omega = .49) = -4dB$, for example, the self-cancellation null in partially adaptive Pμ-STAP is on par with partially adaptive STAP SINR frequencies self-cancellation does not occur. In contrast, targets in training data cause a -6dB loss on PA STAP performance. This is similarly seen in BSPoD adjacent-Bin/displaced-beam in (5.33). The amount of mismatch loss is less than PRI-staggered/displace-beam

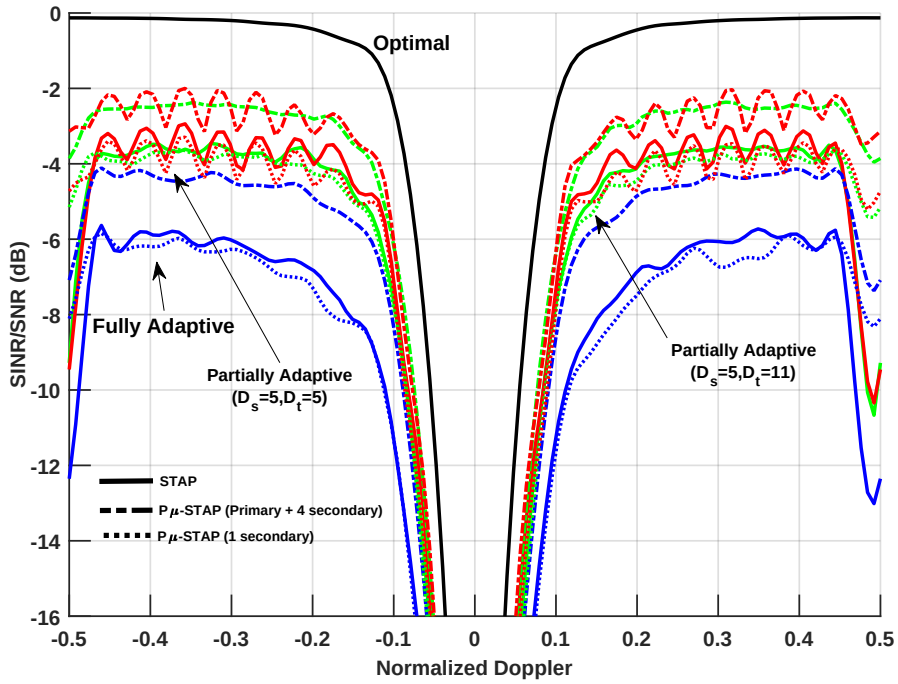

Figure 5.32: BSPoD PRI-Staggered/Displace-Beam SINR Loss at $2D_sD_{t,1}$ with Targets in Training Data

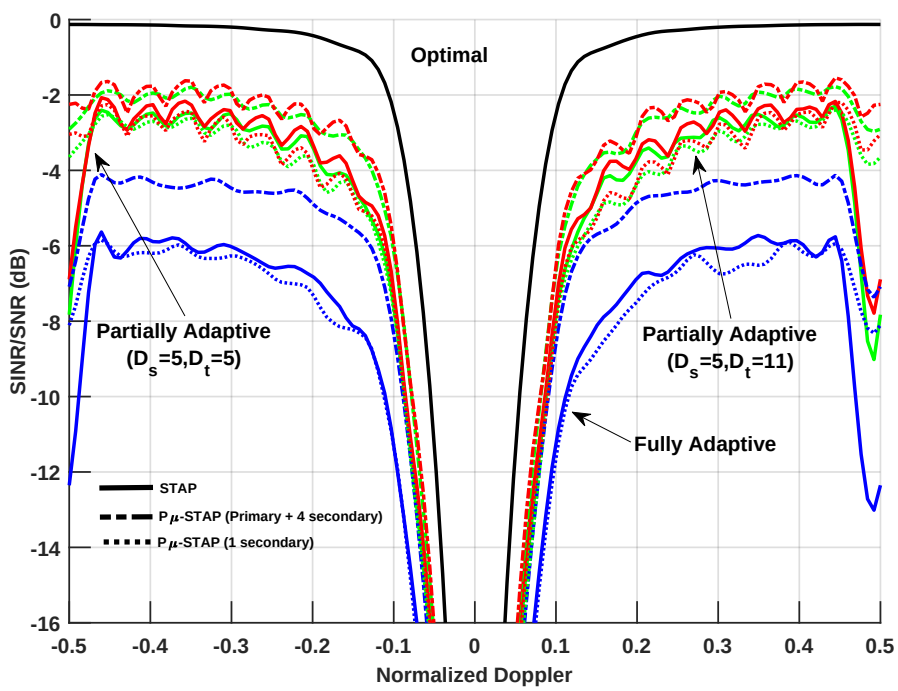

Figure 5.33: BSPoD Adjacent-Bin/Adjacent-Beam SINR Loss at $2D_sD_{t,1}$ with Targets in Training Data

In summary, space-time reduction is the provides greatest robustness to heterogeneous clutter. This reduces the amount of samples needed to satisfy the RMB rule and the size of the covariance matrix to make real-time processing practical. Pμ-STAP further increases robustness. Although in some cases, the benefit is marginal. The greatest benefit is seen in the presence of self-cancellation. Self-cancellation is reduced to have little to no affect on SINR loss.

Chapter 6

Conclusions

A new form of multi-waveform space-time adaptive processing (μ-STAP) called post pulse compression multi-waveform space-time adaptive processing (Pμ-STAP) was proposed for legacy systems performing ground moving target indication. The new formulation performs a homogenization of pulse compressed data using multiple homogenization filters to induce a smearing to the fast-time samples. This smeared data creates more identically distributed data, a critical assumption space-time adaptive processing uses. In addition, the multiple filters provide a multiplicative increase in training samples. Each of these provide a better space-time covariance estimate for clutter cancellation which maximizes SINR and detection performance. Prior knowledge of the transmit signal is not necessary for the proposed formulation A filter analysis of the homogenization filters was performed in simulated homogeneous and heterogeneous clutter. This analysis included filter length and number of secondary filters. Future work should examine SINR performance based on the relationship between the number of samples in the training data and length of the homogenization filter. Instead of based the filter length on time-bandwidth of the waveform, it may be more feasible to determine based on the number of training samples.

A comparison between STAP, μ-STAP, and Pμ-STAP was presented in a homogeneous and three heterogeneous clutter scenarios. The control simulated results showed that Pμ-STAP a provides a better SINR performance over STAP and μ-STAP. A similar comparison between STAP and Pμ-STAP was performed in the high-fidelity, heterogeneous clutter dataset KASSPER. Pμ-STAP was varied depending on the clutter environment. Due to this, it may only be applicable in a certain clutter environments. The results showed a trade off must be made between minor reduction in homogeneous clutter for large improvement in heterogeneous clutter. Future work will

require Pμ-STAP to be examined on experimental data to confirm this.

To mitigate computation cost, Pμ-STAP was examined with well-known partially adaptive techniques in the same four controlled,simulated clutter scenarios and compared to partially adaptive STAP. Reduction was performed in element-space post-Doppler, beam-space pre-Doppler and beam-space post-Doppler. Beam-space post-Doppler provided the best performance. Followed by element-space post-Doppler then beam-space pre-Doppler. Partially adaptive Pμ-STAP further enhances the performance of these algorithms. In each one, performance of Pμ-STAP is greater than partially adaptive STAP. In addition, the reduced dimension Pμ-STAP formulation can be generalized to all μ-STAP formulations due to their similar structure.

More future work should consider μ-STAP and Pμ-STAP covariance in censoring algorithms such as generalized inner product [28], adaptive power residue [29], adaptive coherence estimation [30; 31] and meta-algorithm FRACTA [32]. The work presented here will be presented in journal form in [33].

References

[1] M. A. Richards, J. A. Scheer, and W. A. Holm, Eds., *Principles of Modern Radar: Basic Principles*. Raleigh, NC: SciTech Publishing, Inc., 2010, vol. 1.

[2] W. L. Melvin and J. A. Scheer, Eds., *Principles of Modern Radar: Advanced Techniques*. Edison, NJ: SciTech Publishing, Inc., 2013, vol. 2.

[3] J. Ward, "Space-time adaptive processing for airborne radar," Lincoln Laboratory, Massachusetts Institute of Technology, Cambridge, MA, Tech. Rep. ESC-TR-94-109, 1994.

[4] M. Skolnik, Ed., *Radar Handbook*, 3rd ed. McGraw-Hill Companies, 2008.

[5] L. E. Brennan and L. S. Reed, "Theory of adaptive radar," *IEEE Transactions on Aerospace and Electronic Systems*, vol. AES-9, no. 2, pp. 237–252, March 1973.

[6] I. S. Reed, J. D. Mallett, and L. E. Brennan, "Rapid convergence rate in adaptive arrays," *IEEE Transactions on Aerospace and Electronic Systems*, vol. AES-10, no. 6, pp. 853–863, Nov 1974.

[7] W. L. Melvin, "Space-time adaptive radar performance in heterogeneous clutter," *IEEE Transactions on Aerospace and Electronic Systems*, vol. 36, no. 2, pp. 621–633, Apr 2000.

[8] S. D. Blunt, J. Jakabosky, J. Metcalf, J. Stiles, and B. Himed, "Multi-waveform stap," in *2013 IEEE Radar Conference (RadarCon13)*, April 2013, pp. 1–6.

[9] S. D. Blunt, J. Metcalf, J. Jakabosky, and B. Himed, "Sinr analysis of multi-waveform stap," in *2014 International Radar Conference*, Oct 2014, pp. 1–6.

[10] S. D. Blunt, J. Metcalf, J. Jakabosky, J. Stiles, and B. Himed, "Multi-waveform space-time adaptive processing," *IEEE Transactions on Aerospace and Electronic Systems*, vol. 53, no. 1, pp. 385–404, Feb 2017.

[11] N. Levanon and E. Mozeson, *Radar Signals*. Hoboken, NJ: John Wiley Sons, Inc., 2004.

[12] S. D. Blunt, M. Cook, J. Jakabosky, J. D. Graaf, and E. Perrins, "Polyphase-coded fm (pcfm) radar waveforms, part i: implementation," *IEEE Transactions on Aerospace and Electronic Systems*, vol. 50, no. 3, pp. 2218–2229, July 2014.

[13] S. D. Blunt, J. Jakabosky, M. Cook, J. Stiles, S. Seguin, and E. L. Mokole, "Polyphase-coded fm (pcfm) radar waveforms, part ii: optimization," *IEEE Transactions on Aerospace and Electronic Systems*, vol. 50, no. 3, pp. 2230–2241, July 2014.

[14] R. Klemm, *Principles of Space-time Adaptive Processing*. London, England, UK: The institution of Electrical Engineers, 2002.

[15] F. T. Ulaby and D. G. Long, *Microwave Radar and Radiometric Remote Sensing*. Norwood: Artech House, 2015.

[16] L. Brennan, J. Mallett, and I. Reed, "Adaptive arrays in airborne mti radar," *IEEE Transactions on Antennas and Propagation*, vol. 24, no. 5, pp. 607–615, Sep 1976.

[17] S. S. Haykin, *Adaptive radar detection and estimation*. New York, NY: Wiley, 1992.

[18] J. S. Bergin, C. M. Teixeira, and P. M. Techau, "Multi-resolution signal processing techniques for airborne radar," in *Proceedings of the 2004 IEEE Radar Conference (IEEE Cat. No.04CH37509)*, April 2004, pp. 277–282.

[19] G. A. Akers and J. M. Stiles, "An approach to ground moving target indication (gmti) using multiple resolutions of the clutter covariance matrix," in *2009 IEEE Radar Conference*, May 2009, pp. 1–5.

[20] J. G. Metcalf, K. J. Sangston, M. Rangaswamy, S. D. Blunt, and B. Himed, "A new method of generating multivariate weibull distributed data," in *2016 IEEE Radar Conference (RadarConf)*, May 2016, pp. 1–6.

[21] J. B. Billingsley, A. Farina, F. Gini, M. V. Greco, and L. Verrazzani, "Statistical analyses of measured radar ground clutter data," *IEEE Transactions on Aerospace and Electronic Systems*, vol. 35, no. 2, pp. 579–593, Apr 1999.

[22] K. Gerlach, "The effects of signal contamination on two adaptive detectors," *IEEE Transactions on Aerospace and Electronic Systems*, vol. 31, no. 1, pp. 297–309, Jan 1995.

[23] J. S. Bergin and P. M. Techau, "High-fidelity site-specific radar simulation: Kassper '02," ISL, Vienna, VA, Tech. Rep. ISL-SCRD-TR-02-10, May 2002.

[24] J. R. Guerci and E. J. Baranoski, "Knowledge-aided adaptive radar at darpa: an overview," *IEEE Signal Processing Magazine*, vol. 23, no. 1, pp. 41–50, Jan 2006.

[25] J. R. Guerci, *Space-time adaptive processing for radar*, 2nd ed. Artech House, 2015.

[26] L. Harnett, P. M. McCormick, S. D. Blunt, and J. G. Metcalf, "Multi-window post-doppler dimensionality reduction for multi-waveform stap," in *2016 IEEE Radar Conference (RadarConf)*, May 2016, pp. 1–6.

[27] R. C. DiPietro, "Extended factored space-time processing for airborne radar systems," in *[1992] Conference Record of the Twenty-Sixth Asilomar Conference on Signals, Systems Computers*, Oct 1992, pp. 425–430 vol.1.

[28] P. Chen, W. L. Melvin, and M. C. Wicks, "Screening among multivariate normal data," *Journal of Multivariate Analysis*, vol. 69, no. 1, pp. 10 – 29, 1999. [Online]. Available: http://www.sciencedirect.com/science/article/pii/S0047259X98917882

[29] K. Gerlach, "Outlier resistant adaptive matched filtering," *IEEE Transactions on Aerospace and Electronic Systems*, vol. 38, no. 3, pp. 885–901, Jul 2002.

[30] L. L. Scharf and L. T. McWhorter, "Adaptive matched subspace detectors and adaptive coherence estimators," in *Conference Record of The Thirtieth Asilomar Conference on Signals, Systems and Computers*, Nov 1996, pp. 1114–1117 vol.2.

[31] N. B. Pulsone and M. A. Zatman, "A computationally efficient two-step implementation of the glrt," *IEEE Transactions on Signal Processing*, vol. 48, no. 3, pp. 609–616, Mar 2000.

[32] K. Gerlach, S. D. Blunt, and M. L. Picciolo, "Robust adaptive matched filtering using the fracta algorithm," *IEEE Transactions on Aerospace and Electronic Systems*, vol. 40, no. 3, pp. 929–945, July 2004.

[33] L. Harnett, S. D. Blunt, and J. G. Metcalf, "Post and partially adaptive multi-waveform space-time adaptive processing," *in preparation for IEEE Aerospace and Electronic Systems Magazine*.

[34] R. Klemm, "Adaptive clutter suppression for airborne phased array radars," *Microwaves, Optics and Antennas, IEE Proceedings H*, vol. 130, no. 1, pp. 125–132, February 1983.

[35] J. Ender and R. Klemm, "Airborne mti via digital filtering," *IEE Proceedings F - Radar and Signal Processing*, vol. 136, no. 1, pp. 22–28, Feb 1989.

[36] R. Klemm, "Adaptive airborne mti with two-dimensional motion compensation," *IEE Proceedings F - Radar and Signal Processing*, vol. 138, no. 6, pp. 551–558, Dec 1991.

[37] J. R. Guerci, "Theory and application of covariance matrix tapers for robust adaptive beamforming," *IEEE Transactions on Signal Processing*, vol. 47, no. 4, pp. 977–985, Apr 1999.

[38] D. J. Rabideau and A. O. Steinhardt, "Improved adaptive clutter cancellation through data-adaptive training," *IEEE Transactions on Aerospace and Electronic Systems*, vol. 35, no. 3, pp. 879–891, Jul 1999.

[39] S. M. Kogon and M. A. Zatman, "Stap adaptive weight training using phase and power selection criteria," in *Conference Record of Thirty-Fifth Asilomar Conference on Signals, Systems and Computers (Cat.No.01CH37256)*, vol. 1, Nov 2001, pp. 98–102 vol.1.

[40] G. Benitz, J. D. Griesbach, and C. Rader, "Two-parameter power-variable-training stap," in *Conference Record of the Thirty-Eighth Asilomar Conference on Signals, Systems and Computers, 2004.*, vol. 2, Nov 2004, pp. 2359–2363 Vol.2.

[41] T. M. Selee, K. F. Bing, and W. L. Melvin, "Stap application in mountainous terrain: Challenges and strategies," in *2012 IEEE Radar Conference*, May 2012, pp. 0824–0829.

[42] J. R. Roman, M. Rangaswamy, D. W. Davis, Q. Zhang, B. Himed, and J. H. Michels, "Parametric adaptive matched filter for airborne radar applications," *IEEE Transactions on Aerospace and Electronic Systems*, vol. 36, no. 2, pp. 677–692, Apr 2000.

[43] R. S. Adve, T. B. Hale, and M. C. Wicks, "Practical joint domain localised adaptive processing in homogeneous and nonhomogeneous environments. 2. nonhomogeneous environments," *IEE Proceedings - Radar, Sonar and Navigation*, vol. 147, no. 2, pp. 66–74, Apr 2000.

[44] T. K. Sarkar, H. Wang, S. Park, R. Adve, J. Koh, K. Kim, Y. Zhang, M. C. Wicks, and R. D. Brown, "A deterministic least-squares approach to space-time adaptive processing (stap)," *IEEE Transactions on Antennas and Propagation*, vol. 49, no. 1, pp. 91–103, Jan 2001.

[45] G. A. Fabrizio and M. D. Turley, "An advanced stap implementation for surveillance radar systems," in *Proceedings of the 11th IEEE Signal Processing Workshop on Statistical Signal Processing (Cat. No.01TH8563)*, 2001, pp. 134–137.

[46] K. Gerlach, "Outlier resistant adaptive matched filtering," *IEEE Transactions on Aerospace and Electronic Systems*, vol. 38, no. 3, pp. 885–901, Jul 2002.

[47] Y.-L. Wang, J.-W. Chen, Z. Bao, and Y.-N. Peng, "Robust space-time adaptive processing for airborne radar in nonhomogeneous clutter environments," *IEEE Transactions on Aerospace and Electronic Systems*, vol. 39, no. 1, pp. 70–81, Jan 2003.

[48] M. L. Picciolo and K. Gerlach, "Median cascaded canceller for robust adaptive array processing," *IEEE Transactions on Aerospace and Electronic Systems*, vol. 39, no. 3, pp. 883–900, July 2003.

[49] K. Gerlach, S. D. Blunt, and M. L. Picciolo, "Robust adaptive matched filtering using the fracta algorithm," *IEEE Transactions on Aerospace and Electronic Systems*, vol. 40, no. 3, pp. 929–945, July 2004.

[50] S. D. Blunt and K. Gerlach, "Efficient robust amf using the fracta algorithm," *IEEE Transactions on Aerospace and Electronic Systems*, vol. 41, no. 2, pp. 537–548, April 2005.

[51] W. L. Melvin and J. R. Guerci, "Knowledge-aided signal processing: a new paradigm for radar and other advanced sensors," *IEEE Transactions on Aerospace and Electronic Systems*, vol. 42, no. 3, pp. 983–996, July 2006.

[52] W. L. Melvin and G. A. Showman, "An approach to knowledge-aided covariance estimation," *IEEE Transactions on Aerospace and Electronic Systems*, vol. 42, no. 3, pp. 1021–1042, July 2006.

[53] S. D. Blunt, K. Gerlach, and M. Rangaswamy, "Stap using knowledge-aided covariance estimation and the fracta algorithm," *IEEE Transactions on Aerospace and Electronic Systems*, vol. 42, no. 3, pp. 1043–1057, July 2006.

[54] F. Gini and M. Rangaswamy, *Knowledge Based Radar Detection, Tracking, and Classification,*. Hoboken, NJ: Wiley, 2008.

[55] E. Aboutanios and B. Mulgrew, "Hybrid detection approach for stap in heterogeneous clut-

ter," *IEEE Transactions on Aerospace and Electronic Systems*, vol. 46, no. 3, pp. 1021–1033, July 2010.

[56] O. Besson and S. Bidon, "Adaptive processing with signal contaminated training samples," *IEEE Transactions on Signal Processing*, vol. 61, no. 17, pp. 4318–4329, Sept, 2013.

[57] S. D. Blunt and E. L. Mokole, "Overview of radar waveform diversity," *IEEE Aerospace and Electronic Systems Magazine*, vol. 31, no. 11, pp. 2–42, November 2016.

[58] F. Gini, A. de Maio, and L. Patton, *Waveform Design and Diversity for Advanced Radar Systems*. Institution of Engineering and Technology, 2012.

[59] M. C. Wicks, E. L. Mokole, S. D. Blunt, R. S. Schneible, and V. J. Amuso, *Principles of waveform diversity and design*. SciTech Publishing, 2010.

[60] J. Jakabosky, S. D. Blunt, M. R. Cook, J. Stiles, and S. A. Seguin, "Transmitter-in-the-loop optimization of physical radar emissions," in *2012 IEEE Radar Conference*, May 2012, pp. 0874–0879.

[61] J. Jakabosky, P. Anglin, M. R. Cook, S. D. Blunt, and J. Stiles, "Non-linear fm waveform design using marginal fisher's information within the cpm framework," in *2011 IEEE RadarCon (RADAR)*, May 2011, pp. 513–518.

[62] S. Blunt, M. Cook, E. Perrins, and J. de Graaf, "Cpm-based radar waveforms for efficiently bandlimiting a transmitted spectrum," in *2009 IEEE Radar Conference*, May 2009, pp. 1–6.